ON THE ONSET OF MULTIFRAGMENTATION AND VAPORIZATION IN NUCLEAR REACTIONS

A THESIS

submitted to the
FACULTY OF SCIENCE
PANJAB UNIVERSITY, CHANDIGARH
for the degree of

DOCTOR OF PHILOSOPHY

2019

SAMIKSHA SOOD

CENTRE OF ADVANCED STUDY IN PHYSICS
DEPARTMENT OF PHYSICS
PANJAB UNIVERSITY
CHANDIGARH
INDIA

DEPARTMENT OF PHYSICS
Centre of Advanced Study in Physics
PANJAB UNIVERSITY, CHANDIGARH-160 014 (INDIA)
Fax: ++91-172-2783336
Phone: ++91-172-2541741
EPABX: ++91-172-2534466, 2534446
Email: casphypu.ac.in

CORRECTION CERTIFICATE

It is certified that there were no specific corrections recommended by the examiner of **Ms. Samiksha Sood** in her Ph.D. **"ON THE ONSET OF MULTIFRAGMENTATION AND VAPORIZATION IN NUCLEAR REACTIONS "**. The thesis submitted by **Ms. Samiksha Sood** in the present form, is acceptable.

(Prof. Navdeep Goyal)
Dept. of Physics,
P.U., Chandigarh
(Chairman)

(Prof. Rajeev K. Puri)
Department of Physics
P.U., Chandigarh
(Supervisor)

(Dr. Sakshi Gautam)
Department of Physics
P.U., Chandigarh
Supervisor)

Chairperson
Department of Physics
Panjab University
Chandigarh-160014

Acknowledgements

The final completion of thesis is the job of whole unit of loving, caring and strong people around us who help us achieve the goal. I am extremely blessed to have such beautiful people around me that motivated and encouraged me to reach this day. I should be failing in my duty if I do not show my heartfelt gratitude to them for their help. First and foremost, I thank god for his countless blessings and giving me strength to complete my work.

I owe my deepest gratitude to my esteemed supervisor ***Prof. Rajeev K. Puri*** *for his expert guidance and motivation throughout my thesis. I have known him as a good human being and an inspiring mentor. His passion for good work and aim to achieve perfection has made a deep impression on me. Not only he is readily available for his students but also responds more promptly than one can imagine. His dynamism, eagle-eyed vision and his positive attitude towards work inspired me to realize my own potentials. His constructive words not only helped me perform better in my work but has also helped me to become better individual in life. His patience and support helped me overcome many difficult situations and complete this dissertation. I feel blessed to be associated with a person like him during my life.*

I would like to extend my sincere gratitude to my supervisor, ***Dr. Sakshi Gautam****. During our course of interaction, I have gained extensively from her. From her ideologies, I have learned how to approach a problem by systematic thinking and how to regard an old question from a new perspective. She has been always personally present to render any sought of help and guidance. I owe her lots of gratitude for always being there for me as a great mentor to support and encourage me.*

My sincerest thanks to my senior ***Dr. Rohit Kumar*** *for his unrelenting support in my thesis. I am extremely grateful to him for the long discussions that helped me sort out the technical details of my work. His constructive criticisms and insightful ideas at different stages of my research were provocative and they helped me to perform better in my work. I owe a lot of gratitude to him for always being there. Words will never be enough to say my heartfelt thank you to him.*

I gratefully acknowledge, ***Dr. Arun Sharma*** *for his guidance, valuable advice and extensive discussions about my work. He has been the source of endless encouragement*

throughout my work.

I offer my special thanks to ***Prof. Jörg Aichelin*** *and* ***Dr. Christoph Hartnack*** *at SUBATECH, Nantes in France, for fruitful discussions.*

Next, I would like to thank the Chairpersons, Department of Physics, Panjab University, Chandigarh for providing all the necessary facilities in the department. Also, the author expresses his thankfulness to the staff of the Physics Department for their kind support. My sincerest thanks to Dr. Vipin Bhatnagar for providing necessary computational facility for my research work by extending assistance in HPCC facility.

My special regards to all my teachers in the department who helped me complete such great years of life in the department. They assisted and guided me in every phase of my life. My heartfelt thanks to my fellow scholars Dr. Preeti Bansal, Sakshi, Sucheta, Navjot and Rajat for their cheerful company as my colleagues and friends. I also learned a lot from my senior scholars, through their guidance and interactions, their suggestions at various points of my research programme. My special appreciation goes to my wonderful friends Suman, Gurpreet, Anjali, Priyanka for the beautiful friendship we share together. I can bank upon them without any obligation and hesitation.

My special thanks to my bua and uncle for their endless love and support. The cheerful company of my cousins Ridhi and Anuja always worked as a stress free therapy for me. My heartfelt gratitude to my late cousin Arjun for loving me so much and making me smile, you will always be missed.

I am also grateful to Monika mam for always being there to help, guide and motivate me. She has been a true support throughout my journey. I feel blessed to have Ishita and Arpita for the beautiful bond and love we share together.

I also owe my deepest gratitude towards my best friend and my would be better half Mr. Harit Angrish for his love and support throughout the journey. He was always there for me during tough times of my Ph. D. I also extend my thanks to my new family for encouraging me to achieve my goal.

I would like to pay high regards to my parents for their selfless love and care. I owe everything to them. Besides this, several people have knowingly and unknowingly helped me in the successful completion of this project. I really appreciate there help.

Dated: (Samiksha Sood)

Chandigarh

List of Publications

A. International Journals:

1. Multifragmentation in the perspectives of various clusterization algorithms.
   Rohit Kumar, Arun Sharma, **Samiksha Sood** and Rajeev K. Puri,
   Nuclear Particle Correlations and Cluster Physics (Book) (World Scientific Publishing) (2016) (*12 pages*).

2. Study of bound structures Formed in heavy-ion collisions using metropolis computational technique.
   Samiksha Sood, Ishita Puri, Rohit Kumar and Rajeev K. Puri,
   International Journal of Engineering Technology, Management and Applied Sciences **5**, 2 (2017) (7 pages).

3. Use of Simulated Annealing Technique for finding most bound structures in nuclear reactions.
   Samiksha Sood, Ishita Puri, Rohit Kumar, Arun Sharma and Rajeev K. Puri,
   International Journal of Pure and Applied Physics **13**, 201 (2017) (*4 pages*).

4. On the relative role of temperature of fragments within the framework of quantum molecular dynamics model.
   Rohit Kumar, Arun Sharma, **Samiksha Sood** and Rajeev K. Puri,
   International Journal of Pure and Applied Physics **13**, 17 (2017) (*4 pages*).

5. Study of intermediate energy heavy-ion collisions in asymmetric colliding nuclei using computational methods.
   Arun Sharma, Rohit Kumar, **Samiksha Sood** and Rajeev K. Puri,
   International Journal of Pure and Applied Physics **13**, 21 (2017) (*4 pages*).

6. On the multifragmentation and phase transition in the perspectives of different N-body dynamical models.
   Rohit Kumar, **Samiksha Sood**, Arun Sharma and Rajeev K. Puri,
   Acta Physica Polonica B **49**, 3 (2018) (*6 pages*).

7. Cluster formation and phase transition in nuclear disassembly using a variety of clusterization algorithms.
   Samiksha Sood, Rohit Kumar, Arun Sharma and Rajeev K. Puri,
   Physical Review C **99**, 054612 (2019) (*7 pages*).

8. Fragment emission and critical behavior in light and heavy charged systems.
   Samiksha Sood, Rohit Kumar, Arun Sharma and Rajeev K. Puri,
   Journal of Physics G (2019), (*Submitted*).

9. Role of mass asymmetry in the production of light particles and entropy at incident energies $\geq$ 400 MeV/nucleon.
   Samiksha Sood, Rohit Kumar, and Rajeev K. Puri, Physical Review C (2019)(*Submitted*).

10. On the onset of vaporization and its systematic study within n-body dynamical models.
    Samiksha Sood, Rohit Kumar, and Rajeev K. Puri, Physical Review C (2019)(*Submitted*).

B. Conference Proceedings/Abstracts accepted:

1. Entropy production and its dependance on the asymmetry of a reaction.
   Samiksha Sood, Rohit Kumar, and Rajeev K. Puri,
   Proceedings of the DAE Symposium on Nuclear Physics **63**, 548 (2018) (*2 pages*).

2. Systematic study of entropy production in asymmetric reactions using transport model.
   Samiksha Sood, Rohit Kumar, and Rajeev K. Puri,
   Zakopane Conference on Nuclear Physics 2018 (*abstract accepted*).

3. On the fragment production and phase transition using QMD + SACA model.
   Samiksha Sood, Rohit Kumar, and Rajeev K. Puri,
   INDO-FRENCH Seminar on"Multifragmentation, Collective Flow and Sub Threshold Particle Production in Heavy Ion Reactions".
   Department of Physics, Panjab University, Chandigarh, India (2019) (*accepted*).

4. Role of spatial correlations on the onset of nuclear vaporization in ^{16}O+^{80}Br reaction.
   Samiksha Sood, Rohit Kumar, Arun Sharma and Rajeev K. Puri,
   Proceedings of the Jangjeon Mathematical Society **22**, 1 (2019) (*9 pages*).

Other Publications [1]:

1. Effect of initialization on the fragment production.
   Sukhjit Kaur and **Samiksha Sood**,
   Proceedings of the DAE Symposium on Nuclear Physics **59**, 484 (2014) (*2 pages*).

2. Structural effects on the peak production of fragments.
   Sukhjit Kaur and **Samiksha Sood**,
   Acta Physica Polonica B **46**, 3 (2015) (*4 pages*).

[1]Work not included in the thesis

Contents

List of Figures

List of Tables

PREFACE

The description of nuclear matter away from the ground state (specifically at high densities and temperatures) remains a challenging area of research for physicists for a long time now. The main interest in this research area is fuelled due to the use of the nuclear matter properties to investigate various astrophysical phenomena such as evolution of the proto-neutron stars, explosion mechanism of supernova as well as evolution of the universe at initial times. The only accessible tool to create nuclear matter at such conditions on earth is heavy-ion collisions. Though, a large number of experimental as well as theoretical studies have been conducted to understand behavior of nuclear matter at these extreme conditions of temperature and pressure, its comprehensive picture is still missing. The present study is done in the framework of dynamical models i.e., Quantum Molecular Dynamical (QMD) model and Isospin dependent Quantum Molecular Dynamics (IQMD) model. The phase space generated via Quantum Molecular Dynamics (QMD) model is further subjected to various available clusterization algorithms i.e., Minimum Spanning Tree (MST) method, Minimum Spanning Tree method with Momentum (MSTM or MSTP) cut, Minimum Spanning Tree method with Binding (MSTB) energy cut, Minimum Spanning Tree method with Temperature-dependent Binding (MSTBT) energy cut and Simulated Annealing Clusterization Algorithm (SACA). Multifragmentation is considered as the strong candidate to study phase transitions in nuclear matter. Various phases of nuclear matter constitute different sized multi-fragments. These multi-fragments include free nucleons (FN's), light charged particles (LCP's) and Intermediate Mass Fragments (IMF's). The multiplicity of intermediate mass fragments and light charged particles indicates to the onset of multifragmentation and vaporization in nuclear matter.

In the present work, we shall explore phase transition in nuclear matter and associate its significance with various significants phenomenon in nuclear physics. Firstly, we shall study liquid-gas phase transition by extracting critical parameters τ and λ and study various other critical observables such as S_2, γ_2 and Z_{max2}. This study will reveal that whether the liquid-gas phase transition is dependent on the choice of clusterization algorithm or not. Results regarding this will be presented in chapter 3. Further in chapter 4, we shall extend our study by using energy based clusterization algorithm i.e., Simulated Annealing Clusterization Algorithm (SACA) and extract all the parameters related to

phase-transition. We shall also confront our results with experimental data for light and heavily charged systems.

Next, in chapter 5, we shall study the complete disassociation of system into lighter particles i.e., onset of vaporization. This study will be conducted using various clusterization algorithms. Further, we shall study the systematics of light particles and entropy production. The work will be spanned over the complete mass asymmetry and incident energy range. In chapter 6, we shall present the summary of the work along with an outlook.

Chapter 1

Review of phase-transition in heavy-ion collisions

The field of nuclear physics focuses on exploring various properties of atomic nuclei and outshines among the most generally thought about fields in science in the present era. One of the main motivation behind contemplating nuclear physics is to understand the properties of nuclear matter at the time of big bang or just after that [1, 2]. The Big Bang portrayed the development of the universe from the point when the temperature and density were extremely high and proffer the extensive description of phenomena associated with it. The origin of the universe from the huge explosion fuelled the enthusiasm of physicists and cosmologists to further progress in the field. To deal with the physics (behind the happenings that review the constituents and interactions associated with it), nuclear physics is considered as an unobtrusive branch.

Another objective of nuclear physics is to comprehend the properties of nuclear matter as well as of finite nuclei and to understand how the nuclear core is developed from the basic constituents. The nuclear matter is a naturally visible framework with the equivalent number of protons and neutrons. Further, these nucleons comprise of quarks and gluons that glue to each other through strong interactions. The massless gluons are responsible for the interactions among quarks. In addition, one also wonders whether nuclear matter, like fluid, can exist in different phases and whether there is a transition among different phases. The investigation about the phase-transitions in nuclear matter, therefore, has fascinated the scientists for a long time now. At low incident energies, the nuclear matter is studied as an analogue to liquid drop through the famous *liquid drop model*. Subsequently at intermediate and high incident energies, the properties and characteristics of nuclear matter resembles closely with that of ordinary matter, therefore, instigates one to explore

the field at a deeper level. The fundamental reason behind studying these transitions is to explore how the nuclear matter evolves through different phase-separation (*binodals*) and instability boundaries (*spinodals*) [3]. These phase-transitions are also crucial for understanding various astrophysical phenomena such as the dynamics of the supernova explosions as well as the formation of neutron stars [4]. In this thesis, we will explore liquid-gas phase transitions and various order parameters that predict these transitions in nuclear matter. We will also study the onset of vaporization and emission of light particles that will also be used to extract systematics on entropy production.

1.1 Statistical view of phase-transition

The statistical physics provides the framework for associating the microscopic features of each atom and molecule to the macroscopic properties that can be observed in daily life [5–7]. The fundamental laws of classical (macroscopic systems) or quantum mechanics (microscopic systems) govern the physics and dynamics involved behind the interactions between these atoms and molecules. Consequently, the thermodynamics is a natural outcome of the statistics. In thermodynamics, when the state variables such as pressure (P), volume (V), temperature (T), energy (E′), chemical potential (μ) etc. become independent of time, the system is said to be in thermodynamical equilibrium. To define it in a more refined way, one needs to understand the system at a microscopic level. At microscopic level, all the macroscopic objects are considered to be composed of atoms and molecules.

1.1.1 Phase-transition and critical phenomenon

The main objective of statistical physics is to determine the equation of state at a microscopic level by taking into account all the constituents and interactions of the thermodynamic system. Here a *phase* is defined as the state of matter in thermodynamic equilibrium. Depending upon the different macroscopic conditions, the thermodynamical variables can be classified into following two types:

- intensive variables : The value of these variables is independent of the amount of substance for which it is measured. These variables include pressure (P), temperature (T), volume (V), etc.
  and

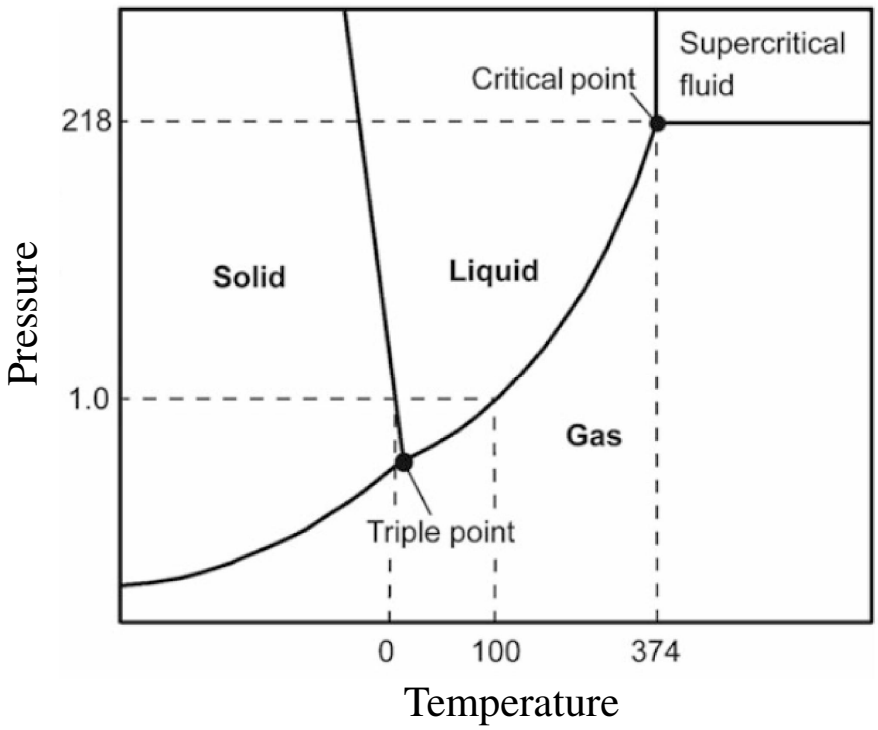

Figure 1.1: The Pressure-Temperature (P-T) phase diagram.

- extensive variables: The value of these variables depend on the amount of substance in the system or quantity contained in the system. These variables include energy (E′), entropy (S), free energy (F), specific heat (C_V) etc.

For one pair of these thermodynamical variables (such as Pressure-Temperature (P-T), Pressure-Volume (P-V), Temperature-Energy (T-E′) etc.), two phases can co-exist at the same time and attain thermodynamical equilibrium. Consequently, the co-existence of two phases and various characteristics associated with it marks the first-order phase transition. The phase diagrams between any two above discussed thermodynamical variables can be used to depict graphically the physical states of the matter under different conditions.

Fig. 1.1 illustrates the variations between different states of the matter as they relate Pressure-Temperature (P-T) phase diagram. In the figure, different phases are shown as solid, liquid and gas, respectively. The solid lines in the figure separate two phases and are also termed as phase equilibrium lines along which the two phases can co-exist simultaneously. The point where the three phases co-exist simultaneously is termed as "*triple point*" and another point where the distinction between liquid and vapor vanishes

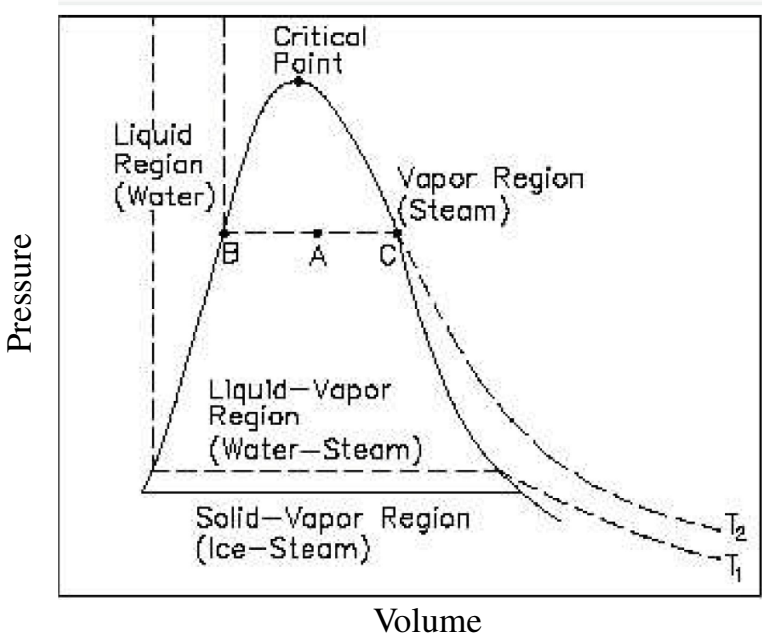

Figure 1.2: The Pressure-Volume (P-V) phase diagram.

is termed as the "*critical point*".

In Fig. 1.2, the Pressure-Volume (P-V) phase diagram depicts the isotherms at different temperatures (T_1 and T_2). The figure shows the existence of liquid region (water), the vapor region (steam) and coexistence of liquid and vapor region (water-steam) simultaneously. At low volume, the vertical curves represent the incompressible liquid whereas at high volume, the curves show the hyperbolic trend which denotes the vapor phase. The parallel isotherms at the mid volume show the simultaneous existence of both the liquid and vapor phases. In other words, coexistence of liquid and vapor phases happens at constant pressure. Further, as the temperature increases, the parallel portion of the curve decreases and ultimately at critical point, liquid-vapor co-existence disappears.

As per Ehrenfest criteria, the n_{th} order of the phase-transition corresponds to the discontinuity of the n_{th} derivative of free energy function. Thus, in a first-order transition, the first derivative of the free energy becomes discontinuous whereas in the second-order transition, the second derivative of the free energy diverges at the transition point.

In statistical physics, the free energy using partition function is described by the relation F= -$KT\ ln\ Q$, where F is the Helmholtz free energy, K is the Boltzmann constant and Q is the partition function of the given system. The first-order derivative of F with respect to T gives the discontinuity at the transition point if the system undergoes a first-order phase transition. The entropy (S) can be extracted from the temperature as:

$$S = -T\Big(\frac{\partial F}{\partial T}\Big). \tag{1.1}$$

Therefore, the entropy gives the first discontinuity at the transition point. The entropy "S" can also be expressed in the terms of latent heat. The first-order phase transition includes the latent heat that converts one phase into another without affecting the temperature of the system. From the Ehrenfest theory, it is clearly understood that for the second-order phase transition, the second derivative of the free energy will diverge at the critical point. The second-order derivative is related to the specific heat (C_V) that reads as:

$$C_V = -T\Big(\frac{\partial S}{\partial T}\Big), \tag{1.2}$$

where, C_V represents the specific heat at a constant volume. As shown in the above equation, C_V denotes discontinuity at the transition point for second-order derivative.

Another type of phase diagram i.e., Temperature-Energy (T-E′) phase diagram for ordinary and nuclear matter, is displayed in Figs. 1.3 (a) and (b), respectively. These curves are termed as caloric curves. In Fig. 1.3 (a), the matter exists in solid form at initial stage and temperature increases linearly with the energy and therefore, melts down into liquid form. With the further increase in the temperature, the curves becomes parallel to the energy axis (X-axis) and therefore, two phases co-exist simultaneously. Thereafter, further increase in the temperature leads to gas phase.

To study the phase-transition in nuclear matter, Pochdozalla *et al.* performed first experiment for heavy-ion reaction [8, 9]. For this experiment, the ALADIN forward spectrometer of GSI facility was used to induce ^{197}Au + ^{197}Au reaction at 600 MeV/nucleon. They studied the isotopic temperature (T_{HeLi}) as the function of excitation energy ($< E/A >$), here E is the excitation energy and A is the mass of the fireball. Note that the yield of He and Li produced the above given reaction is used to calculate the isotopic temperature (T_{HeLi}). Their results together with the results obtained by other experimental groups such as National Superconductor Cyclotron Laboratory (NSCL)-

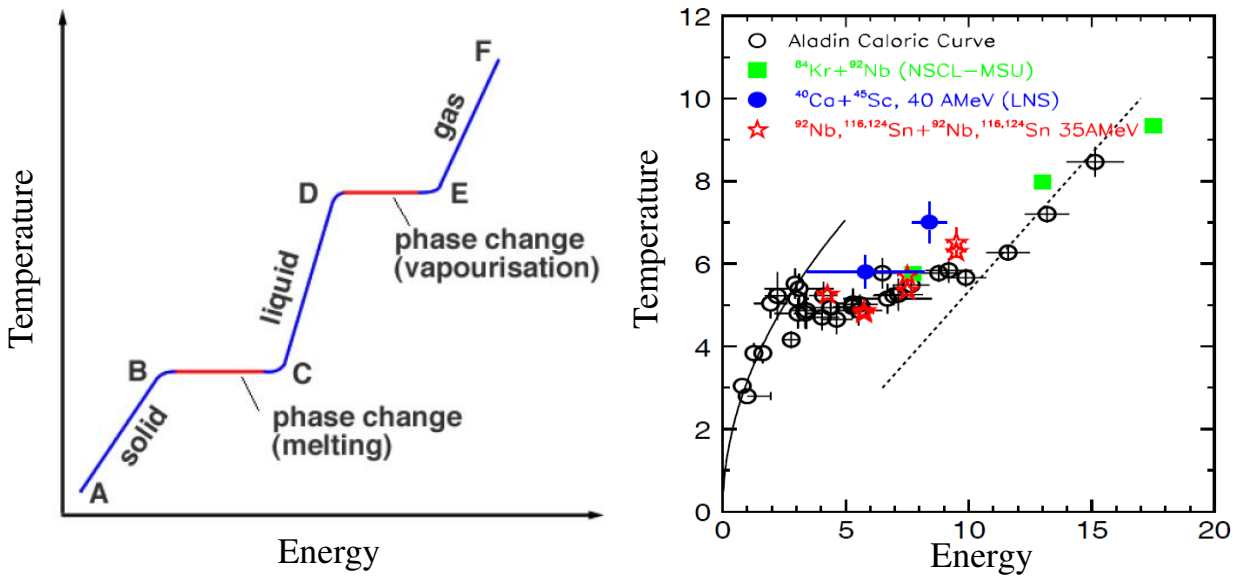

Figure 1.3: The Temperature-Energy (T-E′) phase diagram in ordinary and nuclear matter. " Reprinted (Fig. 1) with permission from M. D' Agostino *et al.*, Nuclear Physics A **749**, 55c-64c (2005), Copyright (2005) by the Elsevier".

Michigan State University (MSU), Laboratory of Nuclear Science (LNS) are also showed in Fig. 1.3 (b). One notices that the isotopic temperature increases sharply with the excitation energy for initial temperatures after which a plateau was reported at a fixed isotopic temperature ≈ 5 MeV for the broad range of excitation energy. This plateau was taken as a strong evidence for the liquid-gas phase transition in nuclear matter. For the further increase in the excitation energy, a linear rise in the temperature was obtained. Interestingly, the results were independent of the system masses. These results of nuclear matter were analogous to the well known behavior (i.e., phase-transition) in ordinary matter.

1.1.2 Phase-transitions in nuclear matter

The phase transitions in nuclear matter provide an unique edge to the nuclear and statistical physics. Phase-transitions in nuclear matter are exceptionally unique as they occur at a scale many orders of magnitude far from the ordinary matter. For the explicit description, a schematic representation of various phases of nuclear matter is displayed in Fig.

1.4 [10]. As shown in the figure, the nuclear matter exists as *liquid phase* in ground state. The point on the density axis (X-axis) in the figure corresponds to the normal state of the nuclear matter ($\rho = \rho_0$, T = 0 MeV) and the arrows define the trajectory followed by the universe after the big bang. In the liquid-phase, the nuclear matter is cold and exists in the ground state i.e., at low temperature and density. With the rise in the temperature and density, the particles of nuclear matter move freely like Van der Waal's gas, therefore, under specific conditions liquid-gas phase transition can be witnessed. When the density of nuclear matter is too high in comparison to the ground state (e.g., in neutron stars), this phase is often termed as *condensed phase*. The state where the temperature is fairly high with density being few times the normal nuclear matter density corresponds to the *gaseous phase*. The nuclei evaporates into hadron gas and further rise in the temperature can also lead to the second-order phase transitions. This phase corresponds to the highly compressed state of nuclear matter where density reaches up to 5 to 10 times the normal nuclear density and the temperature of around 150 MeV (or higher) is attained. In this phase, nuclear matter is highly compressed that makes hadrons to disassociate themselves into elementary particles and a de-confined mixture of quarks and gluons start appearing. This phase is termed as Quark Gluon Plasma (QGP) phase.

1.1.3 Equation of State (EOS) of nuclear matter

As mentioned above, the equation of state in nuclear matter can be expressed in terms of thermodynamical variables i.e., relation between pressure and volume of nuclear matter. The knowledge of the equation of state in the field of nuclear physics evoked the interest of both physicists and cosmologists to understand the range of phenomena happening at all energy scales. The equation of state helps to procure necessary physics behind phenomena such as multifragmentation, collective flow, stopping etc. and structure of nuclei far from the stability line whereas in astrophysics, it helps to understand the mechanism associated with supernova collapse and the structure of neutron stars. Hans Bethe and Carl Friedrich von Weizsäcker were pioneers in the field to introduce the concept of nuclear equation of state near the ground state conditions. Their results were formatted in the form of formula famously known as semi-empirical mass formula or liquid drop model [11]. Unfortunately, with the passage of time, it became clear that to pin down the nuclear equation of state is not straightforward. Further, the uncertainty in the experimental observations and also in the theoretical approaches has made the situation much more complicated than

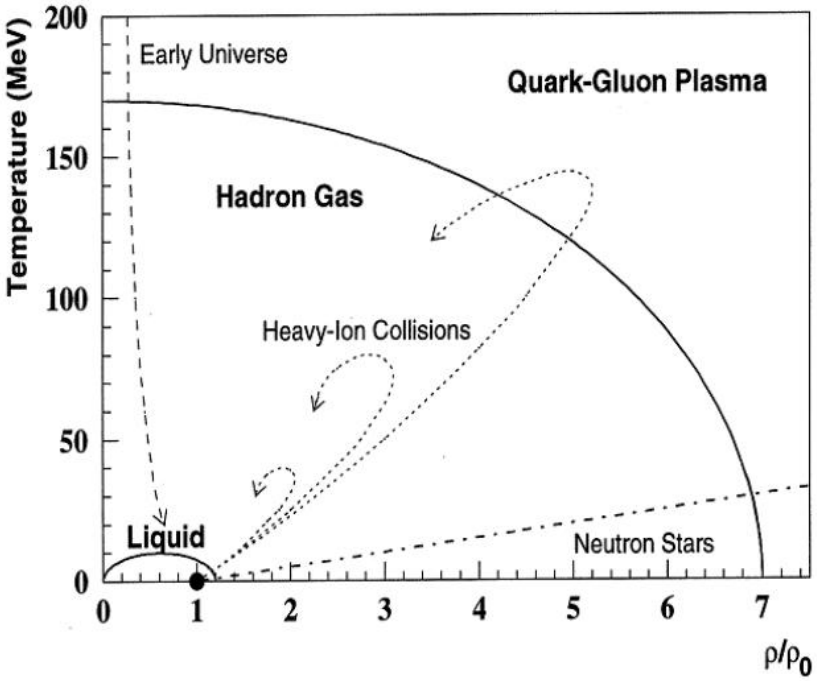

Figure 1.4: A schematic view of the phase diagram of nuclear matter. Here, Y-axis displays the temperature (in MeV) and X-axis displays the baryons density normalized to the density of the ground state of nuclear matter. This figure is taken from the Ref. [10].

was anticipated in early studies. The above situation becomes much complicated when one realizes that the compressed and hot stage in the nuclear matter stays for very short period of time and cannot be detected experimentally.

In another approach, the set of isotherms are used to define the equation of state (pressure versus density) that corresponds to nuclear forces. In Fig. 1.5, we display such curves for representation. These isotherms show the maximum-minimum behavior which is quite similar to Van der Waal's equation of state of real gases. Based on the interaction taken into account, the nuclear equation of state depicts the critical point at $\rho_c \approx 0.3$ - $0.4\ \rho_0$ and $T_c \approx 16$ - 18 MeV, where ρ_c and T_c represents the critical density and temperature, respectively. In Fig. 1.5, the area below the dotted line corresponds to the area of negative compressibility which implies that at a constant temperature, an increase in the density leads to decrease in the pressure [12]. However, in this area the single homogenous phase is unstable and system assimilates into liquid and gas phases. This assimilation into two phases corresponds to the spinodal instability. This instability is often mentioned as the cause behind the phenomenon of multifragmentation. The

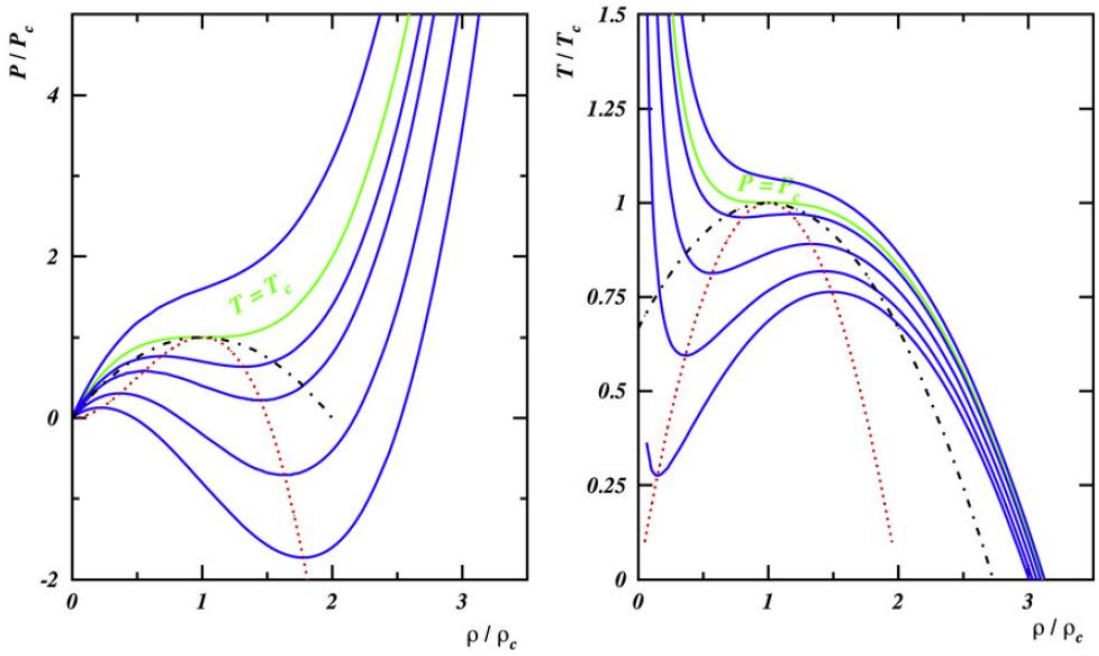

Figure 1.5: Equation of state corresponding to pressure or temperature and density (normalized to critical density) in nuclear matter. The dashed dotted lines are the co-existence lines and dotted lines the spinodal lines [12]. " Reprinted (Fig. 1) with permission from B. Borderie and M. F. Rivet, Progress in particle and nuclear physics **61**, 551-601 (2008), Copyright (2008) by the Elsevier".

considerable part of the co-existence of liquid and gas phases is present in the spinodal region. We likewise don't have any immediate method to measure the state variables (pressure (P), volume (V), temperature (T), energy (E′), etc.) for nuclear matter. As mentioned earlier, there are various methods to explore the highly dense state of nuclear matter indirectly. The finite nucleus and monopole vibrations generate slightly higher density than the normal nuclear density, so cannot be used to examine the situation at the extreme. On the other side, due to inaccessibility and rare occurrence of neutron star and supernova explosion, these cannot be taken as reliable sources for hot and dense state of nuclear matter. Therefore, owing to aptness to overcome all the limitations, heavy-ion collisions at intermediate energies are considered as the best tool to probe the state of compressed and dense nuclear matter state [1, 2].

1.2 Heavy-ion collisions

The progress in the field of nuclear physics led to the construction and commissioning of various accelerators that are capable of accelerating heavy-ions from few keVs to thousands of GeV/nucleon [13–15]. Concomitantly, the advanced detectors have been devised to detect charged as well as uncharged particles and reported the key role of heavy-ion collisions to probe the various aspects of dynamics associated with nuclear matter. Higher the incident energy, deeper and better insight into nuclear matter from atoms to nucleons and consequently, nucleons to quarks is possible [16–20].

In accordance with the incident energy of the projectile, heavy-ion collisions can be classified into three domains and its overview is discussed below: At low incident energies, the scattering of nucleons is expressed in terms of Brueckners's G-matrix. In this domain, the interaction potential is given in terms of G-matrix which can be subdivided into two parts i.e., real and imaginary parts. The real part acts like the potential whereas, imaginary part is proportional to the cross-section. The mechanism of reactions at low, intermediate and high energy depends strongly on the interplay between the real and imaginary parts of the interaction potential. At low incident energy (upto few MeV/nucleon) the contribution of imaginary part is too small to have meaningful and significant impact. At relativistic energy ($\geq$ few GeV/nucleon), the imaginary part of the potential dominates. This is attributed to the reduced number of blocked collisions due to available free momentum space. Contrarily, at intermediate energies (in between few MeV/nucleon and GeV/nucleon), both the real and imaginary parts play the key role in deciding the dynamics of a reaction. The cause behind the keen interest in the low energy domain ($E_{lab} < 10$ MeV/nucleon) is to understand the process of fusion [21, 22], fission [23], cluster radioactivity [24], emission of beta and gamma rays [25, 26], synthesization of super-heavy nuclei [27, 28] as well as to explore the features of exotic nuclei formed during the reaction [29]. Here, the real part of the potential i.e., mean-field plays the decisive role. As a result, initial nucleon-nucleon correlations are preserved for the longer duration. Contrarily, in the high energy domain ($E_{lab} > 2$ GeV/nucleon), the sub-nucleonic degrees of freedom becomes dominant. The binary hard collisions among nucleons destroy the initial correlations among nucleons and therefore, nuclear matter equilibrates early and fast. The main motive to study the reactions in this regime is to understand the interactions between quarks and also to explore the existence of quark-gluon plasma [30, 31].

In the intermediate energy domain, the energy of the projectile is such that none of the real and imaginary parts has decisive dominance. In this energy domain, both binary collisions as well as mean-field play equally important role. The nuclei at normal density and zero temperature behave like a Fermi liquid, therefore, liquid to gas phase transition can possibly be observed in these reactions. Subsequently, the second phase-transition is witnessed by the nuclear matter at high temperature and density. Here, one observes the transition from the hadronic matter to Quark Gluon Plasma (QGP) phase. The reactions in this density-temperature range also provide an unique edge to determine the exact nature of the equation of state. The great efforts have been put by large number of scientists performing experiments at high energy all around the world at Conseil European pour la Recherche Nucleaire (CERN) at Geneva in Switzerland and Brookhaven National Laboratory (BNL) at New York, United States of America (USA). In this thesis, we will constrain our study to heavy-ion collisions at intermediate energy only.

1.2.1 Multifragmentation

When the incident energy of the projectile is comparable to its binding energy, a thermalized (and concentrated) state of nuclear matter may form. This thermalized state of the nuclear matter gets consolidated by the outflow into the extensive number of varied size fragments. This complete phenomenon is termed as multifragmentation [12, 32–35]. The compressed state of nuclear matter exists for a very short time scale. After the compression phase, the expansion of the nuclear matter occurs that leads to the production of fragments of various sizes. In Fig. 1.6, a schematic representation of the multifragmentation as a function of time scale of a reaction is depicted. In the figure, the projectile and target collide at certain incident energy and forms a pre-equilibrium compressed state for a very short time scale (10^{-22} sec). The pressure gradient developed in the compressed state leads to the fragmentation of the system. Further, these fragments stabilize through secondary decays.

At low incident energy, the reacting partners (projectile and target) do not have sufficient energy to break into fragments. In comparison, at high incident energy the excitation energy is too high and does not permit fragments to survive. At intermediate energy, the excitation energy is sufficient to produce large number of fragments therefore, studying reactions at intermediate energies is an ideal situation [12, 32]. It is well known that the multiplicity of fragments is reliant strongly on the various entrance channel pa-

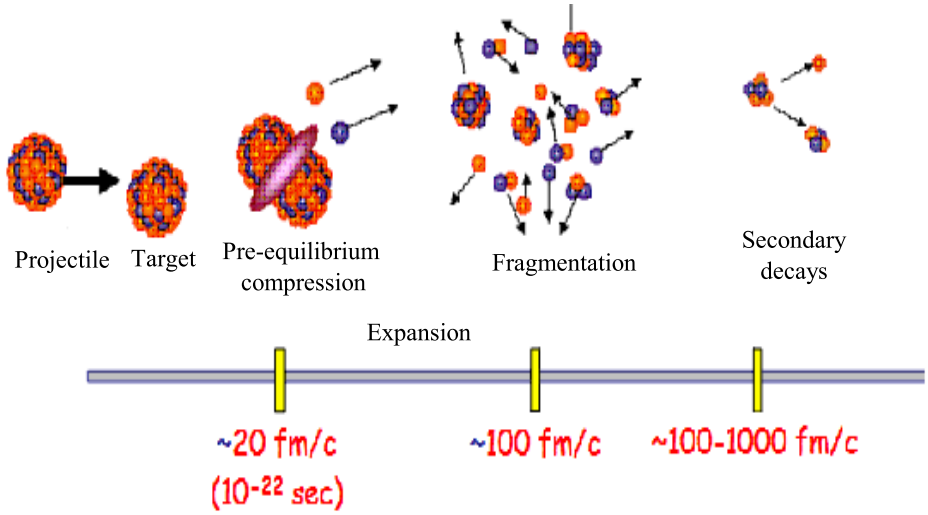

Figure 1.6: A pictorial representation of phenomenon of multifragmentation

rameters such as mass of the colliding nuclei, incident energy of the colliding system, colliding geometry, binding energy, isospin asymmetry, etc. For the better understanding of the dynamics behind the fragmentation, one often classifies the fragments based on the mass and/or charges. In the literature, one often has Free Nucleons (FN's)[A_f=1], Light Charged Particles (LCP's) [2≤A_f≤4], Medium Mass Fragments (MMF's)[5≤A_f≤9], Heavy Mass Fragments (HMF's) (10≤A_f≤A_T/6) and also Intermediate Mass Fragments (IMF's) [5≤A_f≤A_T/6, where A_f represents the mass of the fragment and A_T signifies the total system size/mass]. It should be noted that one often takes charge into consideration when experimental studies are performed. These fragments of different sizes are rich source of information.

The multifragmentation has been considered as an effective probe to contemplate various observables. The phenomenon of multifragmentation can also be explained on the basis of the liquid-gas phase transition. The thermodynamical properties associated with the hot nuclear matter and finite nuclei can be studied through various methods that incorporate phenomenological approaches [36, 37], variational methods [38], the Hartree Fock theory [39], the Thomas-Fermi approximation [40], the relativistic mean-field models [41] as well as the quasi-particle approximation [42]. These approaches revealed the similarity between the equation of state of hot nuclear matter and Van der Waal's forces of ordinary matter. Also, many studies done in the past predicted liquid-gas phase transition but the characteristics related to its exact nature are still unknown [12, 32–35]. For

instance, different calculations done in the literature show fluctuation in the critical temperature T_c [32, 33]. For adequately low temperature and low density, the liquid-gas phase transition is observed in form of droplets whereas at high density and temperature, this transition leads to bubble phase. These droplets are frequently termed as fragments and the mass/charge yield of these fragments strongly assist one to study various parameters related to the liquid-gas phase transition [43–50]. Further, the bubbles correspond to very light fragments formed at high energy that can be interlinked to the onset of vaporization in the nuclear matter. It is well known that the light particles carry vital information about the early phase of the reaction as they are formed at the every stage of the reaction and determine the degree of the equilibration of nuclear matter. The entropy is one such significant observable that shed light on the early stage of the hot and dense state of nuclear matter and also on the equilibration reached. As well as, the entropy production in a heavy-ion reaction is observed to shed light on the fragment formation and on the onset of vaporization. Detailed studies were also documented to find the entropy production in nuclear reactions [51–56].

1.3 Features of fragmentation

1.3.1 Mass distribution

The mass distribution exhibits variation of the multiplicity of the fragments. The knowledge of the mass distribution of fragments is essential to investigate the fragmentation pattern. This distribution can easily be computed through experiments. The Figs. 1.7 (a), (b), (c), (d) show the mass distribution at four freeze-out temperatures (T = 6.5, 7.5, 10 and 14 MeV) for the fireball having mass of 192 units. The mass distribution shows 'U'-shaped curve at low temperature of T = 6.5 MeV, that predicts the presence of both light and heavy mass fragments. At slightly higher temperature, the curve deviates from 'U'-shape and shows the production of intermediate mass fragments. At still higher temperature i.e., T = 10 MeV, one sees monotonous decrease with negative slope that steepens with further rise in the temperature.

1.3.2 Intermediate mass fragments

The multiplicity of Intermediate Mass Fragments (IMFs) is considered as one of the most prominent feature to study the physics behind various phenomena. These fragments carry

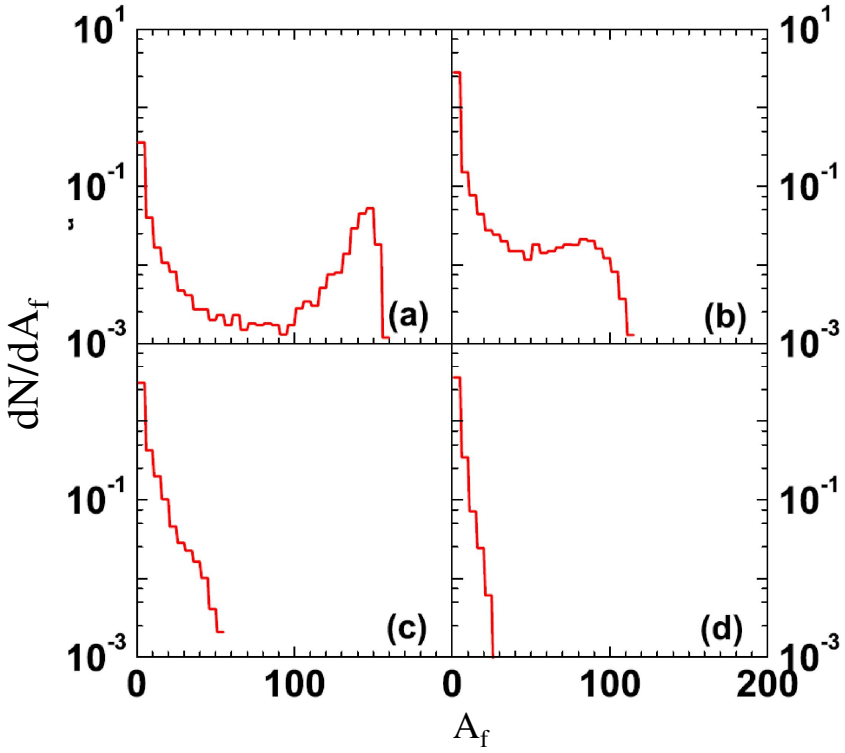

Figure 1.7: The mass distribution of fragments using Canonical Thermodynamical model (CTM) calculation for a fireball (system mass = 192) at a temperature (a) 6.5 MeV (b) 7.5 MeV (c) 10 MeV and (d) 14 MeV. " Reprinted (Fig. 2) with permission from S. Mallik, S. Das Gupta and G. Choudhuri, Physical Review C **91**, 034616 (2015), Copyright (2015) by the American Physical Society".

no hereditary of the colliding nuclei and are heavier than the alpha particles but lighter than the fission fragments. The multiplicity of IMFs plays a key role in understanding the dynamics of fragmentation pattern. In Fig. 1.8, we display the IMFs multiplicity as a function of incident energy. A "rise and fall" behavior of the IMFs with incident energy of the projectile has been observed [57]. Interestingly, both statistical and dynamical models calculations have reported the emission of Intermediate Mass Fragments as most significant signature to analyze the liquid-gas phase transition.

1.3.3 Liquid-gas phase transition

In several studies reported in the past, the multifragmentation has been closely interlinked with the liquid-gas phase transition in nuclear matter [43, 44, 46]. The phase-transition in the ordinary matter is generally defined for the macroscopic system in the thermodynamic limit. Since nuclear system in a reaction is composed of few hundred of nucleons; therefore

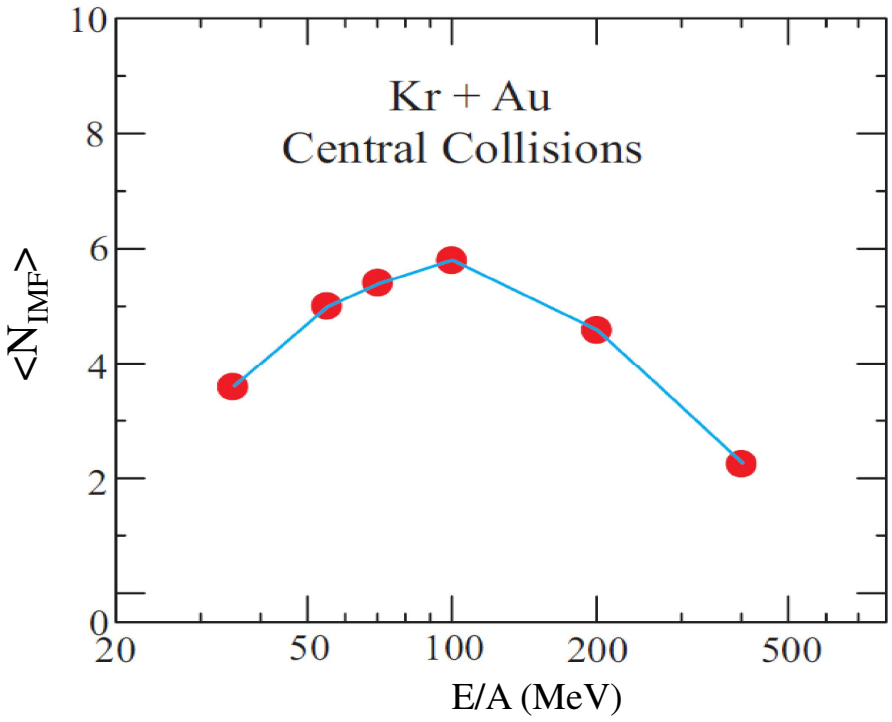

Figure 1.8: The multiplicity of IMFs as a function of incident energy for the central collisions for ^{84}Kr+^{197}Au [57]. The <N$_{IMF}$> and E/A represent the multiplicity of IMF's and excitation energy of the system, respectively. " Reprinted (Fig. 2) with permission from G. F. Peaslee *et al.*, Physical Review C **49**, R2271 (1994), Copyright (1994) by the American Physical Society".

the term "phase-transition" is only legitimate for the finite nuclear system with long-range Coulomb interactions.

In heavy-ion collisions at intermediate energy domain, it is considered that liquid-gas phase transition does occur. The formation of small chunks after the reaction (chunks are generally termed as fragments) is considered to contain signals of such liquid-gas phase transitions. As discussed above, mass yield curve at low incident energy points toward the presence of both light and heavy mass fragments, thus the co-existence of both liquid and gas phase can be observed. It was found that fragment mass/charge yield when fitted as a function of mass (A_f)/charge (Z_f) of fragments obeys such power-law at certain excitation energy which is also signal for the liquid-gas phase transition [43, 44, 46]. The value of incident energy at which power-law [$Y(A_f) \propto {A_f}^{-\tau}$] or [$Y(Z_f) \propto {Z_f}^{-\tau}$] appears has been termed as critical energy or the energy of the *onset of multifragmentation*. The Purdue experimental group noted such signal in their experiments [58]. This kind of

behavior of fragments was earlier predicted in the Fisher's droplet model calculations and was later on confirmed in various other theoretical calculations [44–46]. The value of critical energy is estimated by looking for the minimum in the power-law parameter "τ" when plotted as a function of incident energy. One should keep into the mind that the extraction of critical exponent and its power-law behavior is not sufficient evidence for the liquid-gas phase transition. Therefore, various other observables such as moments of the charge distribution, Campi scatter plots, multiplicity derivative of the largest fragment as well as the fluctuations in the charge of the second largest fragment and many other observables have been devised in the literature to study liquid-gas phase transition through multifragmentation.

1.3.4 Onset of vaporization

From the studies of ordinary matter, it is quite evident that at high incident energies the phase-transition leads to vapor phase. Coincidingly, the dynamics of the heavy-ion reactions is also governed by the incident energy of the projectile. After the critical point, the slope parameter τ keeps on increasing with incident energy and at certain higher incident energy almost all the correlations among nucleons break down. This particular energy has been identified in the literature as the energy of *onset of vaporization*. Such phenomenon was predicted for the first time by Peliert *et al.* [59] and later on was confirmed in experimental studies of ^{16}O+^{80}Br at GSI, Germany [35]. In another attempt, Souza *et al.* [60] performed much elaborated study of the onset of vaporization by defining the average charge of the fragments as an observable. Seldom is the case, that the onset of vaporization is investigated in detail. Though, it should be noted here that the energy at which the onset of vaporization occurs is of great importance as it determines the strength of the nucleon-nucleon correlations that is used to determine nuclear potentials.

For the better clarity of phase-transition in nuclear matter, the evolution of fragment mass distributions with increasing temperature of initial nucleus is shown in Fig. 1.9. The multiplicity (dN/dA_f) as a function of fragment mass (A_f) is displayed in the figure. At low temperatures (T $\leq$ 1-2 MeV), mass distribution corresponds to the liquid phase (evaporation in compound nucleus) of the nuclear matter. The fission peak can also be clearly observed in the figure which indicates the presence of heavy nuclei. With further increase in temperature, the peaks get broaden and consequently turn into U-shape at T$\approx$ 5 MeV. The mass distribution follows the power-law ($Y(A_f) \propto {A_f}^{-\tau}$) behavior at

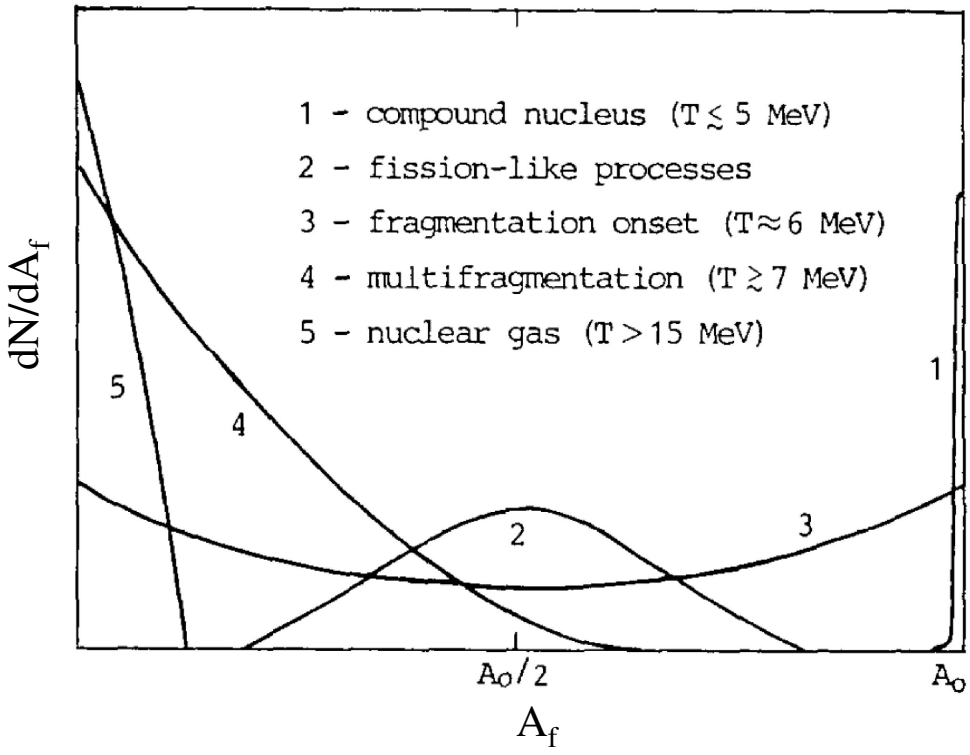

Figure 1.9: Types of disintegration phenomenon associated to the average multiplicity as a function of mass of produced fragments. " Reprinted (Fig. 5.10) with permission from J. P. Bondorf *et al.,* Physics Reports **257**, 133-221 (1995), Copyright (1995) by the Elsevier".

temperature about T = 5-7 MeV. The critical exponent "τ" extracted from the power law distribution shows minimum with incident energy which is defined as the point of onset of multifragmentation [43–46]. At temperature T = 7-15 MeV, the mass distribution shows the steep decrease in curve which reflects the emission of intermediate mass fragments and therefore, coexistence of liquid-gas phase in nuclear matter. With further rise in the temperature (T = 15 MeV), the curve shows the exponential fall in the multiplicity reflecting the dominance of light particles i.e., onset of vaporization in nuclear matter.

1.3.5 Entropy production

As mentioned earlier, the entropy shows the discontinuity at the point of first-order phase transition in ordinary matter. Also, the light particles in vaporization phase assist one to compute the entropy production in nuclear matter [53]. Therefore, it is considered as a significant observable to determine the degree of thermalization in nuclear heavy-

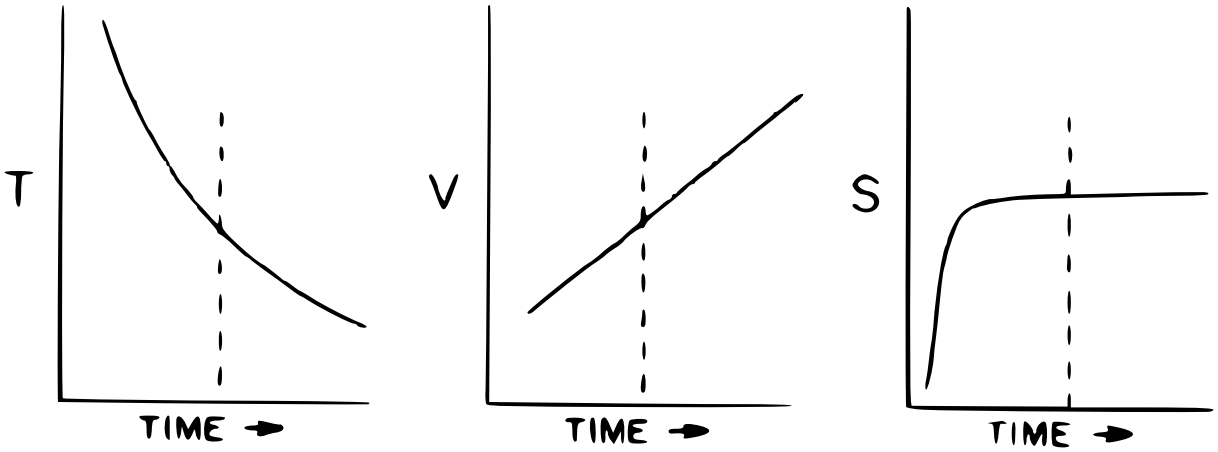

Figure 1.10: The Temperature, Volume and Entropy as function of time [54]. " Reprinted (Fig. 1) with permission from G. F. Bertsch *et al.,* Nuclear Physics A **400**, 221c-232c (1983), Copyright (1983) by the Elsevier".

ion reactions through multifragmentation at intermediate energy. The time evolution of thermodynamical variables such as temperature (T), volume (V) and entropy (S) is displayed in Fig. 1.10. The existence of compressed state of nuclear matter during heavy-ion collisions is for a very short duration. The compressed state leads to high density and large part of kinetic energy gets converted into thermal excitation energy that leads to an increase in the randomness of the system. The phase after the compressed state of nuclear matter witness negligible change in the entropy (as shown in Fig. 1.10). Therefore, entropy production provides an opportunity to study the early phase of the hot and dense nuclear matter. Siemen and Kapusta in 1979, reported that generalized entropy can be deduced from the deuteron to proton ratio [53]. Due to the unaltered behavior of entropy till the end of the reaction, they insisted on the use of entropy else than other variables for thermodynamic analysis. Additionally, the entropy production in a heavy-ion reaction is also observed to shed light on the fragment formation. Detailed studies were also documented to find the entropy production in nuclear reactions [51–56, 59, 61–64].

1.4 Experimental review of multifragmentation

1.4.1 Features of detectors (specifically 4π detectors)

In this section, we essentially focus on the basic requirements and physical objectives of the experiments at intermediate energies. As the work presented in this thesis, is based

on the comparison with experimental data specifically from 4π detector, therefore, we will take into account features of 4π multi-detectors around us. For example, FOPI detector at GSI, the INDRA detector (a 4π -light charged particle and fragment multi-detector built in 1989 at GANIL, the MSU 4π detector etc.) are accessible for heavy-ion reactions.

The reacting partners (i.e., projectile and target) at low incident energy conserve their identity and the internal quantum states, whereas in reactions at relativistic energies the assortment of smaller entities in the reactions is quite large. Additionally, reactions at intermediate energies lead to the production of large number of varied sized fragments and one can likewise, observe the production of strange particles also [65, 66].

The primary objective to perform any experiment is event-by-event detection and simultaneous measurement of all the emitted particles. The known experimental detectors (such as MSU 4π detector, the Bevalac Plastic Ball detector and large array detectors at CERN and BNL heavy-ion reaction experiments) are strictly based on this procedure. Likewise, irrespective of set up, the detector of constrained size and geometry are incapable to determine (forward or backward) emitted particles sharply along the beam-line. The alignment of detectors is slightly out of vacuum region where the target is placed. Due to this reason, the particles with lower kinetic energies (soft particles) are not able to penetrate the vacuum region. Consequently, due to the restricted acceptance of detectors, it is hard to reproduce the spectrum of the emitted particles. However, an appropriate arrangement of events is required. Presently, we will discuss couple of fundamental steps required to be followed for complete management of events in experimental studies.

1.4.2 Event selection

The nuclear physics experiments aim to assemble information about various nuclear interactions happening in the core of the nucleus. When nuclear particles pass through the detectors they are detected by various electrical signals. The signals carry information about their type, energy and trajectory. The data acquisition system digitizes, formats and stores the information so that it can be used further for data analysis. Out of thousand to million events occurring per second only very few events are useful, so experiments needs proper sorting of "well measured events".

It is significant to mention here, mainly in the 4π multi-detectors, the direct relation between the violence of collisions and the centrality of the reactions can be used to choose the events with different impact parameter (as mentioned in Refs. [67, 68]. But

experimentally, the violence of the collisions cannot be examined directly. Therefore, the multiplicity of various particles can give proper measurement of impact parameter. The measured multiplicity of charged particles (N_c) indicates about the centrality (impact parameter) of the reaction. However, the charged particle multiplicity (N_c) and the impact parameter are inversely proportional to each other. Further, we will briefly discuss few of the other quantities related to event sorting:

1.4.3 Event trigger

The event triggers in experiments deal with the loss of particles or particles which are not distinguished because of poor count in the detector. The triggering system can be used to select events by taking into consideration the multiplicity of particles in any 4π-array. Note that, in few cases there is a need of higher multiplicity and thus, combination of various runs may take place with other reactions of similar type. Therefore, event trigger assist in selecting the proper number of collisions with the desired multiplicity.

1.4.4 Physical data storage

The physical data storage in the detector transforms the primary data set into physical data set to investigate various features of detected particles in heavy-ion reactions. The physical data set (as reported in Ref. [67]) comprises of detected particles and their features such as species, charge, energy, momentum, etc. This device is also utilized to store all the features of the emitted particles. With the assistance of this stored data set, one can compute the desired cross-section, interactions among different particles, momentum dependence of nucleon-nucleon interactions and some other observables that can be measured.

1.4.5 Determination of impact parameter

The impact parameter cannot be measured directly. Therefore, to extract exact value of the impact parameter and to know the centrality of the reaction, various techniques need to be developed. As phenomenon of multifragmentation is highly reliant on the geometry of the colliding system, so it is very pivotal to gain proper knowledge associated with accurate estimation of the impact parameter. This is attributed to the fact that as the impact parameter decreases the overlap volume of the colliding partner (projectile and

target) increases and thus, affects the results of the experiment drastically [12, 32, 43, 47, 69–71].

Some quantities that assist in extracting the information about the measurement of impact parameter are:

- *The ratio of transverse and longitudinal kinetic energy (E_{RAT})*:

  This technique is utilized by different experimental groups to deal with the sorting of data which is based on the cuts in global variable distribution. The multiplicity of charged particles and E_{RAT} (ratio of transverse and longitudinal kinetic energy) is used to select impact parameter range [72]. It is defined as:

$$E_{RAT} = \frac{\sum_i^{\perp} E_i}{\sum_i^{\parallel} E_i}|_{y \geq y_{cm}}. \tag{1.3}$$

  Here y_{cm} is the center of mass rapidity of different fragments.

- *The charged particle multiplicity (N_c)*:

  All charged particles detected by 4π detectors are defined using this quantity [67, 68]. Since the single detector considers all the multi-hits as single hits, regardless of whether they can be distinguished as double hits. Therefore, the count N_c is close counterpart to the multiplicity of detectors in which at least one charged particle is detected in a given event. This quantity is frequently utilized by various distinctive research collaborations (for instance, GSI and FOPI) to sort out events [72] .

- *The total transverse kinetic energy of identical particles* [67, 68, 72]:

  This quantity is also used to determine the impact parameter. The E_t is defined as:

$$E_t = \sum_{i=1}^{N_c} E_i \times sin\theta_i{}^2 = \sum_i \frac{(p_i sin\theta_i)^2}{2m_i}. \tag{1.4}$$

  Here E_i, p_i, θ_i and N_c are the kinetic energy, momentum, emission angle of 'i^{th}' particle with respect to the beam axis and the charged particles multiplicity, respectively. The experimentally determined impact parameter is used to express the cross-section by assuming the geometrical correspondence between E_t and impact parameter. Also, the largest value of E_t relates to the most central collisions [73].

- *The mid-rapidity summed charge, Z_y*

This quantity is defined as the sum of all identified particles of rapidity 'y' with $0.25\ y_{cm} \leq y \leq 0.75\ y_{proj} + 0.25\ y_{cm}$, y_{cm} and y_{proj} depict the rapidities of the total center-of-mass system and of projectile, respectively. The rapidity of the particle is defined as:

$$Y = \frac{1}{2} ln \frac{E + p_Z}{E - p_Z}, \tag{1.5}$$

here, E and p_Z are the total energy of the particle and the total longitudinal impulsion, respectively.

Note that all the quantities discussed above are interlinked with each other. In the next section, we will discuss various theoretical and experimental endeavors done in the past to contemplate multifragmentation [74].

A substantial number of experimental endeavors have been done and many are in progress to comprehend the properties of the hot and dense compressed state of nuclear matter. The first experiment to study the phenomenon of multifragmentation was performed using cosmic rays (naturally accelerated beams) [34, 75]. Since the cosmic rays comprise of variety of projectiles of different masses, charges, as well as energies, thus, constrained the experiments to be inclusive. Also, to perform exclusive experiments the specified nuclei with a fixed amount of excitation energy was a prerequisite but this was feasible through accelerators only.

In the mid 70's, the Bevatron when joined to linear accelerator SuperHILAC (named as BEVALAC) at Lawrence Berkeley Laboratory was the early accelerator available to accelerate heavy-ions to relativistic energies . This further led to the construction of various high energy accelerators at Michigan State University (MSU), Michigan, USA, Grand Accelerateur National D'ions Lourds (GANIL) at Caen, France, Relativistic Heavy-Ion Collider (RHIC) at Brookhaven National Laboratory (BNL), New York, USA, NSF-Arizona accelerator at university of Arizona, Tucson, USA, Vivitron accelerator at Oak Ridge National Laboratory Strasbourg, France, Superconducting Cyclotron (SC) at Texas, Michigan, USA, Superconducting cyclotron at INFN, Catania, Italy, Heavy-ion Synchrotron (SIS) accelerator at GSI, Darmstadt, Germany and Charged Heavy Ion Mass and Energy Resolving Array (CHIMERA) detector at Laboratori Nazionali del Sud in INFN, Catania, Italy. These accelerators gave extraordinary plausibility to perform heavy-ion collisions under controlled conditions and led to exclusive experiments. It is important to mention here that these experiments utilize the range of experimental setups, that are

exceptionally complex in nature.

As mentioned earlier, the cosmic rays were also used in the past to study multifragmentation and the reactions also analyzed the emission of fragments that are heavier than alpha particles but lighter than fission fragments. The ionization chambers and Geiger counters were used as detectors. Subsequently, the phenomenon of multifragmentation was also studied using synchro-cyclotron, proton beams at relativistic energies on emulsions [76]. The multiplicity, charge distribution, energy distribution, and angular correlations were determined to study the fragmentation of colliding nuclei. Similarly, Jakobsson *et al.* conducted emulsion experiments and proposed exclusive data on multifragmentation [34]. The study done through this experiment extended over the complete range of phenomena occurring in nuclear matter i.e., the onset of nuclear multifragmentation to nuclear vaporization in heavy-ion collisions. Another experiment at Berkeley, USA, observed the emanation of IMF's when emulsion was illuminated by carbon beam at 250 MeV/nucleon. The motivation behind this experiment was to examine the high multiplicity of ^{12}C reactions at intermediate energy.

The work done at Berkeley lab at Lawrence Berkeley Laboratory (LBL), mainly concentrates around the dynamics of asymmetric reactions such as $^{36}_{18}$Ar+$^{197}_{79}$Au, $^{56}_{26}$Fe+$^{197}_{79}$Au, $^{139}_{57}$La+$^{12}_{6}$C, $^{40}_{20}$Ca, $^{64}_{29}$Cu, $^{139}_{57}$La, $^{197}_{79}$Au+$^{27}_{13}$Al, $^{51}_{23}$V, $^{64}_{29}$Cu . These experiments were performed in the incident energy range between 35 and 110 MeV/nucleon [77–81]. The major aim to perform these experiments was to examine the role of entrance channel mass asymmetry on the reaction dynamics. These experiments also focussed on the various attributes such as charge distribution, incident energy, angular distribution, cross-section of different fragments as well as velocity distribution by varying the asymmetry of the reactions. Consequently, the Equation of State (EOS) collaboration at BEVALAC have also made efforts to determine phase-transition in nuclear matter through the phenomenon of multifragmentation. In the similar way, various critical exponents have also been investigated by colliding $^{84}_{36}$Kr, $^{139}_{57}$La and $^{197}_{79}$Au projectiles on the fixed $^{12}_{6}$C target. The research was further extended to determine critical exponents such as volume energy, surface energy, entropy, etc. [82] for symmetric reactions of $^{197}_{79}$Au+$^{197}_{79}$Au over the entire incident energy range that spans from 400-1000 MeV/nucleon [83].

The National Superconducting Cyclotron Laboratory (NSCL) of Michigan State University (MSU), was another prominent group to perform experiments using asymmetric reactions. Specifically, the MSU group emphasized on the reactions of $^{129}_{54}$Xe + $^{12}_{6}$C, $^{27}_{13}$Al,

$^{51}_{23}$V, $^{64}_{29}$Cu, $^{89}_{39}$Y (50 MeV/nucleon), $^{36}_{18}$Ar + $^{197}_{79}$Au, $^{129}_{54}$Xe + $^{197}_{79}$Au (50 - 110 MeV/nucleon), $^{36}_{18}$Ar + $^{64}_{29}$Cu, $^{108}_{47}$Ag, $^{197}_{79}$Au (17 - 115 MeV/nucleon) [46, 49, 68, 84–87]. The major goal behind performing these experiments was to determine average multiplicities, spectral slopes and masses of heavier fragments. Besides asymmetric reactions, efforts were also made by the group to include nearly symmetric reactions such as $^{20}_{10}$Ne + $^{27}_{13}$Al, $^{20}_{10}$Ne + $^{45}_{21}$Sc, $^{84}_{36}$Kr + $^{93}_{41}$Nb, $^{129}_{54}$Xe + $^{129}_{57}$La in the incident energy range of 15 and 135 MeV/nucleon [88–90]. Lately, to study isospin effects this group also performed an experiment with $^{112}_{50}$Sn + $^{112}_{50}$Sn and $^{124}_{50}$Sn + $^{124}_{50}$Sn reactions at 50 MeV/nucleon [91–94]. Another study done at Michigan State University (MSU) analyzed the charge distribution for the symmetric reaction of ^{45}Ar + ^{45}Sc in the incident energy range from 35 to 115 MeV/nucleon. They extracted power law parameter "τ" and exponential parameter "λ" from the charge distribution to study liquid-gas phase transition in nuclear matter [87]. This study was further extended for asymmetric reaction of ^{84}Kr+^{197}Au in the incident energy range from 35 - 400 MeV [49].

Among various important experimental groups, A Large Acceptance Dipole magNet (ALADiN) and FOur PI (FOPI) at GSI were also ones to examine various features associated with fragmentation. The study done by these groups incorporate the complete systematics of the reaction between $^{12}_{6}$C and $^{208}_{84}$Pb from lower to higher incident energy ranging from 100 to 1000 MeV/nucleon [43, 49, 57, 70, 71, 95–97]. Further, the study was extended by fixing the target to $^{197}_{79}$Au but changing the mass of the projectile. In this broad range of incident energy, they covered the complete range of phenomena happening at the various stages of nuclear matter i.e., evaporation to the emission of fragments and complete disassembly of the nuclear matter. The study was extended further and the results reported the "rise and fall" feature of IMFs when plotted as a function of incident energy [57] and impact parameter [71, 97]. Another marked feature, " universality", was reported by this group after studying the behavior of fragment multiplicities and fragment correlations with Z_{bound} (where Z_{bound} is the total sum of the charge of all the fragments with $Z_f \geq 2$)[71, 96].

The 4π multidetector Identification de Noyaux et Detection avec Resolution Array (INDRA) group at GANIL, constructed in the early nineties intended to investigate the dynamics of hot and dense nuclei that further cools by multifragmentation. It is another significant group that has made remarkable progress in the field of nuclear physics. They gave prominence to the role of various entrance channels and other parameters of multi-

fragmentation. The group mainly analyzed the asymmetric reactions of $^{36}_{18}$Ar + KCl, $^{36}_{18}$Ar + $^{58}_{28}$Ni, $^{129}_{54}$Xe + $^{nat}_{50}$Sn, $^{208}_{82}$Pb + $^{197}_{79}$Au and $^{155}_{64}$Gd + $^{238}_{92}$U in the incident energy range of 32 - 90 MeV/nucleon [98, 99]. They also focussed on the detailed investigation of the dynamics for the symmetric reactions of ^{36}Ar on ^{58}Ni and the role of various mass asymmetries was also studied by this group. The characteristics indicating the liquid-gas phase transition have been studied through the dynamical (spinodal instability) and thermodynamical parameters (microcanonical heat capacity) in the multifragmentation phenomenon [100]. They have also given various signals of a first-order phase transition in finite non-extensive systems. These signals include dynamics of the transition (spinodal fluctuations), negative heat capacity, bimodality of the size distribution of the heaviest fragment, extraction of the coexistence zone of the transition, the first estimate of the associated latent heat dynamics of the transition in relation with the introduction of the N/Z degree of freedom and neutron enrichment of the gas phase [101, 102]. Lately, another data was reproduced for symmetric reactions i.e., $^{197}_{79}$Au+$^{197}_{79}$Au reaction in the incident energy range between 40 - 50 MeV/nucleon [103].

In this direction, strong effort has been done by TAMU - Neutron Ion Multidetector for Reaction Oriented Dynamics (NIMROD) to study heavy-ion collisions in the Fermi-energy region [74]. The experimental work extracted various parameters i.e., multiplicity distribution, charge and mass distribution, momentum distribution, kinetic energy spectra, velocity, and temperature for $^{60}_{30}$Zn + $^{58}_{28}$Ni (at 26 MeV/nucleon), $^{197}_{79}$Au (at 47 MeV/nucleon), $^{60}_{30}$Zn + $^{92}_{42}$Mo (at 35 and 47 MeV/nucleon), $^{27}_{13}$Al + $^{112}_{50}$Sn (at 55 MeV/nucleon), $^{40}_{18}$Ar + $^{27}_{13}$Al, $^{48}_{22}$Ti, $^{58}_{28}$Ni (at an incident energy of 47 MeV/nucleon) and $^{40}_{18}$Ar + $^{112}_{50}$Sn (at an incident energy of 40 MeV/nucleon) [109–112]. Another approach has given strong evidence of liquid-gas phase transition by extracting the critical parameter for nearly symmetric reactions $^{40}_{18}$Ar + $^{27}_{13}$Al [44]. To extend study further, various other observables such as Campi plots, fluctuations in Z_{max} etc. using reactions of $^{40}_{18}$Ar + ^{27}Al, ^{28}Ti and ^{58}Ni at 47 MeV/nucleon were analyzed by this group to study liquid-gas phase transition in nuclear matter [45]. Also various parameters for symmetry energy such as isotopic and isobaric yield ratio, neutron to proton ratio (n/p) for the reactions of $^{112}_{50}$Sn + $^{112}_{50}$Sn and $^{124}_{50}$Sn + $^{124}_{50}$Sn (at 28 MeV/nucleon) were proposed. These observables are also studied by using different beams with projectiles $^{36}_{18}$Ar, $^{40}_{20}$Ca, $^{58}_{26}$Fe and $^{58}_{28}$Ni on $^{58}_{26}$Fe and $^{58}_{28}$Ni targets (at incident energies of 25, 30, 40, 45, 47 and 55 MeV/nucleon) [111–113]. The isotopic distribution of hot primary fragments is found to change strongly over the wide and extended

range of neutron-drip line. Lately, this group also studied the mass dependence of nuclear caloric curve.

1.5 Theoretical Review of multifragmentation

The number of ingenious theoretical theories have been devised to understand the physics behind multifragmentation. But attaining such absolute theory that can be procured from the first principle is not possible at the time and likely computationally impossible. Consequently, to develop such absolute theory, one has to rely on the wise approximations formulated in the theory to explain the physics accurately. The dynamics behind multifragmentation at intermediate energy is examined to explain nuclear equation of state, therefore, one has to concentrate on the relation between empirical data and observables to develop theory through numerical simulations.

Over the recent last years, the number of theoretical methodologies have been developed to examine the physics behind multifragmentation. These methodologies are modelled on various assumptions. To illustrate various models that depict multifragmentation, it is important to note here that physics involved with heavy-ion collisions is exceptionally complex and therefore, requires technical handling to develop such theories. The reaction dynamics associated with the fragmentation differs notably in terms of availability of free phase-space available at low and high incident energies. As discussed earlier, at low incident energies due to less available energy in the compressed system, nearly all the attempted collisions are blocked whereas, at high incident energies the phase-space is primarily free. Interestingly, at intermediate energy it is the equal contribution of both mean-field and binary nucleon-nucleon collisions to the reaction dynamics. These factors are appropriate and in accordance to extract the exact information about the hot and dense state of nuclear matter under extreme conditions of temperature and density. Therefore, various theoretical models can be used to portray multifragmentation through simulations that can further be classified into two types:

- Statistical models,
  and;

- dynamical models.

1.5.1 Statistical models

The statistical models [32–35, 79, 114–120] are based on the idea that the large degrees of freedom are included in the framework. The extensive number of degrees of freedom contributes to form the highly excited hot and dense state of nuclear matter. The statistical theory of multifragmentation predominantly defines the partition probabilities of the decay channels at statistical equilibrium. On the basis of numerous observables observed at intermediate energy, the heavy-ion collisions can be examined utilizing statistical equilibrium. The calculations obtained from statistical equilibrium can be included in the microcanonical ensemble (expressed by number of particles (N), volume (V) and energy (E′)), the canonical ensemble (expressed by number of particles (N), volume (V) and energy (T)) and grand canonical ensemble (expressed by chemical potential (μ), volume (V) and temperature (T)).

In microcanonical framework the entropy determines the number of microstates i.e., weight of the given breakup channel. The primary notion of the model is that the fragmentation takes place simultaneously from the thermalized system. In the literature, various variants of the statistical model are available (microcanonical, canonical and grand canonical ensemble). All these different variants contrast in the method of portraying individual fragments and also in the procedure followed for computation. The available statistical models in the literature are Statistical Multifragmentation Model (SMM) [32, 33, 119, 121] based on microcanonical ensemble, another model based on same approach is Berlin Multifragmentation Model [34, 35, 79, 120], Percolation model [33–35], Lattice gas approach [60], etc. Theoretically, the idea to study nuclear dynamics through statistical models originated from the compound nucleus, the Weisskopf evaporation model (1937) [122] and the theory of multiple particle production. Mekijan [115] was the first one to study multifragmentation using statistical thermodynamics.

Randrup and Koonin [116] considered the macrocanonical ensemble of fragments to determine various observables like multiplicity, momentum distribution and intrinsic spectra of fragments in the incident energy range above 10 MeV/nucleon. Various thermodynamical properties have been determined using statistical models to utilize the correlation between multifragmentation with phase-transition (liquid-gas phase transition) in nuclear matter.

The percolation theory with a few simple assumptions has been used by Bauer *et al* to

perform calculations to study significant features such as mass-yield curves, their peculiar U-shaped behavior and power law-dependance [123]. Similarly, percolation theory used by Li *et al* [46], determined the Z_f - distribution of fragments that emanated from the central symmetric reactions of ^{40}Ar+^{45}Sc and this theory have also been successful to reproduce Z_f - distribution for ^{40}Ar+^{45}Sc reactions in the complete beam energy range between 15 and 115 MeV/nucleon.

Lately, the models based on the canonical ensembles were developed to study the dynamics of multifragmentation i.e., Canonical Thermodynamical model [124]. These models concentrate to study the characteristic behavior of nuclear matter at intermediate energy to study phase-transition for heavy-ion collisions, to understand the caloric curves and probe the tendency of negative heat capacity due to finiteness in nuclear matter. This model can also be utilized for the calculations of observables that are not interlinked with the phase-transition such as to determine the populations of specified isotopes in heavy-ion reactions. The assumption of partial or complete thermal equilibrium in the statistical models is one of the major limitation of these models. Another limitation of statistical models is to study the dynamics of nuclear reactions at the freeze-out time that leads to the origin of dynamical models.

1.5.2 Dynamical models

The theoretical procedure to study the non-equilibrated compressed state of nuclear matter formed at intermediate energy heavy-ion collisions can be divided into three steps:

- Initialization: The target and projectile are prepared in their respective ground states and boosted towards each other with proper center of mass energy.
- Compressional stage: Here, the reaction happens and compressed matter is in the hot and dense state.
- Expansion stage: The nuclear matter expands to sub-nucleonic densities which will ultimately break into different sized fragments and light particles.

The dynamical models ambitiously describe the complete time evolution of the reactions and thus assists in understanding almost all the properties of nuclear reactions. These models follow the dynamics of the reaction from well separated projectile and target to the final stage of the reaction, where nuclear matter exists in the cold fragmented state. The

dynamical models are quite competent in determining the evolution of the non-equilibrium stage of the reaction and therefore, portray a true picture that is close to reality. It is worth mentioning that no dynamical model simulates the fragment production directly but takes into account the evolution of a single nucleon only. Dynamical models are classified into two categories: (i) one-body models and (ii) many-body models.

Various dynamical approaches have been proposed to probe the dynamics of the reaction. Along this direction, methodologies such as Time Dependent Hartree Fock (TDHF) theory or Vlasov equation are developed which are accessible at low incident energy. But for explicit description, theoretical methodologies should treat nucleon-nucleon cross-section and mean-field on equal footing in heavy-ion collisions.

Further, based on the Vlasov-Uehling-Uhlenback (VUU) equations or Boltzmaan-Uehling-Uhlenback (BUU) approach, the one-body models are developed that are suitable for low incident energies where the mean-field dominates and nucleon-nucleon collisions are neglected [125, 126]. The test particle method was used to compute the Vlasov-Uehling-Uhlenback (VUU) equations. Few available one-body approaches are such as Boltzmaan-Uehling-Uhlenback (BUU) [125](or Vlasov-Uehling-Uhlenback (VUU) [126], Landau Vlasov (LV) [127], Boltzmann Nordhiem Vlasov (BNV)[128, 129] and Isospin-dependent Boltzmann-Uehling-Uhlenback (IBUU) models [130, 131]. Therefore, the plausible approach to study heavy-ion reactions at intermediate energy must include mean-field and nucleon-nucleon collisions with equal probability. Some efforts in the past have also been done to extend TDHF theory by incorporating nucleon-nucleon interactions into the framework, responsible for two-body collisions. This approach was dubbed as Extended Time Dependent Hartree Fock theory [40]. However, the numerical complexities in its structure constrained its utility to the low energy domain only. Further, BUU/VUU approach was developed that as a close analogue to TDHF theory. The group of NA (N is the number of test particles and A is the mass number) particles are taken into account to calculate the one-body density distribution function. Alternatively, N-parallel events share interface with each other therefore, event to event correlations cannot be analyzed. Evidently, these models provide convenient probe to one-body phenomenon rather than N-body phenomenon (such as multifragmentation) where correlations between events play a significant role.

In regard to the above requisites, one would need that model which incorporates both nuclear correlations and fluctuations among nucleons. In the methodology of N-body

models, N-parallel events are performed and an average of various physical values is calculated. Since N parallel runs are not interlinked with each other so, event by event correlations can be preserved. Further taking into consideration the above factors, Classical Molecular Dynamics (CMD) model has been developed to deal with the formation of fragments and dynamics associated with it. The applicability of the simple CMD model [173] has been limited due to the absence of quantum features in its structure. The Quantum Molecular Dynamics (QMD) model [11], extension of CMD model has been developed to include quantum features in its structure. Numerous number of variants of N-body dynamical models have been developed such as Antisymmetrized Molecular Dynamics (AMD) model [32, 132–136, 183], Extended Quantum Molecular Dynamics (EQMD) model [137], Fermionic Molecular Dynamics (FMD) model [138], Improved Quantum Molecular Dynamics (ImQMD) model [139, 140], Isospin-dependent Quantum Molecular Dynamics (IQMD) model [141], Constrained Molecular Dynamics (CoMD) model [142, 143], Temperature-dependent Quantum Molecular Dynamics (TQMD) model [144], Binding Quantum Molecular Dynamics (BQMD) model [145], Pauli Quantum Molecular Dynamics (PQMD) model [146], Relativistic Quantum Molecular Dynamics (RQMD) model [147–149], Ultra-relativistic Quantum Molecular Dynamics (UrQMD) model, G - matrix Quantum Molecular Dynamics (GQMD) model [150–153].

The utmost utility of these dynamical models has been in the field of intermediate energy to study heavy-ion reactions. In the next chapter, we will discuss and derive the details of many-body dynamical from one-body dynamical models. The dynamical models also defined as "primary models" generate the phase space of single nucleons. This phase space is further subjected to the "clusterization" algorithms (secondary algorithms) to construct stable fragments.

These secondary algorithms determine physics behind the nuclear reactions through the adopted clusterization algorithms. The simplest method to identify fragments is to spatially constrain the distance between the centroids of two nucleons and this method is termed as Minimum Spanning Tree (MST) method [11]. As MST approach takes only coordinate space into account, therefore, in concern to improve the stability of fragments various variants of MST method has been developed. These variants are such as Minimum Spanning Tree with momentum cut (MSTP) [154, 155], Minimum Spanning Tree with Binding energy cut (MSTB) [156], Minimum Spanning Tree with temperature binding energy (MSTBT) cut [11, 154–157]. In aim to reproduce more reliable results energy

minimization method have also been introduced [158, 159]. The energy based algorithm guarantee greater stability of fragments. In the present thesis, we will concentrate on the role of various clusterization algorithms to study phase-transition in nuclear matter and associate the significance of emission of light particles to study entropy production.

1.6 Plan of work

In chapter 2, we shall describe various dynamical models developed in literature to study dynamics of heavy-ion reactions at intermediate energies. We shall review transport models such as Quantum Molecular Dynamics (QMD) model and its isospin variant namely Isospin-dependent Quantum molecular Dynamics (IQMD) model, which will be used as a principle theoretical approach in our study.

In chapter 3, we shall discuss various clusterization algorithms such as Minimum Spanning Tree (MST) method, Minimum Spanning Tree method with Momentum (MSTP or MSTM) cut, Minimum Spanning Tree method with Binding energy (MSTB) cut and Minimum Spanning Tree method with Thermal binding energy (MSTBT) cut. These clusterization algorithms will be utilized to identify fragments. The aim is to search for the critical point to study onset of multifragmentation in nuclear matter. In this regard the charge yield of intermediate mass fragments will be fitted using power-law and exponential law to extract the critical parameters such as 'τ' and 'λ'. The minimum in the values of these critical parameters when studied as a function of incident energy is often linked with onset of multifragmentation or critical energy point for liquid-gas phase transition. Since studying these critical parameters is not the sufficient condition to study onset of multifragmentation, we shall also analyze other parameters based on the charge moments such as $<S_2>$, $<\gamma_2>$ of fragments and charge of the second largest fragment (Z_{max2}). These parameters will be analyzed to find the exact energy of onset of multifragmentation or critical energy point and its sensitivity towards clusterization algorithms.

In chapter 4, we shall discuss fine details of energy based clusterization algorithm i.e., Simulated Annealing Clusterization Algorithm (SACA) to overcome the discrepancies of clusterization algorithms discussed in previous chapter. This algorithm is based on metropolis procedure. Then, we shall confront our calculations obtained by QMD model + SACA with experimental obsevations. The study will be done for both lightly and heavily charged systems. We shall discuss all the parameters discussed in chapter 3 to study the onset of multifragmentation.

In chapter 5, we study the onset of vaporization for ^{16}O+^{80}Br reactions. We shall compute average charge of the fragments with and without largest fragment. We shall study the role of varying clusterization range on the fragmentation pattern and its effect on the point of onset of vaporization. Our study shall also span over the wide range of clusteri-

zation algorithms i.e., Minimum Spanning Tree (MST) method, Minimum Spanning Tree method with momentum cut (MSTM or MSTP) and Simulated Annealing Clusterization Algorithm (SACA). We will study this phenomenon using QMD model as phase space generator coupled with various clusterization algorithms. We shall also compare our calculations with available experimental data.

Further, we shall present a complete systematic study of mass asymmetric reactions available throughout the periodic table. We will explore the effect of asymmetry and incident energy on the composite yield of light mass particles and entropy production by extracting slopes using power-law. The work shall be done in the framework of Isospin-dependent Quantum Molecular Dynamics (IQMD) model. The study will be done in the incident range of 400 to 1000 MeV/nucleon.

Finally, we will summarize our results with an outlook in Chapter 6.

Chapter 2

Insight of various theoretical models

The growth in theoretical nuclear physics witnessed the development of diverse range of theoretical models that can consistently explain many aspects of reaction dynamics. At the same time, with the modernization of the experimental facilities worldwide, many new challenges are known to the field. To understand the heavy-ions dynamics involved at intermediate energies, one needs to have explicit and precise knowledge about the mean-field and binary nn-collisions to describe the real and imaginary parts of the G-matrix, respectively. Among various theories, the Time Dependant Hartree Fock (TDHF) theory [160, 161], was the first approach developed on the basis of conventional mean field hypothesis. It was though successful to crack down many hidden questions in nuclear physics, yet was found unsuitable for describing reaction dynamics at intermediate energies [40]. Later on, this theory was extended by including binary nn-collisions. Even then, it was limited to low incident energies only [162].

In contrast to TDHF theory, the Intra-Nuclear Cascade (INC) model developed by Cugnon [163] and its different variants neglected the role of mean-field and took into account the binary nn-collisions only [164–166]. This model did not incorporate long range correlations. It considered the rapidly changing correlations only. In the absence of mean-field, the nucleons are bound to follow straight line trajectories between the two consecutive collisions. Since the cascade is a very rapid process (10^{-22} sec) therefore, it is suitable for high energy heavy-ion collisions only where binary nucleon-nucleon collisions are very frequent [167]. In the framework of INC model, nucleons in a nucleus are considered as a bundle of point particles distributed within the sphere without Fermi-momentum. The Monte-Carlo sampling is used to assign the initial positions to all the nucleons in a given sphere. It is worth mentioning that the cascade model is based on

the assumption that incoming particles interact with each nucleon of the target. The INC model is successful in explaining various experimental observables measured at high incident energies [164]. Unfortunately, this model was found to fail in describing various phenomena at intermediate incident energies (such as multifragmentation, flow, etc.) where the outcome depends strongly on the initial Fermi-momentum and also on the intrinsic pressure built during the reaction due to the presence of mean-field. Due to these limitations, the cascade model is useful only at high incident energies where the role of mean-field is nearly negligible. In addition, the inconsistency of Cascade model to reproduce estimated pion yields led to the need of designing a new model that ought to improve the assumptions taken in the original Cascade model. The strong efforts were made by Cugnon *et al.* to modify the original INC model by incorporating compression and decompression effects (not considered in the original version of INC model) which are essential to study the phenomena like multifragmentation, flow, etc. [163]. Interestingly, this model also failed to explain the dynamics owing to the absence of mean-field in its structure.

Altogether different approach namely Boltzmann-Uehling-Uhlenbeck (BUU) (or Vlasov-Uehling-Uhlenbeck (VUU)) model was proposed in the literature [125, 126]. This approach studies the evolution of one-body Wigner phase space and incorporate both mean-field and binary nn-collisions in its framework. This type of model is the combination of single particle dynamics (mean-field) and two-body scattering but neglects the many-body correlations in its structure. The VUU/BUU model is quite accomplished in studying the role of single particle observables on nuclear dynamics. In one-body models, large numbers of events are run in parallel to obtain the smooth density functions in the phase space. These models can barely explain the physics behind the phenomena like fragment formation and multifragmentation which needs multiparticle dynamics and correlations. On the other hand, single particle observables such as particle spectra, flow angles, and pion yields were well explained in the framework of VUU model. It should be kept into mind that the one-body models have been inconsistent in describing the necessary physics behind the phenomenon involving multi-body correlations [12, 32]. Therefore, the many-body models that study N-body correlations have been able to subdue all the limitations of one-body models. The many-body models can preserve the multi-particle correlations between nucleons and can explain successfully various phenomena associated with these correlations [11, 12, 32, 141, 168–172].

2.1 N-body molecular dynamical models

The majority of studies done in the past over different energy domains using VUU/BUU models are based on the test-particle concept. In contrast, the many particle models simulate the collisions of real nucleons on event-by-event basis. The famous many-body transport model namely Quantum Molecular Dynamics (QMD) model was developed by Aichelin and Stocker in late eighties [11]. The structure of this model is based on the features of Classical Molecular Dynamics (CMD) model (first N-body model) [173]. In comparison to the one-body dynamical models, this model is based on decreasing the total number of test particles so that each particle represents one nucleon only. Due to the reduced count of test particles, it became feasible to study the N-body correlations of the colliding system. The QMD model obtains most of the features of CMD model but differs from the CMD model with respect to the some of the following quantum features:

- the presence of both collision and potential terms in the dynamical evolution,
- the inclusion of Pauli Principle to respect the Fermionic features of nucleons, and;
- the stochastic scattering of nucleons.

The QMD approach studies the reaction dynamics based on the event-by-event analysis, therefore, preserves the correlations among nucleons. In this approach, each event is simulated individually irrespective of the other events. Unlike BUU/VUU approach, no averaging is done over various events to preserve the initial correlations among the nucleons. The paradigm of the transport model follows three important steps:

- Initialization,
- Propagation,

  and
- Scattering.

In the following sub-sections, we shall explore each step in detail.

2.1.1 Initialization

In the beginning, each nucleon from the projectile and target is assigned coordinate and momentum. This is done by using the Monte-Carlo method where coordinates of each nucleon are assured within sphere of radius R= 1.14 $A^{1/3}$. With the help of Monte-Carlo method, the random numbers are drawn and coordinates of those nucleons are rejected where centroids are closer than certain distance i.e., r_{min}=1.5 fm. The major aim behind this restriction is to procure those nuclei that guarantee proper binding energy and root mean square radii and are stable enough during entire span of the reaction. The local Fermi-momentum is determined using Fermi-gas approximation and it reads as:

$$\mathbf{P}_F(\mathbf{r}_i) = \sqrt{-2mU(\mathbf{r}_i)}, \tag{2.1}$$

where $\mathbf{P}_F(\mathbf{r}_i)$ is the local momentum. The value of the momentum lies between zero and $\mathbf{P}_F$. All those configurations are drawn which fulfill the following criteria:

$$(\mathbf{r}_i - \mathbf{r}_j)^2(\mathbf{p}_i - \mathbf{p}_j)^2 \geq d_{min}. \tag{2.2}$$

Here d_{min} is the allowed distance between centroids of two nucleons. In the QMD model, quantum features are included in the structure through describing each nucleon by the Gaussian wavepacket. So the initial wavefunction in coordinate and momentum space given in the coherent state of the form reads as:

$$\psi_i(\mathbf{r}, \mathbf{r}_i(t), \mathbf{p}_i(t)) = \frac{1}{(2\pi L)^{3/4}} e^{\left[\frac{i}{\hbar}\mathbf{p}_i(t)\cdot\mathbf{r} - \frac{(\mathbf{r}-\mathbf{r}_i(t))^2}{4L}\right]}, \tag{2.3}$$

and

$$g_i(\mathbf{p}, \mathbf{r}_i(t), \mathbf{p}_i(t)) = \frac{2L}{(\pi)^{3/4}} e^{-\left[i\mathbf{p}\cdot\mathbf{r_i(t)} + (\mathbf{p}-\mathbf{p_i(t)})^2 L\right]}, \tag{2.4}$$

respectively. Here 'L' is the Gaussian width of the wavepacket [11, 141]. The total A-body wavefunction for all the nucleons is approximated as a direct product of A-coherent states. The total wavefunction can be written as:

$$\Phi = \prod\nolimits_i \psi_i(\mathbf{r}, \mathbf{r}_i, \mathbf{p}_i, t). \tag{2.5}$$

The QMD model neglects the antisymmetrization of the wavefunction since it does not incorporate Slater determinant in its structure. It is of great significance to mention here that the phase space evolution using the nn-interaction has been found to be consistent

with that of TDHF and Vlasov theories. The TDHF theory begins with the Slater determinant, Vlasov theory from the randomly drawn points inside a sphere of radius R = 1.12 $A^{1/3}$ and the random momenta which is calculated between zero and Fermi-momentum, whereas, the QMD model begins with biased choice of the positions and momenta of nucleons. The striking feature is that the time evolution of the system is independent of the initialization in any of these theories. Evidently, this feature plays a prime role in the time evolution of the system, if it fulfills the basic prerequisites like approximate constant density over the coordinate space as well as proper binding energy [11].

Now, to study the time evolution of nucleons in QMD model, the N-body Schrödinger equation can be utilized. The Schrödinger equation used in the framework is non-relativistic and keeps the momentum and position coordinates on unequal footing. Although, we are able to solve the equation, still the outcome may not be clear. A somewhat different approach helps to simplify this difficulty; the Wigner distribution function. This function is close interlink between the quantum mechanical and classical wavefunctions. The Wigner transformation operator (M) is given as :

$$\begin{aligned} M^W(\mathbf{P},\mathbf{R}) &= \int \frac{d^3s}{2\pi^3} e^{-i\mathbf{P}\cdot\mathbf{s}} < \mathbf{R}-\mathbf{s}/2|M|\mathbf{R}+\mathbf{s}/2 > \\ &= \int \frac{d^3q}{2\pi^3} e^{-i\mathbf{q}\cdot\mathbf{R}} < \mathbf{P}-\mathbf{q}/2|M|\mathbf{P}+\mathbf{q}/2 >, \end{aligned} \tag{2.6}$$

here, '**s**' and '**q**' represent the small change in the coordinate and momentum spaces, respectively. Here operator 'M' corresponds to the density operator and its transform is termed as Wigner density. Thus, the Wigner density of the i^{th} particle in the coordinate and momentum space can be deduced as:

$$\begin{aligned} f_i(\mathbf{r},\mathbf{p},\mathbf{r}_i(t),\mathbf{p}_i(t)) &= \frac{1}{(2\pi\hbar)^3}\int e^{-\frac{i}{\hbar}\mathbf{p}\cdot\mathbf{r}_{12}}\psi_i(\mathbf{r}+\frac{\mathbf{r}_{12}}{2},t)\psi_i^*(\mathbf{r}-\frac{\mathbf{r}_{12}}{2},t)d^3r_{12}, \\ &= \frac{1}{(2\pi\hbar)^3}\frac{1}{(2\pi L)^{3/2}}\int e^{-\frac{i}{\hbar}\mathbf{p}\cdot\mathbf{r}_{12}} e^{\frac{i}{\hbar}\mathbf{p}_i(t)\cdot(\mathbf{r}+\frac{\mathbf{r}_{12}}{2})-\frac{[\mathbf{r}+\frac{\mathbf{r}_{12}}{2}-\mathbf{r}_i(t)]^2}{4L}} \\ &\qquad \times e^{-\frac{i}{\hbar}\mathbf{p}_i(t)\cdot(\mathbf{r}-\frac{\mathbf{r}_{12}}{2})-\frac{[\mathbf{r}-\frac{\mathbf{r}_{12}}{2}-\mathbf{r}_i(t)]^2}{4L}} d^3r_{12}, \\ &= \frac{1}{(2\pi\hbar)^3}\frac{1}{(2\pi L)^{3/2}}\int e^{-\frac{i}{\hbar}\mathbf{p}\cdot\mathbf{r}_{12}} e^{\frac{i}{\hbar}\mathbf{p}_i(t)\cdot\mathbf{r}_{12}-(\mathbf{r}-\mathbf{r}_i(t))^2/2L-\mathbf{r}_{12}^2/8L} d^3r_{12}, \\ &= \frac{1}{(2\pi\hbar)^3}\frac{1}{(2\pi L)^{3/2}}\int e^{-\frac{i}{\hbar}(\mathbf{p}-\mathbf{p}_i(t))^2\cdot\mathbf{r}_{12}} e^{-(\mathbf{r}-\mathbf{r}_i(t))^2/2L-\mathbf{r}_{12}^2/8L} d^3r_{12}, \\ &= \frac{1}{(2\pi\hbar)^3}\frac{1}{(2\pi L)^{3/2}} e^{-(\mathbf{r}-\mathbf{r}_i(t))^2/2L}\int e^{-\frac{i}{\hbar}(\mathbf{p}-\mathbf{p}_i(t))^2\cdot\mathbf{r}_{12}-\mathbf{r}_{12}^2/8L} d^3r_{12}, \end{aligned}$$

$$
\begin{aligned}
&= \frac{1}{(2\pi\hbar)^3}\frac{1}{(2\pi L)^{3/2}} e^{-(\mathbf{r}-\mathbf{r}_i(t))^2/2L} \\
&\quad \times \int e^{-\left[\frac{i}{\hbar}(\mathbf{p}-\mathbf{p}_i(t))^2\cdot\mathbf{r}_{12}+\mathbf{r}_{12}^2/8L+i^2(\mathbf{p}-\mathbf{p}_i(t))^2 2L/\hbar^2-i^2(\mathbf{p}-\mathbf{p}_i(t))^2 2L/\hbar^2\right]} d^3r_{12}, \\
&= \frac{1}{(2\pi\hbar)^3}\frac{1}{(2\pi L)^{3/2}} e^{-(\mathbf{r}-\mathbf{r}_i(t))^2/2L} e^{-(\mathbf{p}-\mathbf{p}_i(t))^2 2L/\hbar^2} \\
&\quad \times \int e^{-\left[\frac{i}{\hbar}(\mathbf{p}-\mathbf{p}_i(t))\sqrt{2L}+\mathbf{r}_{12}/2\sqrt{2L}\right]^2} d^3r_{12}, \\
&= \frac{1}{(2\pi\hbar)^3}\frac{1}{(2\pi L)^{3/2}} e^{-(\mathbf{r}-\mathbf{r}_i(t))^2/2L} e^{-(\mathbf{p}-\mathbf{p}_i(t))^2 2L/\hbar^2} \times \left(2\sqrt{2\pi L}\right)^3, \\
&= \frac{1}{(\pi\hbar)^3} e^{-(\mathbf{r}-\mathbf{r}_i(t))^2/2L} e^{-(\mathbf{p}-\mathbf{p}_i(t))^2 2L/\hbar^2}, \qquad (2.7)
\end{aligned}
$$

where $\mathbf{r}_i(t)$ and $\mathbf{p}_i(t)$ represent the centroids of Gaussian wave packet in the phase space. Although, the Wigner density acts like a classical particle it can also have negative values. Further, the Wigner transformation follows the uncertainty principle $\triangle x \cdot \triangle p = \hbar/2$ [11]. The Wigner transformation in coordinate and momentum space of the coherent states is defined by the Gaussian wavefunction. To achieve the desirable density function, one can subject the Wigner density distribution in the phase space for each nucleon in the coordinate and momentum space. Therefore, the density of the i^{th} particle in the coordinate space is defined as:

$$
\begin{aligned}
\rho_i(\mathbf{r}, \mathbf{r}_i(t), \mathbf{p}_i(t)) &= \int f_i(\mathbf{r}, \mathbf{p}, \mathbf{r}_i(t), \mathbf{p}_i(t)) d^3p, \\
&= \int \frac{1}{(\pi\hbar)^3} e^{-[\mathbf{r}-\mathbf{r}_i(t)]^2/2L} e^{-[\mathbf{p}-\mathbf{p}_i(t)]^2 2L/\hbar^2} d^3p, \\
&= \frac{1}{(\pi\hbar)^3} e^{-[\mathbf{r}-\mathbf{r}_i(t)]^2/2L} \int e^{-[\mathbf{p}-\mathbf{p}_i(t)]^2 2L/\hbar^2} d^3p, \\
&= \frac{1}{(\pi\hbar)^3} e^{-[\mathbf{r}-\mathbf{r}_i(t)]^2/2L} \left(\sqrt{\frac{\pi\hbar^2}{2L}}\right)^3 \\
&= \frac{1}{(2\pi L)^{3/2}} e^{-[\mathbf{r}-\mathbf{r}_i(t)]^2/2L} \\
&= |\psi_i(\mathbf{r}, \mathbf{r}_i, \mathbf{p}_i, t)|^2. \qquad (2.8)
\end{aligned}
$$

In the same way, densities in the momentum space reads as:

$$
\begin{aligned}
\rho_i(\mathbf{p}, \mathbf{r}_i(t), \mathbf{p}_i(t)) &= \int f_i(\mathbf{r}, \mathbf{p}, \mathbf{r}_i(t), \mathbf{p}_i(t)) d^3r \\
&= \left(\frac{2L}{\pi}\right)^{3/2} e^{-(\mathbf{p}-\mathbf{p}_i)^2 2L} \\
&= |g_i(\mathbf{p}, \mathbf{r}_i(t), \mathbf{p}_i(t))|^2. \qquad (2.9)
\end{aligned}
$$

Further to pursue the simulation of heavy-ion collision, we need to built the projectile and target. This can be done by the following steps:

The centroid of each Gaussian wave packet is uniformly distributed in a sphere (of radius R = 1.14 $A^{1/3}$, where A implies to the mass of the nucleus) in the polar coordinates by selecting:

$$\begin{aligned} \mathbf{r} &= R\ c_1^{1/3}, \\ cos\ \boldsymbol{\theta} &= 1 - 2\ c_2, \\ \boldsymbol{\phi} &= 2\pi\ c_3, \end{aligned} \tag{2.10}$$

where c_1, c_2 and c_3 are the random numbers. A minimum distance of 1.5 fm between two centroids of Gaussians is imposed to get smooth nuclear density. Similarly, the centroid of each Gaussian wave packet in the momentum space is uniformly distributed in polar coordinates by:

$$\begin{aligned} \mathbf{p} &= \mathbf{P}_F(\mathbf{r}_i)\ c_4^{1/3}, \\ cos\ \boldsymbol{\theta} &= 1 - 2\ c_5, \\ \boldsymbol{\phi} &= 2\pi\ c_6, \end{aligned} \tag{2.11}$$

where c_4, c_5 and c_6 again are random numbers. In the above equation, the Fermi-momentum can be computed from the eq. (2.1).

The eigen states of the Hamiltonian have to fulfill the uncertainty relation. The phase space of the ground state of a system is completely filled up to the highest level in the coordinate and momentum space without any vacancy. This feature of the ground state is used to initialize target and projectile. Strikingly, only 1 out of 50,000 initializations qualifies under present criteria. This model ensures proper binding energy and root mean square radii of both target and projectile in the coordinate and momentum space. The issue about the stability of nuclei has been properly handled by the Frankfurt group [174]. They have shown an enhancement in the stability time for the propagation of nuclei with the inclusion of Pauli principle in the mean field. In the same way, Nantes group also tested the stability of nuclei in terms of the root mean square (r.m.s) radius as well as in terms of binding energy [11]. Most of the procured nuclei were stable for the time of couple of hundred fm/c which is long enough duration for the present purpose.

2.1.2 Propagation

Once the stable projectile and target are prepared, they are boosted towards each other with the proper center-of-mass energy. The equations of motion for many-body system are determined by using the generalized Variational principle. We state action as:

$$S = \int_{t_1}^{t_2} \mathcal{L}[\Phi, \Phi^*]dt, \tag{2.12}$$

where $\mathcal{L}$ represents the Lagrange functional of the form:

$$\mathcal{L} = \langle\Phi|i\hbar\frac{d}{dt} - H|\Phi\rangle. \tag{2.13}$$

Under the allowed variation of the wave function, the action is kept constant to obtain the time evolution using the relation

$$\delta S = \delta \int_{t_1}^{t_2} \mathcal{L}[\Phi, \Phi^*]dt = 0. \tag{2.14}$$

This gives the Euler-Lagrange equation for each parameter 'λ' which reads as:

$$\frac{d}{dt}\frac{\partial\mathcal{L}}{\partial\dot{\lambda}} - \frac{\partial\mathcal{L}}{\partial\lambda} = 0. \tag{2.15}$$

Now if the $\psi_i(\mathbf{r}, \mathbf{r}_i, \mathbf{p}_i, t)$ under the limitation includes the true solution of the Schrödinger equation, then the variation in the above action will initiate the accurate solution of Schrödinger equation. For any coherent state and Hamiltonian of the form:

$$\langle H\rangle = \sum_i \langle T_i\rangle + \frac{1}{2}\sum_{ij}\langle V_{ij}\rangle, \tag{2.16}$$

where T_i is the kinetic energy and V_{ij} is potential energy, the Lagrangian can easily be obtained by:

$$\mathcal{L} = \sum_i \left[-\dot{\mathbf{r}}_i\mathbf{p}_i - T_i - \frac{1}{2}\sum_{j\neq i} < V_{ij} >\right] - \frac{3}{2Lm}. \tag{2.17}$$

Using Euler Lagrange equation the time evolution of $\mathbf{r}_i$ and $\mathbf{p}_i$ can be determined:

$$\frac{d}{dt}\frac{\partial\mathcal{L}}{\partial\dot{\mathbf{p}}_i} - \frac{\partial\mathcal{L}}{\partial\mathbf{p}_i} \rightarrow \dot{\mathbf{r}}_i = \frac{\mathbf{p}_i}{m} + \nabla_{\mathbf{p}_i}\sum_j < V_{ij} >,$$

$$\therefore \dot{\mathbf{r}}_i = \nabla_{\mathbf{p}_i} < H >, \tag{2.18}$$

$$\frac{d}{dt}\frac{\partial\mathcal{L}}{\partial\dot{\mathbf{r}}_i} - \frac{\partial\mathcal{L}}{\partial\mathbf{r}_i} \rightarrow \dot{\mathbf{p}}_i = -\nabla_{\mathbf{r}_i}\sum_{j\neq i} < V_{ij} >,$$

$$\therefore \dot{\mathbf{p}}_i = -\nabla_{\mathbf{r}_i} < H >, \tag{2.19}$$

where $\mathbf{r}_i = \mathbf{r}_i + \frac{\mathbf{p}_i}{m}t$ and $\langle V_{ij}\rangle = \int d^3\mathbf{r}_1 d^3\mathbf{r}_2 \langle \psi_i^* \psi_j^* | V(\mathbf{r}_1, \mathbf{r}_2) | \psi_i \psi_j \rangle$. These equations, solved using variational principle, make it feasible to solve $6 \times \mathrm{A}_T$ ($\mathrm{A}_T = \mathrm{A}_{Proj}+\mathrm{A}_{Tar}$) [where A_{Proj} and A_{Tar} corresponds to mass of the projectile and target, respectively] linear differential equations, which are much more convenient to solve in comparison to the N-body second order Schrödinger equation. Subsequently, the framework of equations of motion is close analogue to the classical Hamilton's equations and it can be given as:

$$\dot{\mathbf{r}}_i = \frac{\partial \langle H \rangle}{\partial \mathbf{p}_i}; \qquad \dot{\mathbf{p}}_i = -\frac{\partial \langle H \rangle}{\partial \mathbf{r}_i}. \tag{2.20}$$

The numerical solution for these equations can be obtained in a same manner as done for the Classical Molecular Dynamics calculations, therefore, the average of the total Hamiltonian can be expressed as:

$$\begin{aligned} \langle H \rangle &= \langle T \rangle + \langle V \rangle \\ &= \sum_i \frac{\mathbf{p}_i^2}{2m_i} + V^{Sky} + V^{Yuk} + V^{Coul}. \end{aligned} \tag{2.21}$$

The terms V^{Sky}, V^{Yuk} and V^{Coul} are the local (two and three-body) Skyrme, Yukawa and Coulomb potentials, respectively. The local Skyrme potential is given by:

$$V^{Sky} = \frac{1}{2!}\sum_{j;i\neq j} V_{ij}^{(2)} + \frac{1}{3!}\sum_{j,k;i\neq j\neq k} V_{ijk}^{(3)}. \tag{2.22}$$

Here, $\mathrm{V}_{ij}^{(2)}$ and $\mathrm{V}_{ijk}^{(3)}$ represent the two- and three-body terms of the local Skyrme potential, respectively. The two-body interactions $\mathrm{V}_{ij}^{(2)}$ are computed by folding the two-body potential with the densities of both the nucleons. This is solved as:

$$\begin{aligned} \sum_{j;i\neq j} V_{ij}^{(2)} &= \sum_{j;i\neq j} \int f_i(\mathbf{r}_i, \mathbf{p}_i, t) f_j(\mathbf{r}_j, \mathbf{p}_j, t) V(\mathbf{r}_i, \mathbf{r}_j) d^3r_i d^3r_j d^3p_i d^3p_j, \\ &= \sum_{j;i\neq j} \int f_i(\mathbf{r}_i, \mathbf{p}_i, t) f_j(\mathbf{r}_j, \mathbf{p}_j, t) t_1 \delta(\mathbf{r}_i - \mathbf{r}_j) d^3r_i d^3r_j d^3p_i d^3p_j, \\ &= \sum_{j;i\neq j} t_1 \int f_i(\mathbf{r}_i, \mathbf{p}_i, t) f_j(\mathbf{r}_j, \mathbf{p}_j, t) d^3r d^3p_i d^3p_j, \\ &= \sum_{j;i\neq j} t_1 \int \frac{1}{(\pi\hbar)^3} e^{-(\mathbf{r}-\mathbf{r}_i(t))^2/2L} e^{-(\mathbf{p}-\mathbf{p}_i(t))^2 2L/\hbar^2} \end{aligned}$$

$$
\begin{aligned}
&\times \frac{1}{(\pi\hbar)^3} e^{-(\mathbf{r}-\mathbf{r}_j(t))^2/2L} e^{-(\mathbf{p}-\mathbf{p}_j(t))^2 2L/\hbar^2} d^3r d^3p_i d^3p_j, \\
= \;& \frac{1}{(\pi\hbar)^6} \left(\sqrt{\frac{\pi\hbar^2}{2L}}\right)^3 \left(\sqrt{\frac{\pi\hbar^2}{2L}}\right)^3 \sum_{j;i\neq j} t_1 \int e^{-(\mathbf{r}-\mathbf{r}_i(t))^2/2L} e^{-(\mathbf{r}-\mathbf{r}_j(t))^2/2L} d^3r, \\
= \;& \frac{1}{(2\pi L)^3} \sum_{j;i\neq j} t_1 \int e^{-(\mathbf{r}-\mathbf{r}_i(t))^2/2L - (\mathbf{r}-\mathbf{r}_j(t))^2/2L} d^3r, \\
= \;& \frac{1}{(2\pi L)^3} \sum_{j;i\neq j} t_1 \int e^{-\left[\frac{\mathbf{r}^2}{L} - \frac{\mathbf{r}}{L}(\mathbf{r}_i+\mathbf{r}_j)\right] - \left(\frac{\mathbf{r}_i^2+\mathbf{r}_j^2}{2L}\right)} d^3r, \\
= \;& \frac{1}{(2\pi L)^3} \sum_{j;i\neq j} t_1 \int e^{-\left[\left\{\frac{\mathbf{r}^2}{L} - \frac{\mathbf{r}}{L}(\mathbf{r}_i+\mathbf{r}_j) + \left(\frac{\mathbf{r}_i+\mathbf{r}_j}{2\sqrt{L}}\right)^2\right\} - \left(\frac{\mathbf{r}_i+\mathbf{r}_j}{2\sqrt{L}}\right)^2\right]} e^{-\left(\frac{\mathbf{r}_i^2+\mathbf{r}_j^2}{2L}\right)} d^3r, \\
= \;& \frac{1}{(2\pi L)^3} \sum_{j;i\neq j} t_1 \int e^{-\left[\left\{\frac{\mathbf{r}}{\sqrt{L}} - \left(\frac{\mathbf{r}_i+\mathbf{r}_j}{2\sqrt{L}}\right)\right\}^2 - \left(\frac{\mathbf{r}_i+\mathbf{r}_j}{2\sqrt{L}}\right)^2\right]} e^{-\left(\frac{\mathbf{r}_i^2+\mathbf{r}_j^2}{2L}\right)} d^3r, \\
= \;& \frac{1}{(2\pi L)^3} \sum_{j;i\neq j} t_1 \int e^{-\left[\left\{\frac{\mathbf{r}}{\sqrt{L}} - \left(\frac{\mathbf{r}_i+\mathbf{r}_j}{2\sqrt{L}}\right)\right\}^2 - \left(\frac{\mathbf{r}_i^2}{4L} + \frac{\mathbf{r}_j^2}{4L} + \frac{\mathbf{r}_i\mathbf{r}_j}{2L}\right) + \left(\frac{\mathbf{r}_i^2}{2L} + \frac{\mathbf{r}_j^2}{2L}\right)\right]} d^3r, \\
= \;& \frac{1}{(2\pi L)^3} \sum_{j;i\neq j} t_1 \int e^{-\left[\left\{\frac{\mathbf{r}}{\sqrt{L}} - \left(\frac{\mathbf{r}_i+\mathbf{r}_j}{2\sqrt{L}}\right)\right\}^2 + \left(\frac{\mathbf{r}_i^2}{4L} + \frac{\mathbf{r}_j^2}{4L} - \frac{\mathbf{r}_i\mathbf{r}_j}{2L}\right)\right]} d^3r, \\
= \;& \frac{1}{(2\pi L)^3} \sum_{j;i\neq j} t_1 \int e^{-\left[\left\{\frac{\mathbf{r}}{\sqrt{L}} - \left(\frac{\mathbf{r}_i+\mathbf{r}_j}{2\sqrt{L}}\right)\right\}^2 + \left(\frac{\mathbf{r}_i}{2\sqrt{L}} - \frac{\mathbf{r}_j}{2\sqrt{L}}\right)^2\right]} d^3r, \\
= \;& \frac{1}{(2\pi L)^3} \sum_{j;i\neq j} t_1 e^{-(\mathbf{r}_i-\mathbf{r}_j)^2/4L} \int e^{-\left\{\frac{\mathbf{r}}{\sqrt{L}} - \left(\frac{\mathbf{r}_i+\mathbf{r}_j}{2\sqrt{L}}\right)\right\}^2} d^3r, \\
= \;& \sum_{j;i\neq j} t_1 e^{-(\mathbf{r}_i-\mathbf{r}_j)^2/4L} \;\; \frac{1}{(2\pi L)^3} \;\; (\sqrt{\pi L})^3,
\end{aligned}
$$

$$
\begin{aligned}
&= \sum_j t_1 \frac{1}{(4\pi L)^{3/2}} e^{-(\mathbf{r}_i-\mathbf{r}_j)^2/4L} \\
&= t_1 \sum_{j;i\neq j} \rho_{ij}, \qquad (2.23)
\end{aligned}
$$

where,

$$
\rho_{ij} = \int d^3r \rho_i(\mathbf{r}) \rho_j(\mathbf{r}) = \frac{1}{(4\pi L)^{3/2}} e^{-(\mathbf{r}_i-\mathbf{r}_j)^2/4L}. \qquad (2.24)
$$

The three-body part of the Skyrme interaction is calculated as

$$
\sum_{j,k;i\neq j\neq k} V_{ijk}^{(3)} \;\; = \;\; \sum_{j,k;i\neq j\neq k} \int f_i(\mathbf{r}_i, \mathbf{p}_i, t) f_j(\mathbf{r}_j, \mathbf{p}_j, t) f_k(\mathbf{r}_k, \mathbf{p}_k, t) V(\mathbf{r}_i, \mathbf{r}_j, \mathbf{r}_k)
$$

$$
\begin{aligned}
&\times d^3r_i d^3r_j d^3r_k d^3p_i d^3p_j d^3p_k, \\
= &\sum_{j,k;i\neq j\neq k} \int f_i(\mathbf{r}_i,\mathbf{p}_i,t) f_j(\mathbf{r}_j,\mathbf{p}_j,t) f_k(\mathbf{r}_k,\mathbf{p}_k,t) t_2 \\
&\times \delta(\mathbf{r}_i-\mathbf{r_j})\delta(\mathbf{r}_i-\mathbf{r}_k) d^3r_i d^3r_j d^3r_k d^3p_i d^3p_j d^3p_k, \\
= &\frac{t_2}{(2\pi L)^3\ 3^{3/2}} \sum_{j,k;i\neq j\neq k} e^{-\left[(\mathbf{r}_i-\mathbf{r}_j)^2+(\mathbf{r}_i-\mathbf{r}_k)^2+(\mathbf{r}_k-\mathbf{r}_j)^2\right]/6L}, \\
= &\frac{t_2}{(2\pi L)^3\ 3^{3/2}} \sum_{j,k;i\neq j\neq k} e^{\{-\left[(\mathbf{r}_i-\mathbf{r}_j)^2+(\mathbf{r}_i-\mathbf{r}_k)^2\right]/6L\}\times\frac{3}{2}}, \\
= &\frac{t_2(4\pi L)^{3/2\times 2}}{(2\pi L)^3\ 3^{3/2}} \left[\sum_{j\neq i} \frac{1}{(4\pi L)^{3/2}} e^{-(\mathbf{r}_i-\mathbf{r}_j)^2/4L}\right]^2, \\
= &\frac{t_2\ 2^3}{3^{3/2}} \left[\sum_{j\neq i} \rho_{ij}\right]^2. \qquad (2.25)
\end{aligned}
$$

This is further supplemented by the Coulomb interaction V^{Coul} term which is given by:

$$V^{Coul} = \sum_{j;i\neq j} \frac{Z_{eff}^2 e^2}{|\mathbf{r}_i-\mathbf{r}_j|}. \qquad (2.26)$$

The finite two-body range Yukawa interaction V^{Yuk} is given by:

$$V^{Yuk} = \sum_{j;i\neq j} t_3 \frac{e^{-|\mathbf{r}_i-\mathbf{r}_j|/\omega}}{|\mathbf{r}_i-\mathbf{r}_j|/\omega}. \qquad (2.27)$$

The part of Yukawa term [with t_3 = -6.66 MeV and ω (range of Yukawa potential = 1.5 fm)] in the structure is incorporated to improve the surface properties of the nuclei. Since the interaction density coincides precisely with the single particle density, this assists us to correlate the required parameters to the nuclear matter properties. Note that the two-body part of the Skyrme interaction potential and Yukawa interaction are linearly proportional to $(\frac{\rho}{\rho_0})$ whereas, three-body part of the Skyrme potential is proportional to $(\frac{\rho}{\rho_0})^2$.

$$V^{Sky} = \frac{\acute{\alpha}}{2}\left(\frac{\rho}{\rho_0}\right) + \frac{\acute{\beta}}{\acute{\gamma}+1}\left(\frac{\rho}{\rho_0}\right)^2. \qquad (2.28)$$

The $\acute{\alpha}$, $\acute{\beta}$ and $\acute{\gamma}$ are the free parameters in the above given equation. The general properties like average binding energy (-15.75 MeV) and total energy that possess minimum at ρ_0 are used to compute the values of $\acute{\alpha}$ and $\acute{\beta}$. Further to examine the role of various compressibilities $\kappa = 9[\rho^2 \frac{\partial^2}{\partial\rho^2}(\frac{E}{A})]_{\rho=\rho_0}$, the above equation can be written in a generalized

form as:

$$V^{Sky} = \frac{\acute{\alpha}}{2}\left(\frac{\rho}{\rho_0}\right) + \frac{\acute{\beta}}{\acute{\gamma}+1}\left(\frac{\rho}{\rho_0}\right)^{\acute{\gamma}}. \tag{2.29}$$

The above mentioned equation describes the equation of state and correlates pressure with energy. Also, it has been discussed in Ref. [11] that the energy of the equation of state can be classified into two parts i.e., thermal and compressional energy. One can also reproduce equation of state on the basis of different $\acute{\gamma}$ values. Evidently, the higher (lower) values of $\acute{\gamma}$ represents the stiffer (softer) equation of state. The $\kappa = 200$ MeV and 380 MeV corresponds to the soft and hard equation of state, respectively.

The total baryon-baryon potential V_{ij} can be expressed as:

$$\begin{aligned} V_{ij} &= V_{ij}^{Sky} + V_{ij}^{Yuk} + V_{ij}^{Coul} + V_{ij}^{MDI} \\ &= t_1\ \delta(\mathbf{r}_i - \mathbf{r}_j) + t_2\ \delta(\mathbf{r}_i - \mathbf{r}_j)\rho^{\gamma'-1}((\mathbf{r}_i + \mathbf{r}_j)/2) \\ &\quad + t_3\ \frac{e^{-|\mathbf{r}_i - \mathbf{r}_j|/\omega}}{|\mathbf{r}_i - \mathbf{r}_j|/\omega} + \frac{Z_{eff}^2 e^2}{|\mathbf{r}_i - \mathbf{r}_j|} \\ &\quad + t_4\ \ell n^2[t_5\ (\mathbf{p}_i - \mathbf{p}_j)^2 + 1]\ \delta(\mathbf{r}_i - \mathbf{r}_j). \end{aligned} \tag{2.30}$$

It is worth noting, that the validity of the above equation is for the cold matter only. It is clearly evident that the matter during the course of collisions. Puri *et al* included the temperature dependance of the mean field in the framework of QMD model and pin down the role of temperature in heavy-ion reaction dynamics [175].

2.1.3 The nucleon-nucleon collisions

As mentioned above, the imaginary part of the G-matrix plays the role of binary nn-collisions. In the structure of the QMD model, the simulations are limited to binary collisions (higher order collisions were not included in the simulations) only. The idea of inclusion of binary collisions in QMD model follows the same procedure as done in the Cascade model calculations. In this framework, two nucleons are said to be scattered if they come closer than a certain distance $\sqrt{\frac{\sigma(\sqrt{s})}{\pi}}$ (where $\sigma\sqrt{s}$ is the total nucleon-nucleon cross-section and '$\sqrt{s}$' is the center-of-mass energy of the nucleons).

The scattering of the nucleons in this model differs from the Rutherford scattering, as the scattering in the former is determined stochastically (using Monte-Carlo procedure). Among various parameterizations given in the literature, the cross section deduced by Cugnon *et al.* is the most frequently used parametrization [176].

The total cross-section ($\sigma\sqrt{s}$) can be divided into two channels: elastic and inelastic. In case of elastic channels (NN→NN), the total cross-section (labelled as σ^{el}) is given by ($\sqrt{s}$ is in GeV, σ in mb, momentum in GeV/c, c = 1):

$$\sigma^{(el)}(\sqrt{s})(mb) = \begin{cases} 55 & \text{if} \sqrt{s} < 1.8993\ GeV \\ \frac{35}{1+100(\sqrt{s}-1.8993)} + 20 & \text{if} \sqrt{s} \geq 1.8993\ GeV, \end{cases} \tag{2.31}$$

with $\sqrt{s} = \sqrt{(E_1 + E_2)^2 - (\mathbf{P}_1 + \mathbf{P}_2)^2}$. Here, E_i and $\mathbf{P}_i$ (i, j = 1, 2) are the energy and momenta of two particles in the center-of-mass of two particle, respectively. The angular distribution for the elastic channels is given by:

$$\frac{d\sigma^{el}}{d\Omega} \sim exp(A'(s).\kappa'), \tag{2.32}$$

where, 'κ'' depicts the squared momentum transfer in the c.m of the colliding particles and A′(s) [in $(GeV/c)^{-2}$] can be computed from $\sqrt{s}$ as:

$$\acute{A}(s) = \frac{6(3.65(\sqrt{s} - 1.866))^6}{1 + (3.65(\sqrt{s} - 1.866))^6}. \tag{2.33}$$

In case of inelastic channels NN→NΔ, the total cross-section (labelled as σ^{inel}) in parameterized form is defined as:

$$\sigma^{(inel)}(\sqrt{s}) = \begin{cases} 0 & \text{if} \sqrt{s} < 2.015\ GeV \\ \frac{20(\sqrt{s}-2.015)^2}{0.015+(\sqrt{s}-2.015)^2} & \text{if} \sqrt{s} \geq 2.015\ GeV. \end{cases} \tag{2.34}$$

The cross-section is expressed in GeV. The angular distribution for inelastic channel is supposed to be isotropic. Based on the criteria that the mass of the two colliding nucleons is nearly equal to 1.876 GeV which defines the limit for $\sqrt{s}$ = 1.8999 GeV. Therefore, constant cross-section (= 55mb) is used for the two colliding nucleons with very small velocity.

Each scattered partner undergoes the check for Pauli blocking. To decide whether the scattering is blocked or allowed, the phase space around each scattered partner is checked [11]. Evidently at low incident energy, most of the collisions are Pauli blocked. This condition gets nullified at high incident energies. Here, it is important to mention that the equation of state and cross-section discussed till the end, is legitimate for cold nuclear matter only [11].

Pauli blocking:

It is one of the most significant quantum attribute. The phase space of nucleons generated through the QMD model is further subjected this check. Each nucleon is assumed to occupy a sphere in the momentum and coordinate space [11, 141]. This trick yields same Pauli blocking as obtained by using Gaussian wave packets. The already occupied fractions P_1 and P_2 in the phase space are determined for each scattering partners. The probability of the binary nucleon-nucleon collision to be accepted (P_{allow}) reads as:

$$P_{allow} = 1 - [1 - min(P_1, 1)][1 - min(P_2, 1)], \tag{2.35}$$

which is blocked with probability P_{block} =[1 - P_{allow}]. The present QMD model yield blocked probability is close to 96 % at ground state. For complete stopping, this value should be unity. The Pauli blocking plays a crucial role at low incident energies in contrast at high incident energies where binary collisions govern the dynamics of the reaction. It is worth mentioning that in-medium cross-section differs significantly from the free cross-section at low incident energies. Both in-medium and free cross-section merge at higher incident energies.

2.2 Other variants of molecular dynamics model

Lately, many improvements and transformations have been made over the original QMD model to extend its legitimacy from low to high incident energy domain with new degrees of freedom. The Quantum Molecular Dynamics (QMD) model has been further amended in various ways to investigate the low energy reactions resulting in Binding Quantum Molecular Dynamics (BQMD) model [145], Pauli Quantum Molecular Dynamics (PQMD) model [146], Extended Quantum Molecular Dynamics (EQMD) model [137], Improved Quantum Molecular Dynamics (ImQMD) model [139, 140], Fermionic Molecular Dynamics (FMD) model [138]. On the other hand in the high energy domain, Relativistic Quantum Molecular Dynamics (RQMD), Ultra Relativistic Quantum Molecular Dynamics (UrQMD) models were developed [150–153].

Bohnet *et al.* refined the original version of the QMD model to describe the proper binding energy of target and projectile and termed it as Binding Quantum Molecular Dynamics (BQMD) model [145]. The BQMD model is quite consistent in explaining various processes at low incident energies. The local binding energy of all the nucleons

constrains the maximum Fermi momentum so as to keep all the nucleons bound in a nucleus. Unlike in the QMD model where Gaussian type distribution is considered, the nucleons in the BQMD model were represented by Woods-Saxon type distribution.

Another modified version of the QMD model has been developed by Peilert *et al.* that includes Pauli potential and has been termed as Pauli Quantum Molecular Dynamics (PQMD) model [146]. The PQMD model utilizes the strong repulsive potential that depends on the inter-particle separation between nucleons in the phase-space. The idea of inclusion of Gaussian Pauli potential defined by Dorso *et al.* is worthwhile in phase-space as it does not permit two nucleons to come too close to each other [177]. The QMD approach in addition to Pauli potential manifests the model with defined ground states which is also capable to give the proper excitation energy of the fragments. Further, efforts were done to incorporate the time-dependent Gaussian width coupled with phenomenological Pauli potential into effective interactions in QMD model which is dubbed as Extended Quantum Molecular Dynamics (EQMD) model [137]. This approach has proficiently explained the ground state properties of nucleus such as binding energies, density profiles or α-clustering structure in light nuclei structure over the wide mass range.
In another approach, Wang *et al.* modified the original version of QMD model dubbed as Improved Quantum Molecular Dynamics (ImQMD) model by introducing the symmetry energy and surface terms in the potential energy part to explore the physics behind the heavy-ion fusion at low incident energies [139, 140]. These improvements also include the system size dependent wave packet to study the evolution of the wave packet width.
Likewise, the ImQMD model consider the antisymmetrization in the structure, a constraint on the occupied phase space is implemented and isospin-dependent nn-cross section is also taken into account to consider Pauli blocking [146]. In this approach, the Relativistic Mean Field (RMF) calculations are used to obtain neutron and proton density distributions.

Further, another new variant of ImQMD model i.e, ImQMD-II was developed by including two new additional features in the interaction potential energy based on the Skyrme interaction of SkM* and SLy series [140]. This model successfully described the ground state properties of exotic as well as of stable nuclei. The improved QMD model has been further modified, to consider increasing proximity between the reacting partners and surface interaction; the shell effect term and the switch function method were also introduced, respectively [178]. In this model, the fusion reactions close to Coulomb

barrier, the doubly magic nuclei, the halo nuclei induced reactions and fusion dynamics of superheavy nuclei were studied systematically [178].

In order to study the inelastic channels of baryon-baryon and meson-baryon collisions and also the decay of resonances for the production of pion and strange particles; updated version of improved ImQMD model is introduced dubbed as the Lanzhou Quantum Molecular Dynamics (LQMD) model [179]. In this model, due to inclusion of momentum dependence of the symmetry potential, the effective mass of nucleons gets differentiated in the nuclear medium. In LQMD model, the transverse emissions and ratios of the pions ($\frac{\pi^-}{\pi^+}$) and kaons ($\frac{K^-}{K^+}$) are found to depend strongly on the momentum dependance of symmetry energy. In this model, nucleons, baryons, resonances, and mesons in the system propagate in the self-consistently generated mean field. The LQMD model is also widely used to study the high density behavior of the symmetry energy extracted from the heavy-ion collisions [179].

With the increase in the incident energy, the velocity of the nucleons approaches the velocity of light, therefore, demands complete relativistic theory. To address relativistic effects, Lehmann and Puri *et al* extended the legitimacy of present QMD model upto relativistic energies using Covariant dynamics in the same manner as followed by Sorge *et al.* [180]. This model is termed as Relativistic Quantum Molecular Dynamics (RQMD) model. The collision term is modified by incorporating heavy baryon-resonances, strange particles and string excitation for high energy hadron-hadron interaction. The RQMD model reported the same results in non relativistic limit of incident energy (< 50 MeV/nucleon), although the results of QMD and RQMD differs significantly at high energy. Waged *et al* developed another model to study the heavy-ion collisions at high incident energies [181]. This new approach was developed in the framework of Glauber theory coupled with QMD model (dubbed as DQMD model).

To study pp (proton-proton), pA (proton-nucleus) and AA (nucleus-nucleus) correlations at high incident energies the *Frankfurt group* developed a ultra relativistic variant of QMD model termed as Ultra Relativistic Quantum Molecular Dynamics (UrQMD) model within the large energy domain from BEVALAC and SIS (1GeV/nucleon) upto SPS (200 GeV/nucleon) and energies in colliders like RHIC ($\sqrt{s}$ = 20 GeV/nucleon) and Large Hadron Collider (LHC) [182]. The framework of UrQMD model resembles closely with the structure of QMD and RQMD models. The structure of UrQMD is assimilated with all the necessary physics that is major prerequisite for studying nuclear dynamics at low,

intermediate and high energy.

The inconsistency of QMD model to include fermionic nature prompted the advancement which led to the development of Antisymmetrized Molecular Dynamics (AMD) and Fermionic Molecular Dynamics (FMD) models. In these models, wavefunction of the system is described by the Slater determinant of N-wave packets. Now, to study fermionic nature of nucleons, antisymmetrization of the wavefunction has been taken into consideration in various methodologies. These methodologies are: Fermionic Molecular Dynamics (FMD) model [138], Antisymmetrized Molecular Dynamics (AMD) model [132–134] and Constrained Molecular Dynamics (CoMD) model. In FMD model, the system of fermions is depicted by an antisymmetrized N-body wavefunction that is constructed from the single-particle wave-packets of Gaussian shape. The antisymmetric feature of N-body system in this model takes into account the Pauli principle with respect to particle exchange. It also ensures the correct treatment of Fermionic motion and shell model properties. The low energy phenomena such as fusion-fission and the features of nuclear structure are appropriately described within framework of FMD model.

Modification in the FMD approach has been done by including stochastic collision term and consequently, Ono *et al.* developed the Antisymmetrized Molecular Dynamics (AMD) model [132–135]. This model calculated the rms radius (=2.49 fm) of $^{12}_{6}$C which could explain the previous discrepency of the ^{12}C nuclei [134]. In contrast to FMD approach where the dynamical width parameter is considered, the AMD approach takes into account the Gaussian width that remains constant with time. This simplification in the structure of AMD model saved the computational time of calculations but at the expense of flexibility of the description, in comparison to the FMD model, as long as the stochastic extension terms are not considered [183]. The AMD model lacks in describing the quantum-mechanical mixing of shell-like and clusterlike configuration and also the wave nature of the nucleons. Therefore, the modified rendition of the AMD model, Antisymmetrized Molecular Dynamics superposition of selected snapshots (AMD triplet-S) has been utilized to demonstrate the cluster-shell competition of these nuclei [184]. This methodology works on the idea of the Stochastic Variational Method (SVM).

Although, the nuclear reaction and structure of light nuclei are very well explained in the AMD and FMD models, the criteria of solving Slater determinant consumes huge computational time, therefore, limits its utilization to the lighter system only. Papa *et al.* imposed additional constrains on the occupation probability (i.e., $f \leq 1$) to make the

calculations faster so that the heavier nuclei can be studied [142, 143].

The updated version of Constrained Molecular Dynamics (CoMD) model i.e., CoMD-II [143] resolved the problem of non-conservation of angular momentum that affects other semi-classical microscopic approaches due to the presence of hard core repulsive interaction and more generally the usage of random forces. In the above prescribed methodologies, the mean field and collisions are not considered in a self consistent manner. In other words, the nuclear mean field and in-medium nn-collisions are characterized independently. The parameterized version of the nn-collisions invincibly affects the observables that carry crucial information about the nuclear equation of state. Hence the in-medium cross section utilized in a transport model ought to be resolved reliably before complete data about the equation of state can be obtained. This improvement in the QMD model approach has been done by Jaenicke *et al.*, based on the Brueckner-Bethe-Goldstone equations using Reid soft core potential that is further utilized to determine both effective nn-potential as well as nn-cross section microscopically [185].

The inclusion of temperature in the mean-field potentials of nucleons derived from realistic G-matrix has been done by Puri *et al.* and dubbed it as Temperature Dependent Quantum Molecular Dynamics (TQMD) model [175, 186] . In the framework of QMD model, the local temperature of the i^{th} particle in each time step is calculated which is further used to compute temperature dependent potential in the simulation. In nuclear matter, the temperature dependent potential was obtained by computing the Bethe-Goldstone equation at finite temperature.

2.3 Isospin-dependent Quantum Molecular Dynamics (IQMD) model

The Isospin-dependent Quantum Molecular Dynamics (IQMD) model developed by Hartnack *et al* inherits the majority of its features from VUU model [141, 187, 188]. It is an extension of the original QMD model. In the framework of IQMD model, different charge states of nucleons, deltas and pions are treated explicitly. The isospin degree of freedom has been included in the model through the nucleon-nucleon scattering cross section, Coulomb potential as well as symmetry potential (in a similar way as in IBUU model). Since the framework of IQMD model is a close analogue to the QMD model, for this reason it also comprise of three steps i.e., initialization, propagation and scattering. The

procedure followed by IQMD model at each step differs from the QMD model to some extent. The procedure followed by IQMD model in the first step of initialization follows the distribution of the centroids of Gaussians of the nucleus distributed arbitrarily in a phase space sphere. The distribution in the phase space sphere (r $\leq$ R, p $\leq \mathbf{P}_F$) is within the radius R = 1.12 $A^{1/3}$ that corresponds to the ground state density of ρ_0 = 0.17 fm^{-3} and momentum sphere $\mathbf{P}_F \approx$ 270 MeV/nucleon. The Fermi momentum in the IQMD model is computed using Fermi gas model. The Fermi momentum is strongly dependent on the ground state density. The momenta are uniformly distributed within the momentum sphere, therefore, nucleons close to the surface are initially unbound. This as a result leads to the reduced binding energy of the initialized nucleus. On the contrary, a stronger stability of density profile is achieved in the IQMD model due to full Fermi energy available in the framework of IQMD model. Although the IQMD model provides comparatively stable density distribution and good energy conservation but this is on the cost of nuclear evaporation and improper binding energies ($E_{bind} \approx$ 4-5 MeV/nucleon for heavy nuclei rather than 8 MeV/nucleon). Another characteristic property that differentiate IQMD model from QMD model is the Gaussian width 'L' which is a measure of the interaction range. In the framework of QMD transport model, the Gaussian width is kept constant whereas in the IQMD model it varies in accordance to the system size i.e., 2.16 fm^2 for Au and 1.08 fm^2 for Ca nucleus. The inclusion of the system size dependence 'L' in the IQMD guarantees the maximum stability of the density profile of the target and projectile.

As mentioned above, the IQMD model encompass isospin factor in the form of symmetry potential and Coulomb potential in its framework. The Coulomb potential is given in the same form as expressed in Eq. (2.26) in QMD model. The potentials such as Skyrme, Yukawa and momentum dependent given in QMD and IQMD model are isospin independent, the key role of isospin factor in IQMD model (included in QMD model) is attributed to the symmetry potential. The symmetry potential in the IQMD model can be given as:

$$V^{sym} = \sum_{j;i\neq j} t_6(1/\rho_0)\ T_{3i}T_{3j}\delta(\mathbf{r}_i - \mathbf{r}_j), \tag{2.36}$$

where t_6 = 100 MeV and T_{3i} and T_{3j} depict the isospin projection of the i^{th} and j^{th} particles (i.e., +1/2 and -1/2 for protons and neutrons, respectively).

The role of nuclear symmetry energy and its density dependence has been viewed as one of the most undetermined characteristic property of the isospin-asymmetric neutron-rich nuclear matter. Consequently, the momentum dependence of the symmetry energy is also termed as one of the most engrossing topic in the field of nuclear physics today. Therefore, the total interaction potential ('V_{ij}') in IQMD model differs from the QMD model (given in Eq. (2.30)) in terms of symmetry potential only. The total binding energy of the nucleus in the ground state is computed using the expectation value of the total Hamiltonian.

The IQMD model differs from QMD model in terms of cross-section parameterization in the framework. In QMD model, the nucleon-nucleon collisions use Cugnon parameterization while in framework of IQMD approach, Vernst and Arndt parameterization have been considered [189]. For describing the elastic nucleon-nucleon collisions the experimental parameterization has been taken into account. Although the method followed to treat the collisions in IQMD model is similar to the QMD model but Pauli blocking is isospin-dependent. This implies that this feature checks the occupied phase space of the scattered partners in accordance to the isospin of the already scattered partners. Besides the formation of nucleons and deltas (as in QMD model), pions are also formed through the decay of delta resonance in IQMD model.

The utility of IQMD model has been large to extract numerous observables over the broad energy range. Hartnack *et al.* [141] has not been only one to develop IQMD, various other groups have also done efforts in this direction to further modify QMD model. In another approach the isospin degree of freedom has been included in QMD model by Chen *et al* and dubbed it as Isospin-dependent Quantum Molecular Dynamics (IQMD) model [190]. Although the isospin dependence in structure of this model has been included through mean field, binary nucleon-nucleon collisions and Pauli Blocking but differs from IQMD model developed by Hartnack *et al.* in number of aspects. For instance, the two models differ in the procedure followed for initialization (in considering Gaussian width), the separate treatment is given to neutron and proton due to their different behavior of their density distribution in nuclei far from the β-stability line. The value of interaction range in IQMD model by Chen *et al.* is considered fixed with value 2 fm^2. The isospin-dependent nucleon-nucleon scattering cross section uses experimental parameterizations given by Chen *et al.* [190]. Here, the total interaction potential (i.e., sum of Skyrme, Yukawa, Coulomb and symmetry) considered is similar to the potentials

given in IQMD model developed by Hartnack *et al.* This model has also been used to study isospin-dependence in various phenomena such as fragmentation, collective flow etc. at intermediate energies. Further, this model has been improved by adding Pauli potential and symmetry energy in its framework to stabilize the cold nuclei [82, 174, 191]. This model has been utilized to study phenomenon such as fragmentation, collective flow and also different forms of symmetry potential [66].

The models discussed above are primary models that are utilized to generate the phase space of nucleons. Subsequently, there is necessity of secondary algorithms to clusterize the phase space of nucleons into stable fragments. The detailed range of secondary algorithms will be discussed in chapters 3 and 4.

Chapter 3

Role of clusterization algorithms on the cluster formation and phase-transition in nuclear matter

As discussed in chapter 1, the similarity between nucleon-nucleon interactions (short-range repulsive and long-range attractive parts) and the Van der Waal's forces between molecules indicates the existence of a liquid-gas phase transition in excited nuclear matter [43–46, 49, 58, 59, 87, 109, 192–201]. Conversely, based on the similarity between the equations of state for both phases (that differs approximately by five orders of magnitude), it is considered that like liquid-gas phase transition in macroscopic systems, multifragmentation phenomenon must also contain some signals of the phase-transitions in nuclear matter [43–46, 49, 58, 59, 87, 109, 192–201]. Lately, the same idea was proposed in other fields also such as astronomical and micro-systems (atomic clusters and nuclei). The nuclei as finite system are enticing more and more physicists to find and examine the behavior of liquid-gas phase transition. In this direction, it was found that the mass/charge yields when fitted as a function of mass (A_f)/charge (Z_f) obey a power-law [$\mathrm{Y}(A_f) \propto {A_f}^{-\tau}/\mathrm{Y}(Z_f) \propto {Z_f}^{-\tau}$] at a certain excitation energy; the plausible signal of the liquid-gas phase transition in nuclear matter [43–46, 58, 87, 109, 192–200]. Such a signal was first noted by the Pioneer Purdue group [58]. Later on, this behavior was also reported by various other theoretical groups and was found to be in accordance with the earlier predictions of the Fisher's droplet model [44, 46, 87, 109, 192, 193]. It is worth mentioning that the occurrence of a phase-transition in multifragmentation phenomenon was also questioned in some studies. The study conducted by Porile *et al.* [202] presented one such classical example.

3.1 Different approaches to study phase-transition

The occurrence of phase-transition in nuclear matter has been predicted using two different approaches:

1. Using those models that predict the phase-transition based on the breaking of nuclear matter at subnormal densities,
   and;

2. using the evolution of the decay mechanism of nuclei as a function of excitation energy.

Though, the former one is purely a theoretical concept, the latter one, however, can be used to pin down the phase transition experimentally as well [43–46, 58, 87, 109, 192–194, 199–201]. In the present work, we will focus on the latter method. In this method, the critical point of the phase-transition (also termed as the onset of multifragmentation) corresponds to a minimum in the value of the critical parameter (τ) when plotted as a function of incident energy [46, 58, 87, 194, 196, 200].

3.2 Secondary algorithms (Fragment recognition methods)

As noted in previous chapters, the primary models (both statistical and dynamical models) can be used to study various important phenomena happening at intermediate energy domain such as multifragmentation, collective flow, energy of vanishing flow, etc. The primary models aim to generate the phase-space of nucleons after the collision of the target and projectile with certain geometry and incident energy. The dynamical models are able to provide the complete evolution of the reaction from the well separated target and projectile upto the freeze-out stage of the reaction, whereas the statistical models provide limited information; only at freeze-out time. Additionally, the dynamical models encompass all the features to successfully explain physics behind the heavy-ion collisions at intermediate energy [11, 12, 32, 141, 168–172]. The many-body dynamical models such as Quantum Molecular Dynamics (QMD) model follows the evolution of individual nucleons as independent systems. These types of models generate the phase-space of nucleons at various stages of the reaction.

The information obtained through dynamical models is further subjected to the secondary algorithms. The aim of using secondary algorithms is to identify stable fragments. These secondary algorithms are termed as "clusterization algorithms". To implement the clusterization algorithm, one usually treats each individual nucleon, independently. Usually, the final fragment configuration is frozen when the hot expanding system expands to well below the normal nuclear density. In the present framework, the freeze-out time is decided in accordance with the Gross *et al.* where freeze-out is supposed to occur if fragment configuration remains constant for $t_{freeze} \pm$ 10 fm/c [203]. The important idea behind implementing various clusterization methods is attributed to the fact that one can attain different fragment structures with the same primary model. Therefore, it becomes compulsory to procure comprehensive knowledge related to the formation of fragments with different clusterization algorithms. Various spatial based clusterization algorithms are discussed in the following paragraphs.

3.2.1 The Minimum Spanning Tree (MST) method

It is the one of the most famous and universally used clusterization algorithm to identify various fragments. This method known as the Minimum Spanning Tree (MST) method [11], identifies various fragments on the basis of the distance among nucleons bound in a fragment. Accordingly, two nucleons share the same fragment if their distance, is less than distance R_{clus}. This condition reads as:

$$\mid \mathbf{r}_i - \mathbf{r}_j \mid \leq R_{clus}, \tag{3.1}$$

where $\mathbf{r}_i$ and $\mathbf{r}_j$ in coordinate space, are the centroids of the i^{th} and j^{th} nucleon, respectively. The value of R_{clus} can vary between 3 - 6 fm. Here, it is worth mentioning that the role of varying R_{clus} at freeze-out time is insignificant. Primarily, the R_{clus} value is considered to be 4 fm.

Although the MST method is quite simple and fast but its pertinence is only legitimate at freeze-out stage. The framework of this method is not accomplished enough to study the hot and dense compressed state of nuclear matter (i.e., before freeze-out). Lately, the different R_{clus} values for protons and neutrons has also been suggested [204].

3.2.2 The Minimum Spanning Tree method with Momentum (MSTP) cut

Evidently, the MST method does not remark on the stability of fragments therefore, to avoid the formation of loosely bound/unbound fragments, the relative momenta of the nucleons is also constrained in addition to their coordinate space [154, 155]. This method was labelled as the Minimum Spanning Tree method with Momentum cut (MSTP or MSTM) method. Accordingly, we demand:-

$$\mid \mathbf{r}_i - \mathbf{r}_j \mid \ \leq R_{clus} \ ; \ \mid \mathbf{p}_i - \mathbf{p}_j \mid \ \leq \ \mathbf{p}_{Fermi}, \tag{3.2}$$

where $\mathbf{p}_i$ and $\mathbf{p}_j$ are the momentum coordinates of i^{th} and j^{th} nucleons, respectively, and $\mathbf{p}_{Fermi}$ is the Fermi-momentum of the nucleons bound in a nucleus at its ground state. This formalism rejects all those nucleons which are too far in the momentum space.

3.2.3 Binding energy based clusterization algorithm

Sometimes, in the MST and MSTP methods, one cannot separate two structure fragments if they share a single slow moving surface nucleon. An alternative method to remove above mentioned ambiguity is to first recognize the "pre-clusters" using the MST method and then check their stability using their binding energy. In this algorithm, the realization of the fragment structure depends on the interactions and relative kinetic energy of the nucleons of a given fragment identified by the MST method. The following mechanism is adopted for identifying such realistic fragments:

1. Identify the clusters using the MST method,
   and;

2. then subject each such fragment to the following binding energy check:

$$\zeta = \sum_{i=1}^{A_f} \left[\frac{\left(\mathbf{p}_i - \mathbf{p}_{A_f}^{cm}\right)^2}{2m} + \frac{1}{2}\sum_{j\neq i}^{A_f} V_{ij}(\mathbf{r}_i, \mathbf{r}_j) \right] < E_{bind}. \tag{3.3}$$

with E_{bind} = -4.0 $\times$ A_f MeV if $A_f \geq 3$ and $E_{bind} = 0$, otherwise. In the above equation $\mathbf{p}_{A_f}^{c.m.}$ represent the center-of-mass momentum of the fragment, respectively. The probability to sustain fragment for long depends on the E_{bind} (binding energy) [156, 157, 205].

If any fragment is not able to fulfil the condition mentioned in eq. (3.3), then this pre-fragment is treated as unbound and all the nucleons of the pre-fragment are considered as free nucleons. In this approach of the MST method in which constant binding energy constrain was incorporated is dubbed as MSTB (1.1). The MSTB (1.1) not only removes the unbound fragment structures but also improves the fragment identification time to large extent [156]. Puri *et al.* further modified this approach by implementing the binding energy condition where E_{bind} was computed using modified Bethe−Weizsäcker mass-formula [156]. This version was termed as MSTB (2.1).

Generally, one can use the binding energies corresponding to a cold or hot nucleus. Recently, it has already been shown that one should implement thermal binding energies instead of cold binding energies to filter the unstable fragments at the time of their identification. This method is dubbed as Minimum Spanning Tree with Thermal Binding energy cut (MSTBT) [157]. We will continue with this approach in this work also and will implement only temperature-dependent binding energies to filter the unstable fragment structures. In this method, the excitation energies of various fragments are taken into account and E_{bind} is calculated using the so called temperature-dependent binding energy formulae. Interestingly, for the hot binding energies, various formulae were proposed in the literature [206–208]. We shall discuss some of these formulae in the following paragraphs [156, 157]. Here, we shall use three different temperature-dependent binding energy formulae proposed by Davidson *et al.* [206], Pi *et al.* [207] and Sauer *et al.* [208]. A few details of the temperature-dependent binding energy formulae will be discussed in the next section:

3.2.4 Different temperature-dependent binding energy formulae

Davidson *et al* formula:

The first formula put forwarded by Davidson *et al.* uses the canonical ensemble theory. This formula reads as:

$$E_{Bind}(T) = \alpha(T)A_f + \beta(T)A_f^{2/3} + \left(\gamma(T) - \frac{\eta(T)}{{A_f}^{1/3}}\right)\frac{(4{t_\varsigma}^2 + 4|t_\varsigma|)}{A_f} + 0.8076\frac{{Z_f}^2 R(0)}{{A_f}^{1/3}R(T)}$$
$$\left(1 - \frac{0.7636}{{Z_f}^{2/3}} - 2.29\frac{R(0)^2}{[R(T){A_f}^{1/3}]^2}\right) + \delta(T)\frac{f(A_f, Z_f)}{{A_f}^{3/4}}, \quad (3.4)$$

where $t_\varsigma = (2Z_f - A_f)/2$ represents the isospin asymmetry of a nucleus and $f(A_f, Z_f)$ = (-1, 0, 1) for even-even, even-odd and odd-odd nuclei, respectively. It is important to note here that the relation of nuclear radius is not computed using fitting, but is derived by parameterizing the weak dependence on temperature. To derive this formula, the excitation energy of a nucleus is fitted according to canonical ensemble theory and is converted into the temperature of the considered system;

$$Q(A_f, Z_f, T) = \sum_{i}^{n} g_i \; exp\Big(- \frac{E_i}{T}\Big) + \int_{E_n}^{E_{max}} dE \; g_{A_f,Z_f}(E) \; exp\Big(- \frac{E}{T}\Big), \tag{3.5}$$

where $g_i = (2j_i + 1)$ is the spin degeneracy factor and E_i is the excitation energy of the i^{th} state of the nucleus (E_n and E_{max} corresponds to the excitation energy of the n^{th} and highest energy state of the nucleus, respectively). The temperature-dependence of the constants $\alpha(T)$, $\beta(T)$, $\gamma(T)$, $\delta(T)$ and $\eta(T)$ was calculated from the available experimental details of the excited states of 313 nuclei in the mass region $22 \leq A_T \leq 250$ by calculating the partition function of respective nucleus in canonical ensemble theory and making a least square fit of the excitation energy to ensemble average using the relation

$$E_i(A_f, Z_f, T) = T^2 \frac{\partial}{\partial T} \; ln \; Q(A_f, Z_f, T). \tag{3.6}$$

It is important to mention that in the present study, no refitting of the coefficients of the formula is done; instead the actual form of the expressions given in Ref. [206] is used. The role of shell corrections, pairing terms and deformations is observed to be negligible here [209, 210].

Sauer *et al* and and Pi *et al* formulae:

The other formula implemented for filtering the loosely bound fragments is given as:

$$\begin{aligned} E_{Bind}(T) \;\; = \;\; & (a_v - \alpha_v T^2)A_f - (a_s - \alpha_s T^2)A_f^{2/3} - \left[a_c \left(1 - \frac{a_{Coul}}{A_f^{2/3}} \right) - \alpha_{Coul} T^2 \right] \frac{Z_f^2}{A_f^{1/3}} \\ & -(a_{sym} - \alpha_{sym} \times 10^{-4} T^2) \frac{(A_f - 2Z_f)^2}{A_f} + (a_{ss} + \alpha_{ss} T^2) \frac{(A_f - 2Z_f)^2}{A_f^{4/3}}. \end{aligned} \tag{3.7}$$

Here Z_f is the the charge of the fragment, respectively. This formula was proposed by

Sauer *et al.* [208] and Pi *et al.* [207] using two different theories. Sauer *et al.* obtained this formula by employing the Thermal Hartree-Fock (TDHF) Approximation, whereas Pi *et al.* used hot Thomas-Fermi calculations. In the first case, the density of the nucleus was considered to be somewhat greater at the interior compared to its surface, but in the latter case, the density was considered to vary continuously from the interior to the surface. Also, Pi *et al.* considered the contribution of the surface nucleons towards the nuclear symmetry energy; in contrast to Sauer *et al.,* who ignored this contribution. In the case of the formula by Sauer *et al.,* the coefficient a_{Coul} was set to be zero, whereas a_{Coul} was taken to be 3.1445 by Pi *et al.*. We find that the formula proposed by Pi *et al.* is more accurate compared to Sauer *et al.* for lighter mass nuclei. The parameter set used in the formulae of Sauer *et al.* and Pi *et al.* are listed in Table 3.1. On the contrary, the parameter set used in the binding energy formula of Davidson *et al.,* is extracted from the graphical representation reported in Ref. [206].

The versions of the MSTBT method with binding energy formula of Davidson *et al.*, Pi *et al.* and Sauer *et al.* are termed as MSTBT (3.1), MSTBT (3.2) and MSTBT (3.3), respectively. As far as the extraction of the temperature from non equilibrated system (like typical heavy-ion collisions) is concerned, there are many methods listed in the literature that account for e.g. diffusion of the surface and so on [175]. However, the present formulae are valid upto 4 MeV only. Therefore, using thermal binding energies with fixed temperature is just a case study to understand whether one needs to look at excited fragments in a different way or not. Such assumptions were introduced in our previous work successfully [157].

3.3 Experimental and theoretical approaches to study liquid-gas phase transition

The significant number of studies have been performed by 4π group at Michigan State University (MSU), Michigan, USA, Equation of State (EOS) collaboration at BEVALAC, INDRA 4π array group and ALADIN group at GSI. Li *et al.* [87] reported experimental findings of the charge spectra of fragments emitted in the reactions of ^{40}Ar+^{45}Sc and observed a minimum in the critical exponent (τ) at incident energy of 23.9 ± 0.7 MeV/nucleon. The percolation model was also used in this study for theoretical understanding [46, 87]. In another experiment, Ogilvie *et al* [43] reported the existence of

Table 3.1: Parameters of the temperature-dependent binding energy formulae of Pi *et al.* [207] and Sauer *et al.* [208] used in the present work. All values are in MeV.

Label	a_v	a_s	a_c	a_{sym}	α_v	α_s	α_{Coul}	α_{sym}	a_{ss}	α_{ss}
Pi *et al*	16.00	20.80	0.7714	33.960	0.064	0.2238	0.00102	71.50	71.54	0.8184
Sauer *et al*	16.10	19.00	0.7000	30.020	0.055	0.1500	0.00070	60.04	0.0	0.0

the above minimum in the Au induced reactions on C, Al, and Cu targets at incident energy of 600 MeV/nucleon. Similarly, William *et al.* [49] performed the experiment for the reaction of ^{84}Kr+^{197}Au and compared their results to the Statistical Multifragmentation Model (SMM). It is worth mentioning that some studies use exponential fits [$Y(Z_f) \propto e^{-\lambda Z_f}$] rather than power-law fits [$Y(Z_f) \propto Z_f^{-\tau}$] to extract the corresponding minimum [43, 46, 59, 87]. In some studies, it was pointed out that the power-law observation of the mass (charge) distribution is necessary, but not a sufficient condition for extracting the phase-transition or critical point in a heavy-ion reaction. Therefore, various other order parameters such as the moments of the charge distribution, the Campi scatter plots, the multiplicity derivative of the fragment multiplicity, as well as the fluctuation in the charge of the largest fragment, and the second largest fragment, and so on have also been put forward [45, 109, 192, 193, 196–198]. Various groups have studied the phase-transition for symmetric to asymmetric reactions over wide range of system mass combinations. Gilkes *et al.* performed the experiment at EOS collaboration, Berkeley, and reported the role of various observables calculated using charge moments from fragmented system to determine the critical behavior in the finite nuclei [201]. Lately, Wada *et al.* performed experiment using NIMROD multidetector array using the same reactions as in Ref. [109, 192] and examined the phase-transition signals predicted by SMM model [211]. Another experiment has been performed by the group at Texas A & M cyclotron institute for the reaction of ^{28}Si+^{112,124}Sn at incident energies of 30 MeV/nucleon and 50 MeV/nucleon. In this experiment, charge distribution was measured in terms of a critical exponent τ and various observables extracted from the moments of charge distribution. The multidetector i.e., Forward Array Using Silicon Technology (FAUST) has been used to detect charged particles [200]. They used inclusive data to calculate the critical parameter "τ" and second moment of the charge distribution.

Among various transport models, N-body theories such as the Classical Molecular Dy-

namics (CMD) model, Quantum Molecular Dynamics (QMD) model [11] and its isospin-dependent variant [141] enjoy special status since they can preserve the individual correlations among the nucleons. These models were also used couple of times in the past to get glimpse of the phase-transition [44, 192, 212, 213]. In one of such studies, Belkacem *et al* performed a detailed study of various order-parameters for the reaction of ^{197}Au+^{197}Au at 35 MeV/nucleon using Classical Molecular Dynamics (CMD) model [193]. Ma *et al* in another study used isospin-dependent Classical Molecular Dynamics (CMD) model and reported maximum entropy in the event space at the critical point predicting phase-transition [214]. In another case, Ma *et al* [109, 192] examined the reactions of ^{40}Ar on ^{27}Al, ^{48}Ti, ^{58}Ni at 47 MeV/nucleon using the TAMU Neutron Ion Multi-detector for Reaction Oriented Dynamics (NIMROD) set up for various critical parameters [109, 192]. In one of such studies, Ma *et al.* [44] used the QMD model and reported a minimum in τ at 65 MeV/nucleon for the reactions of ^{40}Ar+^{27}Al. On the other hand, Puri *et al.* found a flat behavior of the power-law parameter τ for the reaction of ^{40}Ar+^{45}Sc using the Isospin-Dependent Quantum Molecular Dynamics (IQMD) model [212].

Through a very careful inspection of the literature we note that, only a few studies discussed the influence of input parameters as well as fragment formation criteria on the critical exponents. For example, Li *et al.* [46] varied the initial lattice size from 50 to 800 in percolation model calculations and found a shift in the minimum of τ till lattice size of 500 and no effect was recorded afterwards. In another study, Pan *et al.* [194] varied the critical density (at which fragments are assumed to be formed) in the percolation model and reported a similar effect. In a recent study, Lin *et al.* examined the sensitivity of various phase-transition parameters for primary and secondary fragments using Statistical Multifragmentation Model (SMM) calculations [196]. They showed that the analysis of primary and secondary fragments can influence the critical point observation. The importance of the simultaneous study of various critical parameters, was also put forward.

It should be noted that all the above-mentioned dynamical studies were conducted by employing the Minimum Spanning Tree (MST) method as a fragment identifier [44, 109, 192, 193, 212, 213, 215]. At the same time, improvements over the MST method were also reported time to time (discussed in earlier sections) [11, 44, 109, 154–159, 205]. These modifications range from the simple momentum cut to complicated energy minimization. We must also keep in mind that clusterization method is enforced at certain reaction time to identify fragments. Therefore, one has to also examine the phase transition by keeping

into mind the associated questions such as freeze-out time, initialization, parameters of the clusterization algorithm and so on. In this work, we will focus on the role of these improvements (over the MST method) in deciding the phase-transition in heavy-ion reactions.

3.4 Various signatures that predict liquid-gas phase transition

Theoretical investigation of phase-transition in thermodynamics reveal the strong role of various thermodynamical variables such as free-energy, specific heat, pressure, energy etc. These variables entirely contribute to the theoretical study of nuclear phase-transition. From the set of isotherm curves (discussed in chapter 1), it is obvious that the equation of state obtained from the mean field calculations of nuclear matter was found to resemble Van der Waal's equation of state in ordinary matter. Various dynamical and statistical models have studied the role of various order parameters associated with liquid-gas phase transition. The statistical models report fluctuations at critical point in thermodynamical variables such as free-energy, specific heat, excitation energy as significant signature of liquid-gas phase transition. On the other hand, the dynamical models concentrate on various observables extracted from the fragmented system after multifragmentation. Both theoretical and experimental studies done in the past discuss various signals that help one to predict liquid-gas phase transition, some of which are discussed below:

3.4.1 The caloric curves

The similarity between caloric curves (temperature-energy curve) of ordinary and nuclear matter is quite striking. This triggered the interest of physicists to explore deeper into the topic both experimentally and theoretically. The study of nuclear caloric curves was contemplated by various significant experimental groups such as ALADIN collaboration, EOS collaboration and INDRA collaboration [8, 9]. Associating to all the studies done in the past, caloric curves can be classified into three stages: At excitation energy below 2 MeV/nucleon, the state of nuclear matter corresponds to the liquid phase. Within the energy range between 3 to 10 MeV/nucleon, isotopic temperature remains constant for the broad range of incident energy. This stage corresponds to the co-existence of liquid-gas phase. Further rise in the excitation energy leads to the constant increase

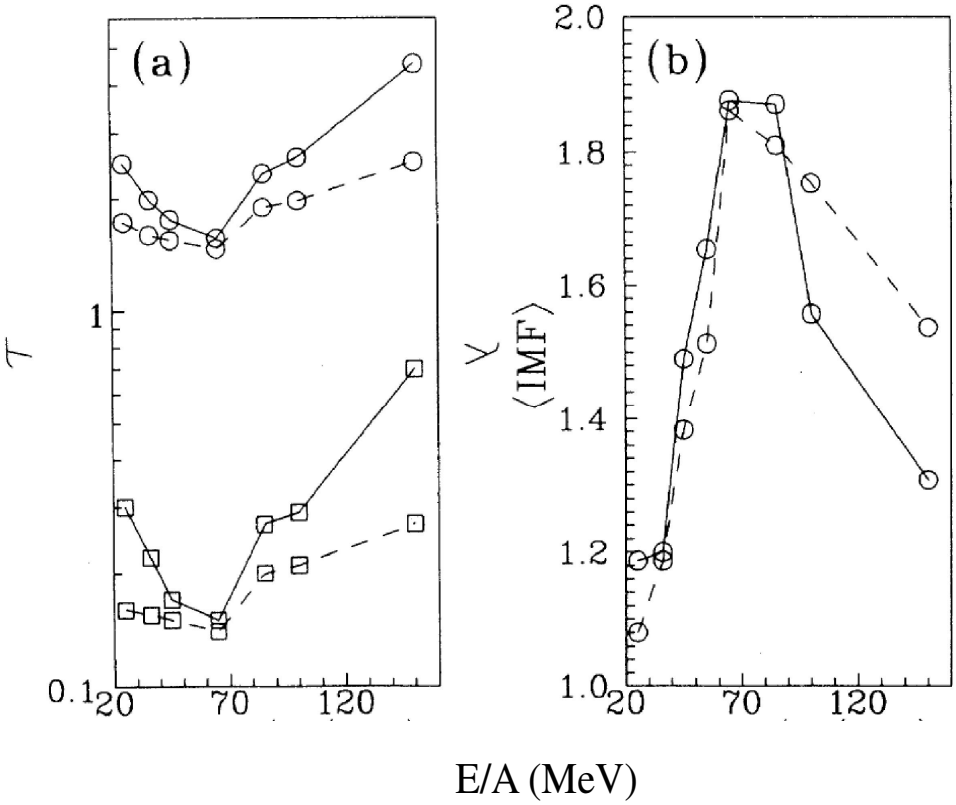

Figure 3.1: The τ and λ calculated by the fit of IMF distribution and average IMF multiplicity as the function of incident energy for ^{40}Ar+^{27}Al reaction. The solid and dashed line in the figure represent the cases corresponding to b = 0 and 2.5 fm, respectively [44]. " Reprinted (Fig. 3) with permission from Y. G. Ma and W. Q. Shen, Physical Review C **51**, 710 (1995), Copyright (1995) by the American Physical Society".

in temperature which can corresponds to gaseous phase or vaporization phase. Many of the caloric curves extracted in the literature are not in agreement with each other. This difference can be attributed to the difference in energy thresholds implemented to measure the isotopic yield. The complexity in performing direct comparison between real and apparent temperatures and small count of nucleons in the nucleus also led to difficulty in measuring the caloric curves. Therefore, there was need of defining better signatures to explore underlying physics behind the phase-transitions in nuclear matter.

3.4.2 The critical exponent τ/λ

As mentioned earlier, the analysis by Purdue group revealed that, mass/charge yields of fragments when fitted as a function of mass (A_f)/charge (Z_f) follow the power-law

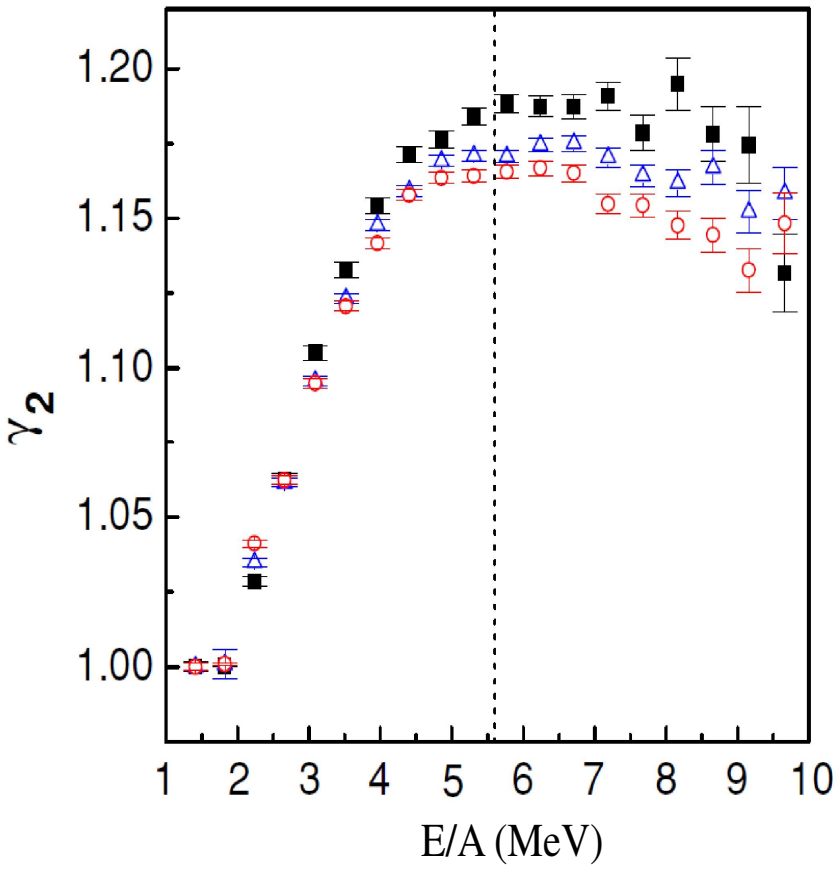

Figure 3.2: The γ_2 produced in the Ar+Al (open circles), Ti (open triangles) and Ni (solid spheres) as a function of incident energy [45]. " Reprinted (Fig. 14) with permission from Y. G. Ma *et al.*, Physical Review C **71**, 054606 (2005), Copyright (2005) by the American Physical Society".

($\propto {Z_f}^{-\tau}$) and exponential fits ($\propto e^{-\lambda Z_f}$) at a certain excitation energy. This led to the conclusion that the fragmenting system is close to the critical point of liquid-gas phase transition [43–46, 58, 87, 109, 192–200]. This idea was initially introduced by the Fisher's droplet model that points to the power-law behavior of liquid drops at the critical point. In this direction, the study done using Lattice Gas Model (LGM) also predict the power-law behavior at the critical point. Fig. 3.1 (a) displays the critical parameter "τ" (calculated from power-law fit) and "λ" (calculated from exponential fit) as the function of incident energy. Similar reports were reported by the group performing calculations with Percolation model [46]. Few experimental groups have also validated the power-law behavior at the critical point. The minimum obtained when these critical parameters are plotted as a function of incident energy also signifies the *onset of multifragmentation*.

3.4.3 The IMF multiplicity

The emanation of Intermediate Mass Fragments (IMFs) gives valuable information about the dynamical evolution of the reactions at intermediate energy. At low incident energies, the IMF production is the unaccustomed phenomenon whereas at high energies the production of large count of light particles governs the domain. Whereas, at intermediate energy the emission of intermediate mass fragments has been both theoretically and experimentally pronounced phenomenon. It is well known that, the multiplicity of intermediate mass fragments shows rise and fall when studied as a function of incident energy [57]. The emission of intermediate mass fragments for central collisions for ^{40}Ar+^{27}Al studied using QMD model has manifested another idea to study liquid-gas phase transition. In Fig. 3.1 (b), we display such results for representation. For instance, the maximum in the multiplicity of IMFs at the critical energy gives another significant evidence to study the onset of multifragmentation.

3.4.4 The moments of fragment charges

Another prominent feature reported by various experimental and theoretical groups is the existence of maximal fluctuations at the critical point in the systems that undergo phase-transition. The thermodynamical cause behind the fluctuations is the disappearance of latent heat at the critical point. Campi proposed the event-by-event correlations to study scatter plots between the largest cluster as a function of normalized second moment

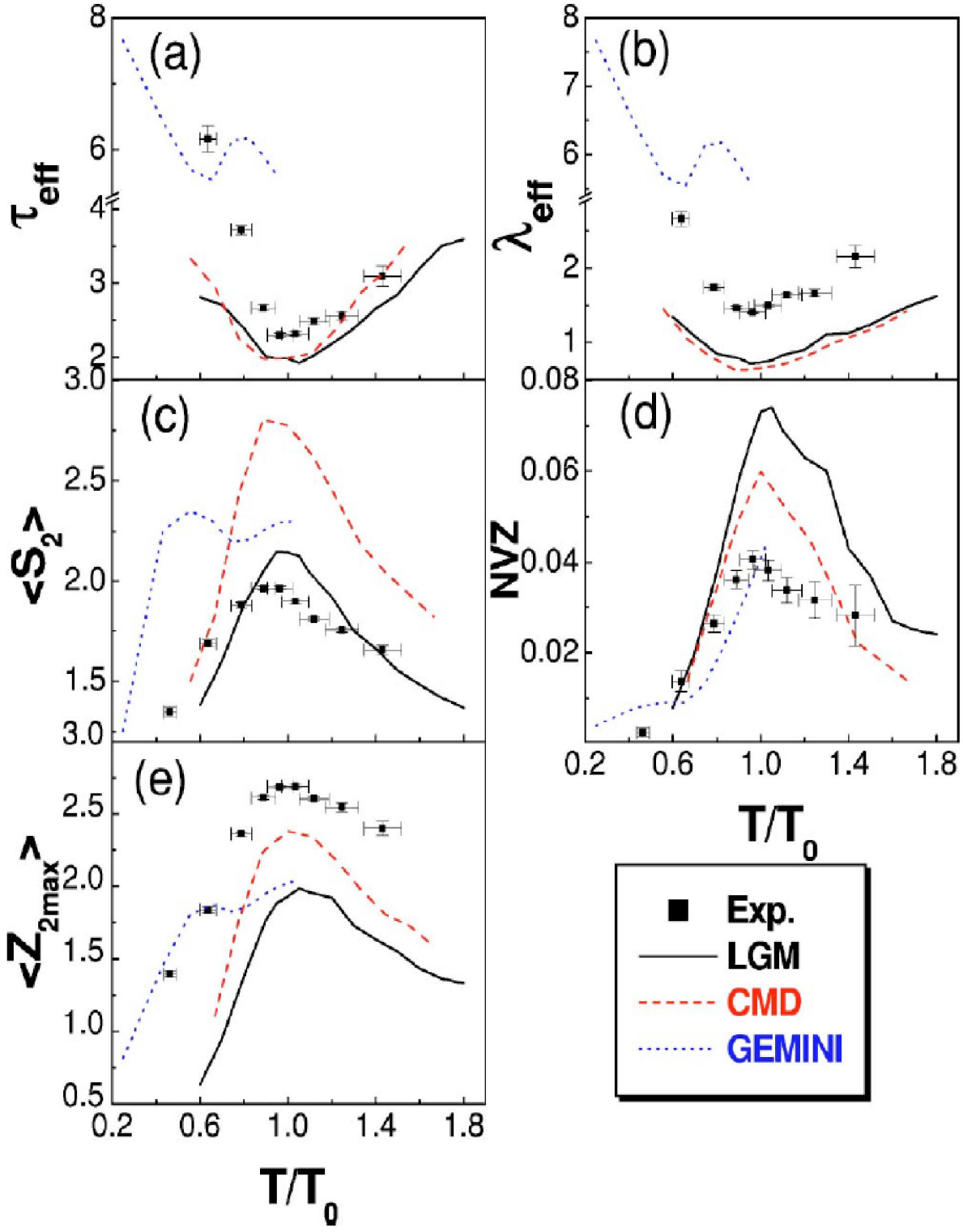

Figure 3.3: The critical parameter τ (τ_{eff}) (a), the exponential parameter λ (λ_{eff}) (b), <S_2> (c), the normalized charge variance (NVZ) (d), the mean charge of the second largest fragment <Z_{2max}> (<Z_{max2}>) (e). " Reprinted (Fig. 3) with permission from Y. G. Ma *et al.*, Physical Review C **69**, 031604 (2004), Copyright (2004) by the American Physical Society".

(excluding the mass of the heaviest cluster). This study introduced "S_2" as an significant observable to predict liquid-gas phase transition. Another quantity, "γ_2" that takes the ratio of moment of charges into account has also been proposed by the same group to study the liquid-gas phase transition. In Fig. 3.2, we display the value of "γ_2" as a function of incident energy of the projectile [109]. From the figure, it can clearly be observed that the maximum in the figure indicates the critical point which can closely be associated with the maximal fluctuations. The detailed description of these observables can be studied in the following section.

The experiment performed by TAMU-NIMROD detector reported various signals that mark the existence of first order phase transition [45, 211]. In this direction, the wide variety of studies have also been performed. The schematic comparison between numerous theoretical and experimental outcomes as a function of temperature is displayed in Fig. 3.3. The figure shows various observables such as critical parameter τ, exponential parameter λ, $<S_2>$, Normalized Charge Variance (NVZ), mean charge of the second largest fragment (Z_{max2}) as a function of incident energy. Clearly, the observables displayed in the figure show deviation in their behavior at the critical point i.e., minima in the Figs. 3.3 (a) and (b) and maxima in Figs. 3.3 (c), (d) and (e). The figure compares the experimental results with standard statistical sequential decay code (GEMINI), the isospin dependent Lattice Gas model, Classical Molecular Dynamics (CMD) model with Coulomb forces [109].

3.4.5 Results and discussions

It is well known that the identification of the fragments based on the spatial correlations should be done when the system is diluted and fragments are well separated. Therefore, in the present study, clusterization algorithms are enforced at a freeze-out time of 300 fm/c where fragments are well separated from each other.

In Figs. 3.4 and 3.5, we display the fragment charge spectra obtained in the central reactions of ^{40}Ar+^{45}Sc at different incident energies between 15 and 115 MeV/nucleon. The results obtained using MST, MSTP, and MSTBT methods are represented by squares, circles, and inverted triangles, respectively. It should be noted that for the discussion of Figs. 3.4 to 3.6, MSTBT results corresponds to the results of MSTBT (3.1) (at 4 MeV) version. From the figure, the well-known trends can be noted. The heavier fragments dominate the spectra at lower incident energies, which is taken over by the lighter frag-

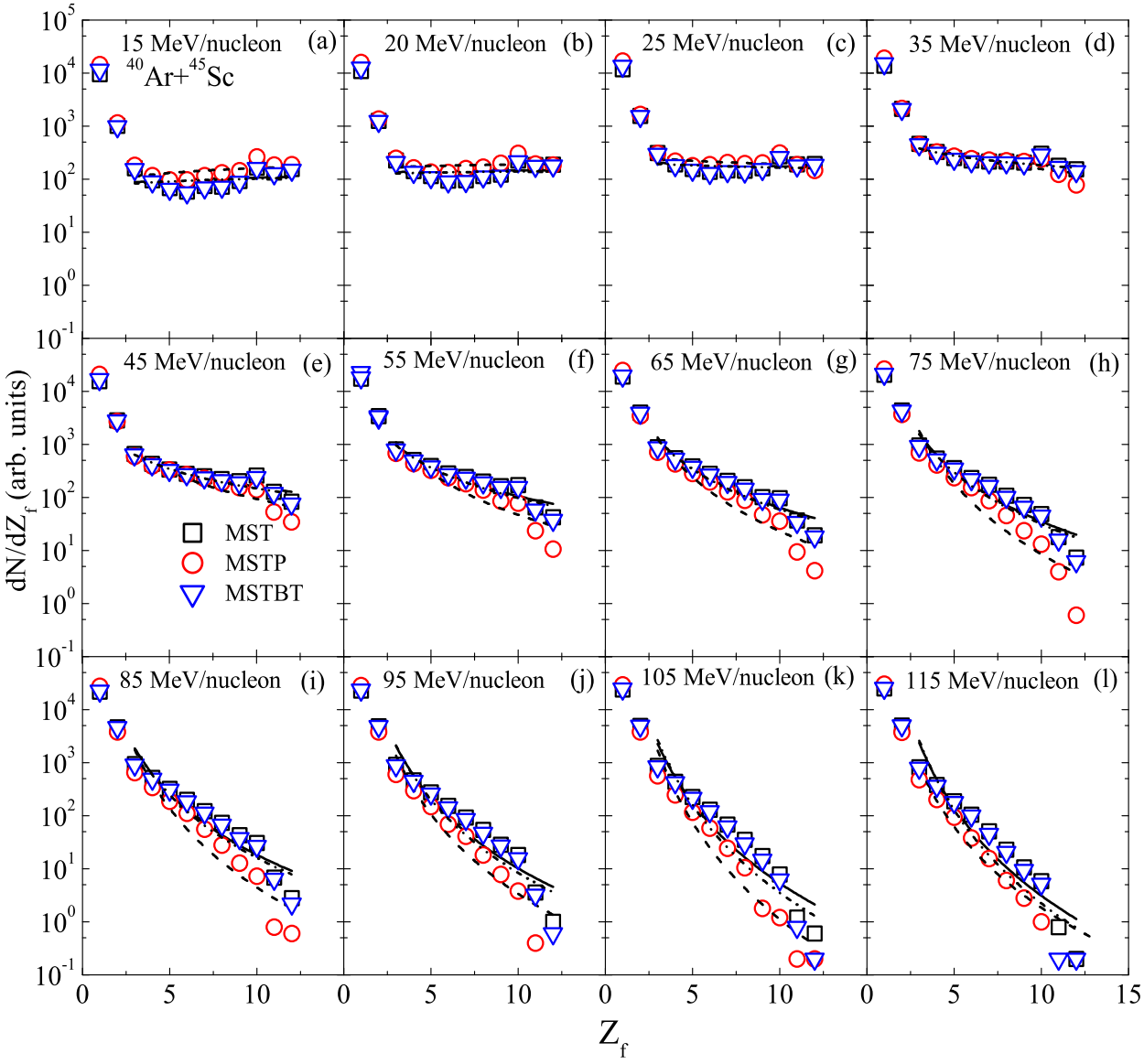

Figure 3.4: The charge distributions of central reactions of ^{40}Ar+^{45}Sc at different projectile incident energies in the range of 15 to 115 MeV/nucleon. The open squares, open circles, and open inverted triangles represent the results using the MST, MSTP, and MSTBT methods, respectively. The lines are to guide the eyes and correspond to power-law fits over fragment charge distributions for IMFs [$3 \leq Z_f \leq 12$].

ments at higher incident energies. At the same time, one sees nearly no effect of different clusterization algorithms on the spectra [44, 46, 49, 87]

Now to see how different algorithms can affect the critical point, the charge yield distribution of intermediate mass fragments is fitted with a power-law ($\propto Z_f^{-\tau}$) (shown in Fig. 3.4) and exponential fitting ($\propto e^{-\lambda Z_f}$) (shown in Fig. 3.5). In Fig. 3.6, the values of τ (upper panel) and λ (lower panel) obtained using different algorithms are plotted as a function of incident energy. Various symbols have the same meaning as in Figs. 3.4 and 3.5. In addition, the calculation with temperature of 2 MeV is also displayed in the figure (labelled as MSTBT′).

Looking at the Fig. 3.6, one notices that the value of $\tau(\lambda)$ increases with projectile's incident energy beyond 20 (25) MeV/nucleon; mimicking the increase in the sharpness of the charge spectra of the fragments. It is worth noting that even though the fragment charge yields (presented in Fig. 3.1) differ significantly for different algorithms, their power-law parameter τ (λ) shows almost similar trends with incident energy within error bars except for the MSTP method, where deviation is more significant. This happens due to a sharp decrease in the probability of the larger charge fragments. The minima in the $\tau(\lambda)$ is obtained using fourth-order polynomial fit as was done in Refs. [46, 87, 212, 213]. The minima in τ (or critical point) is found at incident energies of 18.03, 19.04, and 18.03 MeV/nucleon using MST, MSTP, and MSTBT methods, respectively. Whereas, no minima in τ is obtained in the case of MSTBT′ (inverted lined triangles) method. Similarly, for the exponential fits, the parameter λ has minima at incident energy of 21.06, 19.04, 19.04, and 17.02 using MST, MSTP, MSTBT, and MSTBT′ methods, respectively.

It is worth mentioning that the values of τ (λ) are much lower than the experimentally measured or expected values. This may be due to the lack of exact Fermionic properties (such as specific heat) of the nucleons in the present dynamical model (see Refs. [216, 217]). As mentioned above, the cold binding energies can also be enforced to check the stability of the fragments (dubbed as MSTB method) [156]. Though, we already discarded its use in Ref. [157] here results with MSTB are also displayed for the reference purpose only. Interestingly, no minimum was observed when cold binding energies were used. This further shows that demanding cold binding energies for the fragment filtration is too stringent a condition. Probably one needs to wait longer to have cold fragments, but in that case, one runs into the risk of having spurious fragments. On the other hand, the use of thermal binding energy seems to be a reasonable condition. As noted, all different

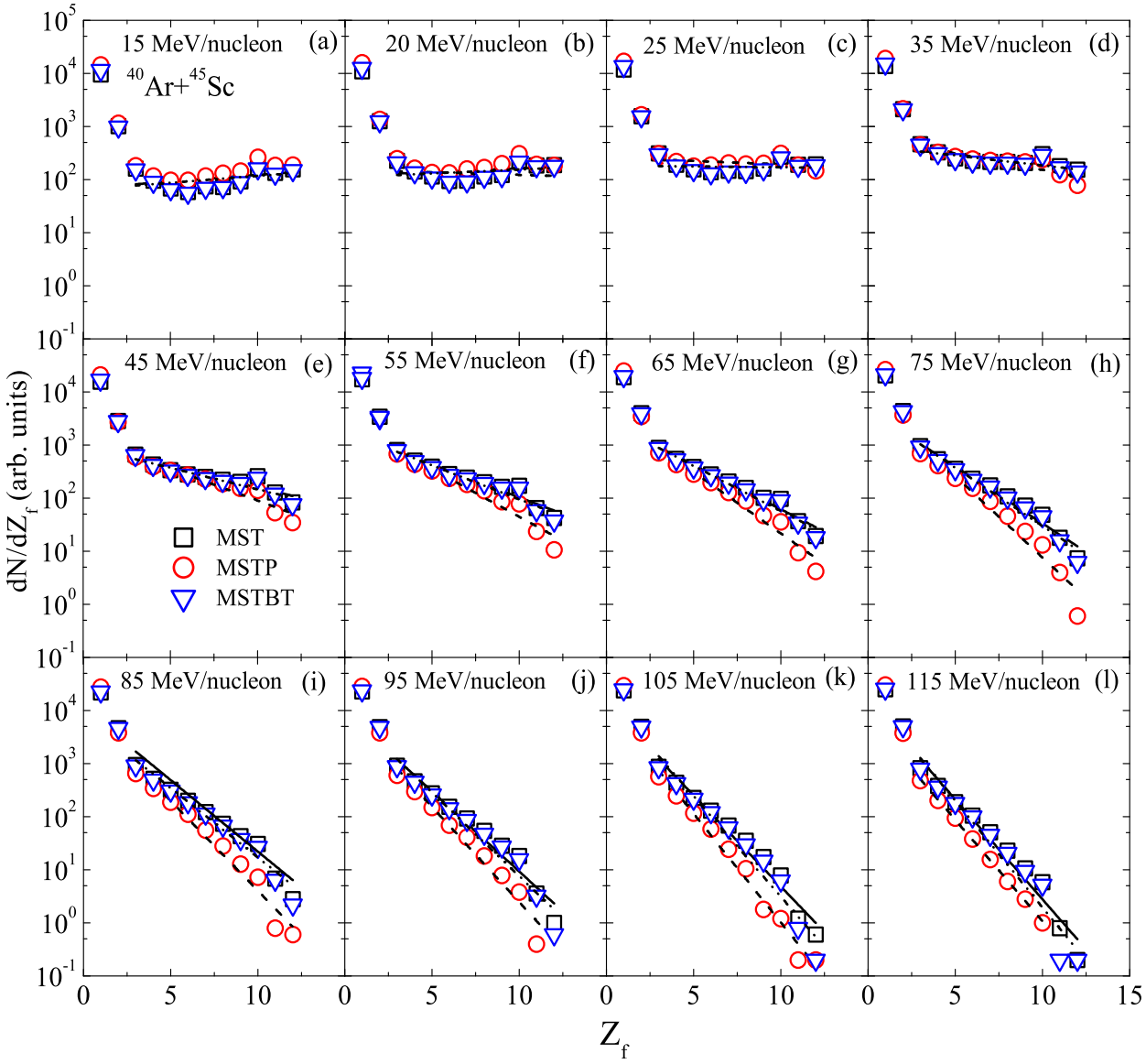

Figure 3.5: The charge distributions of central reactions of ^{40}Ar+^{45}Sc at different projectile incident energies in the range of 15 to 115 MeV/nucleon. The symbols have the same meaning as in Fig. 3.4. The lines are to guide the eyes and correspond to exponential - fit over fragment charge distributions for IMFs [$3 \leq Z_f \leq 12$].

cluster identifiers reach nearly the same conclusion. It clearly demonstrates that the effect of different cluster identifiers is nearly insignificant.

3.4.6 Different signatures to study liquid-gas phase transition

In a recent study, Lin *et al.* pointed that one should study various order parameters simultaneously to pin down the exact critical point [196]. Also the earlier studies showed that the occurrence of a minimum in $\tau(\lambda)$ is necessary but not a sufficient condition for the observation of phase-transition [45]. Campi suggested using the moments of the charge distribution to pin down the critical point [197]. In general, the i^{th} moment of the charge distribution having multiplicity 'n' can be defined as:

$$M_i = \sum_{Z_f \neq Z_{max}} Z_f^i \;\; n(Z_f). \tag{3.8}$$

Here, Z_f is the charge and $n(Z_f)$ is the multiplicity of the fragment with charge Z_f in an event. The values obtained are then averaged over all events except the heaviest fragment which indicates towards the property of bulk liquid in infinite system. In most of the studies, two particular combinations of these moments are used namely normalized second moment (S_2) and γ_2 [45, 109, 192, 193, 195]. These are defined as

$$S_2 = \frac{M_2}{M_1}, \tag{3.9}$$

and,

$$\gamma_2 = \frac{M_2 M_0}{{M_1}^2}, \tag{3.10}$$

where M_0, M_1, M_2 are the zeroth, first, and second moments of the charge distribution, respectively. In such an analysis, the parameters $<S_2>$ and $<\gamma_2>$ are expected to give maximal values at the critical point mimicking the largest fluctuations of the fragment charge distribution. Also due to the exclusion of largest cluster charge, one expects $<S_2>$ to be proportional to the isothermal compressibility [195]. In other studies, the charge of the second largest fragment ($<Z_{max2}>$) is also found to show a maximal value at the critical point when plotted as a function of the incident energy of the projectile [192]. We have also analyzed these parameters using various clusterization algorithms.

In Fig. 3.7, we display the values of the parameters $<S_2>$, $<\gamma_2>$, and $<Z_{max2}>$ as a function of incident energy using MST, MSTP, and MSTBT methods. The symbols have the same meaning as in Figs. 3.4 and 3.5. We see that all three parameters give

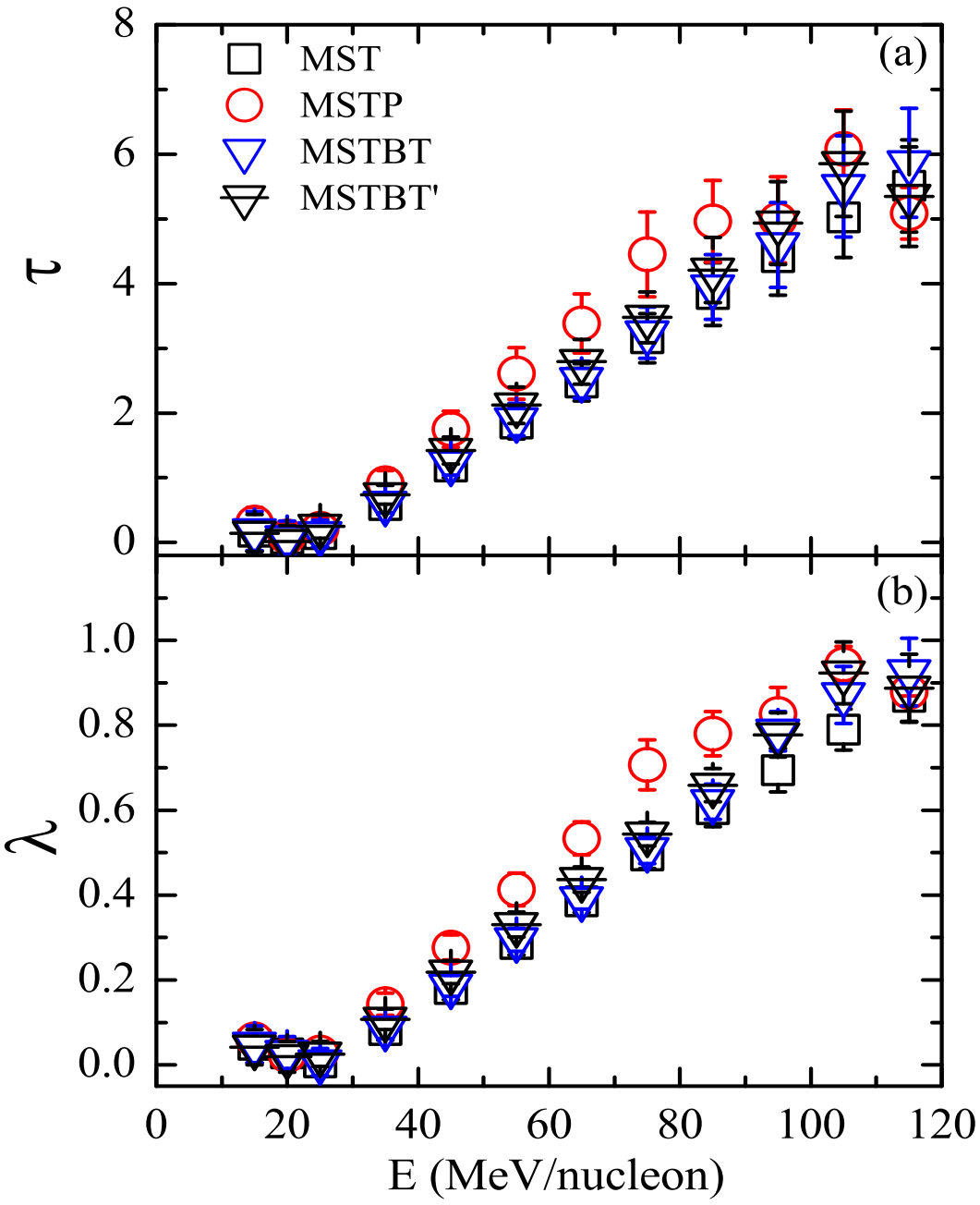

Figure 3.6: The extracted values of power-law parameter τ (using power-law fits [$Y(Z_f) \propto {Z_f}^{-\tau}$] and parameter λ (using exponential fits [$Y(Z_f) \propto e^{-\lambda Z_f}$] of IMFs as shown in Fig. 3.4) plotted as a function of incident energy. Different symbols carry the same meaning as in Fig. 3.4. The inverted lined triangles represent the results using MSTBT′ method.

almost the same results over the entire range of the incident energy. The effect of different clusterization algorithms is nearly insignificant.

The parameter $<S_2>$ shows a maximal value at 12 MeV/nucleon for the fragments identified using MST, MSTP, and MSTBT methods. Note that this predicted critical point is much lower than the expected or measured value due to the inclusion of classical heat capacity in-spite of the Fermionic one [217]. As pointed out in Ref. [217], the classical heat capacity is much larger than the Fermionic heat capacity, therefore, causing lesser production of IMFs and a larger Z_{max}. We also noted that the MST method gives highest value of $<S_2>$ due to maximum number of bound charge fragments.

Similarly, the parameters $<\gamma_2>$ and $<Z_{max2}>$ show maxima at 15 MeV/nucleon using MST, MSTP, and MSTBT algorithms. It is worth mentioning that we also checked the sensitivity of our results by varying the freeze-out time from 300 to 400 fm/c. The critical values of $\tau(\lambda)$ read as 19.04 (20.05), 17.01 (18.03), and 21.06 (22.07) for MST, MSTP, and MSTBT methods, respectively. In other words, the effect of different freezing time is about 5 - 10% only. The effect is of similar order as we obtain for different clusterization algorithms.

On the other hand, no effect of different freeze-out time is seen on the other transition parameters such as $<S_2>$, $<\gamma_2>$ and $<Z_{max2}>$. All these parameters remain completely insensitive towards both different clusterization algorithms as well as towards different freeze-out time (from 300 to 400 fm/c).

3.4.7 Effect of different thermal binding energies in clusterization algorithm

Now, we would like to draw the attention of the reader to the studies conducted by Souza *et al* [218] using statistical multifragmentation model (SMM) and Karthikraj *et al* [219] using dynamical cluster model (DCM). In both these studies, results were reported depending on the binding energy formulae one uses in the analysis codes. Souza *et al.* conducted their study using the SMM model to constraint the symmetry energy using an iso-scaling parameter based on the lighter fragments [218]. They took three liquid-drop-based binding energies, i.e., LDM1 [220], LDM2 [221], and LDM3 [222] to draw the breakup conditions for nuclei. The iso-scaling parameter and thus, the symmetry energy was found to vary significantly with the choice of the binding energy formula in their analysis program. A similar type of results were reported by Karthikraj *et al.* but

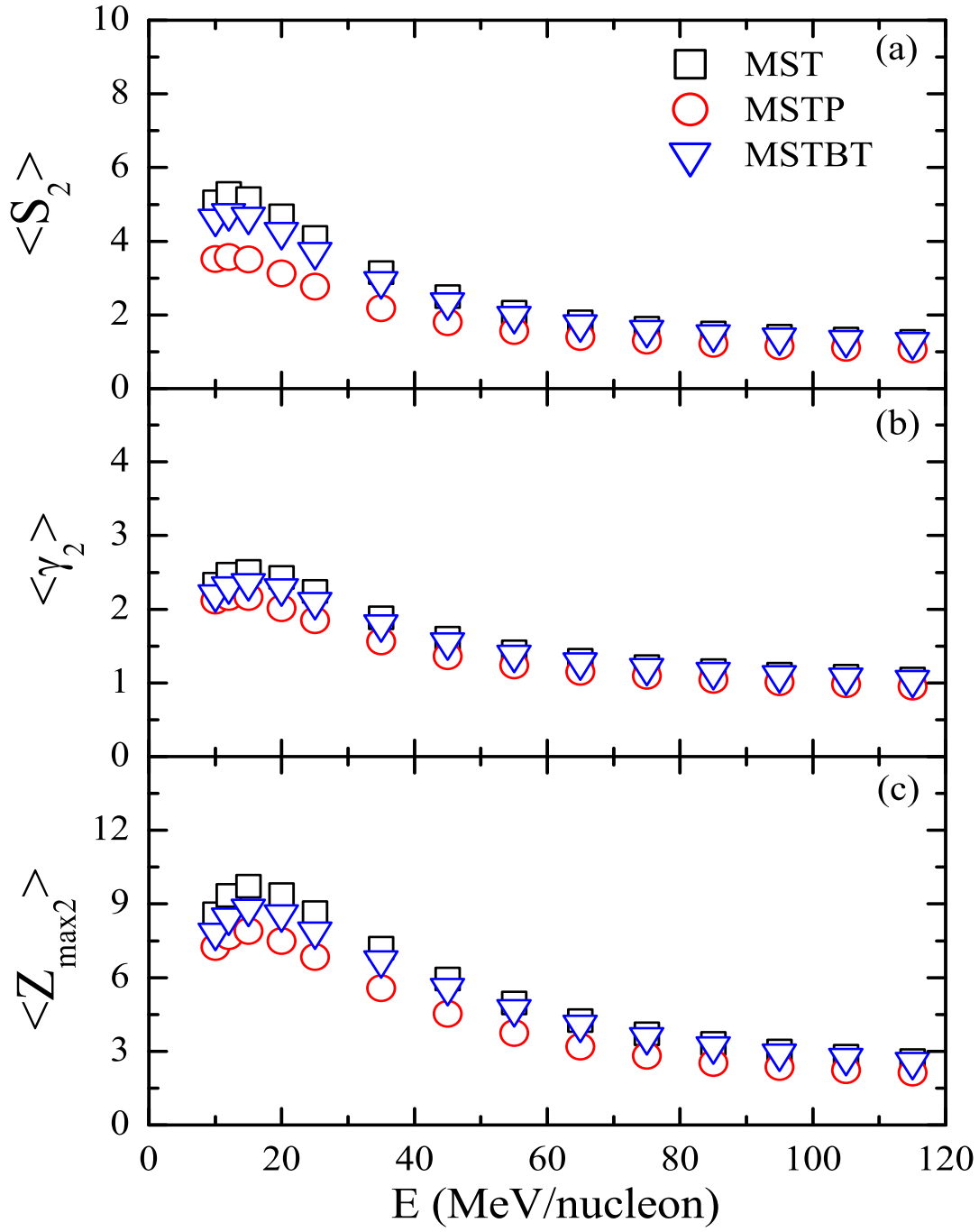

Figure 3.7: The critical parameters $<S_2>$, $<\gamma_2>$ and $<Z_{max2}>$ plotted as a function of the projectile incident energy using various clusterization algorithms. Symbols carry same meaning as in Fig. 3.4.

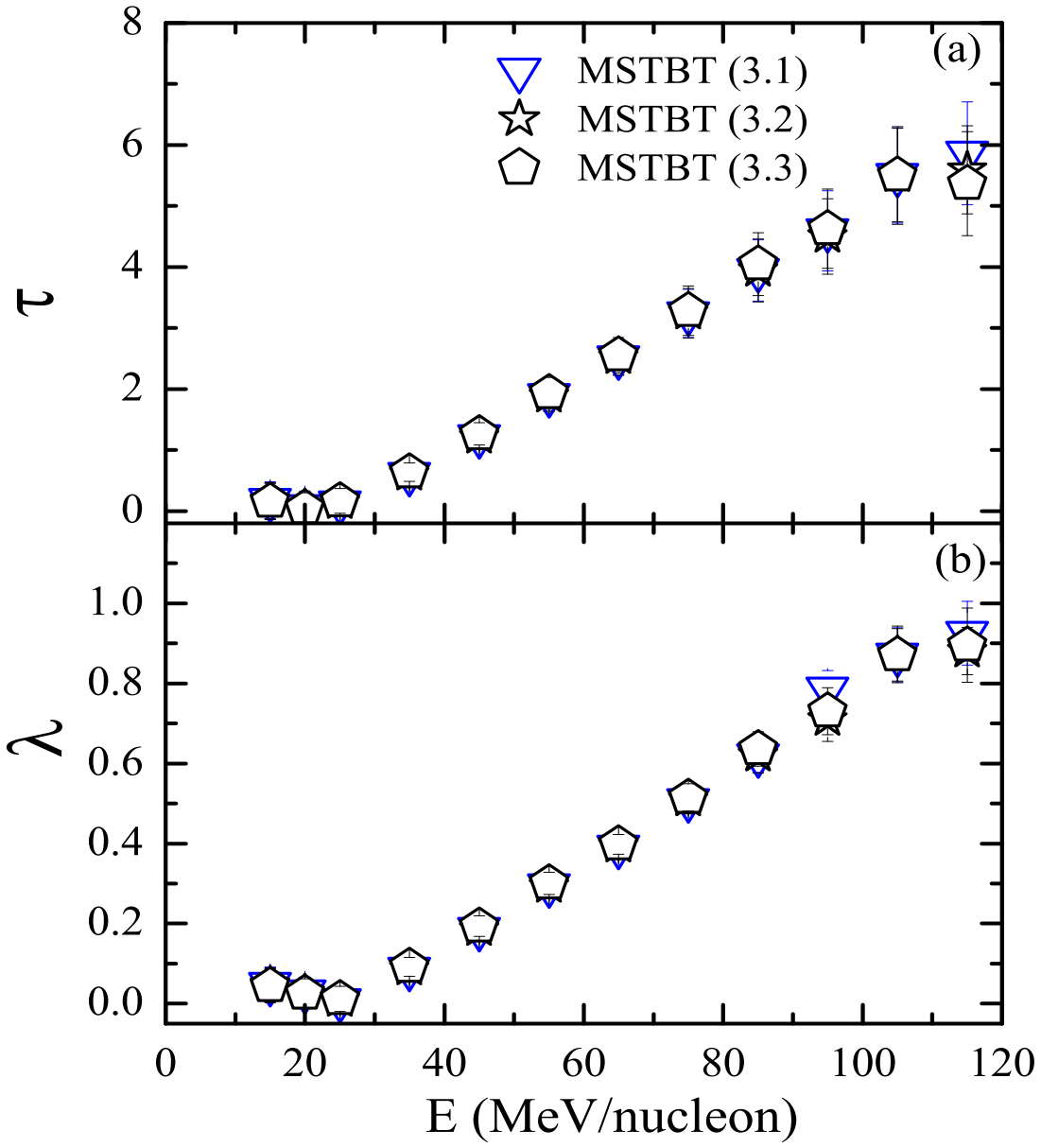

Figure 3.8: Same as Fig. 3.6, but for the different thermal binding energy formulae implemented in the clusterization algorithm. Symbols are explained in the text.

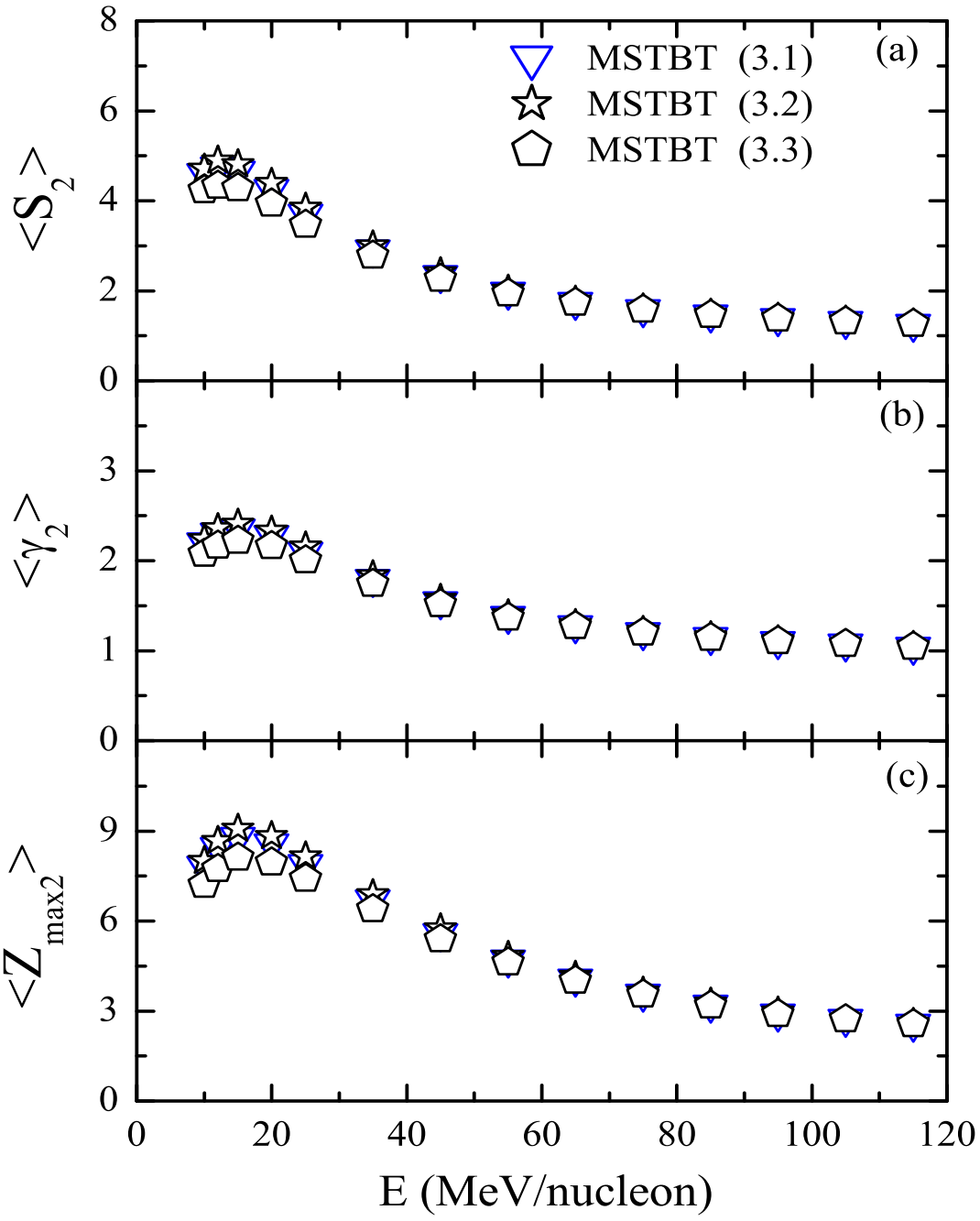

Figure 3.9: Same as Fig. 3.7, but using different thermal binding energy formulae implemented in the clusterization algorithm.

using different temperature-dependent binding energies in the DCM model to look for the α-structure of nuclei [219]. They studied the decay of $^{56}Ni^{*}$ compound nucleus formed in the reaction of $^{35}S+^{24}Mg$. The α-structure was found to depend significantly on the temperature-dependent binding energy one is using in analysis code.

Keeping the above studies in mind, we extended our work by using different thermal binding energy formulae (discussed in section 3). We used MSTBT (3.1), MSTBT (3.2), and MSTBT (3.3) methods for analyzing the stable fragment structures and finally critical parameters namely, τ, λ, $<S_2>$, $<\gamma_2>$, and $<Z_{max2}>$.

The results of τ and λ using different versions of MSTBT methods are plotted in Fig. 3.8, whereas Fig. 3.9 depicts the results for $<S_2>$, $<\gamma_2>$, and $<Z_{max2}>$ parameters. The inverted triangles, stars, and pentagons represent the results obtained using MSTBT (3.1), MSTBT (3.2), and MSTBT (3.3) methods, respectively. From Fig. 3.8, we observe minima in τ at 18.03, 17.02 and 17.72 MeV/nucleon for MSTBT (3.1), MSTBT (3.2), and MSTBT(3.3) methods, respectively. For λ, minima are obtained at 19.04, 20.05, and 19.04 MeV/nucleon for MSTBT (3.1), MSTBT (3.2), and MSTBT (3.3) methods, respectively.

All other parameters $<S_2>$, $<\gamma_2>$ and $<Z_{max2}>$ (see in Fig. 3.9) show the insignificant effect of different versions of the MSTBT method. Our these results are in agreement with previously reported results [157].

3.5 Summary

In this chapter, we investigated the connection between liquid-gas phase transition (or the onset of multifragmentation) and fragment charge yields for the central reactions of ^{40}Ar+^{45}Sc. In the present work, we have coupled various clusterization algorithms with the QMD model. Our detailed study in the chapter clearly indicates that different quantities advocated to study the phase transition namely the minimum in the critical parameter $\tau(\lambda)$ and maxima in $<S_2>$, $<\gamma_2>$ and $<Z_{max2}>$ give nearly consistent results. Further, all these results are nearly insensitive towards different clusterization algorithms, different freeze-out time, as well as towards different thermal binding energies formulae, therefore, present a universal behavior. Thus the order parameters used to find the critical point of phase transition is independent of the choice of algorithm one uses to find results.

Chapter 4

Fragment emission and critical behavior using energy based clusterization algorithm

In the previous chapter, we have used various extensions of Minimum Spanning Tree (MST) method (that include momentum and binding energy cuts) and found that there is no effect of these extensions on the extraction of liquid-gas phase transition signals [223]. It is very well known that the utility of MST method (or any of its extension) is constrained to dilute nuclear matter only where nucleon-nucleon collisions nearly cease. The MST method (or any of its variant) is quite accomplished to explain physics at the freeze-out stage (i.e., at $\sim$ 300 fm/c). In previous chapter using Quantum Molecular Dynamics (QMD) model, we could definitely obtain minimum in the exponent of charge yield for the reaction of ^{40}Ar+^{45}Sc and corresponding maxima in the values of $<S_2>$, $<\gamma_2>$, and $<Z_{max2}>$. The absolute values were, however, far from the experimental data. But to understand about the density fluctuations/correlations among nucleons that lead excited system to break into variable sized fragments; one requires clusterization algorithm that can trace back these initial correlations in the time (or identify fragment structures quite early in time i.e., when matter is in the violent or compressed state). In this direction, Puri and Aichelin proposed an algorithm namely Simulated Annealing Clusterization Algorithm (SACA) [159]. The idea of such algorithm was given by Dorso and Randrup for small systems [224]. This algorithm was found to resolve the issues that were reported with Minimum Spanning Tree (MST) method or any of its variants. In the last two decades, the utility of SACA method has been shown to resolve many misconceptions regarding dynamical models. For example, Tsang *et al* put forward a failure of QMD

+ MST method to reproduce the ^{197}Au + ^{197}Au data at relativistic energies of 250 and 400 MeV/nucleon for peripheral collisions [84]. They considered the use of classical heat capacity instead of Fermionic heat capacity in the dynamical model as the main reason for this failure. Later, Puri *et al* were successful in reproducing these experimental results using the same QMD model coupled with SACA method. They have also extended their study upto incident energies of 1000 MeV/nucleon to explain spectator fragmentation of ^{197}Au + ^{197}Au reactions. Earlier, thermal models were considered more suitable to explain experimental observations at these incident energies. In the last few years, the QMD + SACA model was also able to explain event-by-event correlations among fragments in the Fermi-energy domain for symmetric as well as asymmetric reactions [223]. This approach when coupled with Quantum Molecular Dynamics approach is also found to explain great set of experimental data on fragment multiplicities, bimodality, multiplicity distribution etc. Very recently, Aichelin and Fevre have shown success of QMD + Fragment Recognition in General application (FRIGA) model (modified version of SACA) to reproduce the isotopic yields [225]. Great efforts are done in order to extend the SACA method to the region of ultra-relativistic energies (upto LHC) to explain the production of hyper-clusters, related phenomena and Quark-Gluon Plasma (QGP) formation and hypernuclei production [226]. Our present aim is to workout the problem of studying liquid-gas phase transition (or onset of multifragmentation) with QMD model coupled with SACA method. We will use all the critical exponents explained in the earlier chapters. The motivation of the present study is to know whether our observations about liquid-gas phase transition are influenced if the energy based clusterization algorithm is used. If successful, one can consider the combination of QMD + SACA method as universally consistent method that can explain all the observations linked to multifragmentation.

4.1 Various energy based clusterization algorithms

4.1.1 Early Cluster Recognition Algorithm (ECRA)

Dorso *et al*, were the first to take initiative to develop an algorithm based on the metropolis procedure. This algorithm was named as Early Cluster Recognition Algorithm (ECRA) [158]. The emphasizing fact of this algorithm was that one could procure the most stable configuration at the early stage of the reaction (i.e., before freeze-out stage). In this algorithm the aim was on on maximizing the binding energy of each cluster, thus also used

the momentum space of nucleonic space. Despite the fact, the outcome of this algorithm was quite interesting but its utility was constrained due to the enhanced computing time and its compatibility to study lighter reactions only.

4.1.2 Simulated Annealing Clusterization Algorithm (SACA)

Based on the idea of energy minimization (as mentioned in ECRA), Puri *et al.* designed a unique clusterization technique "Simulated Annealing Clusterization Algorithm (SACA)" [159]. This algorithm removed all the shortcomings of the ECRA method. This algorithm is based on the similar ground as the "annealing" process used for the cooling of solids and widely used in metallurgy field. This algorithm is able to recognize the correlations among nucleons bound in fragments much ahead of their formal separation in coordinate space. In other words, SACA enables one to understand the reaction dynamics at the violent stages of a reaction. This algorithm not only identifies the realistic fragment structures but also realizes the fragment structure as early as $\sim$ 60 - 90 fm/c where state of matter is still dense and hot. This time is much shorter compared to the time needed by the standard MST method to provide the final fragment structures ($\sim$300 fm/c). Here, Monte-Carlo simulated annealing technique is evoked to search for the most bound configuration consisting of the fragments of different sizes and free nucleons. This algorithm constructs almost all possible fragment configurations using metropolis procedure [227] coupled with "simulated annealing" technique [228]. This algorithm is a sequence of metropolis steps with a control parameter ϑ interpreted as "temperature".

Further, it may happen that at intermediate times of a reaction too many clusters are recognized, which will break apart at later times. To avoid this and to fasten the procedure the pre-clusters formed at the intermediate stages are subjected to following binding energy condition:

$$\zeta = \sum_{i=1}^{A_f} \left[\sqrt{\left(\mathbf{p}_i - \mathbf{p}_{A_f}^{cm}\right)^2 + m_i^2} - m_i + \frac{1}{2}\sum_{j\neq i}^{A_f} V_{ij}(\mathbf{r}_i, \mathbf{r}_j) \right] < E_{bind} \times A_f, \tag{4.1}$$

with E_{bind} = - 4.0 MeV, if $A_f \geq 3$ and E_{bind} = 0 MeV, otherwise. This constant binding energy cut was changed to microscopic binding energy cut, where binding energy is calculated using the binding energy formula. But the effect on final fragment configuration has been seen to be insignificant. This condition assists to realize the fragments early,

despite the fact that if once loosely bound fragments are formed, it consumes longer time to search for the true configuration. Some steps regarding the procedure followed in the algorithm will be discussed in the upcoming paragraphs.

The procedure of the SACA method proceeds from any random configuration (e.g. using MST method) which is the basis to construct the new configuration. The acceptance of new configuration is based on the criteria that it yields maximum number of stable configurations. This algorithm ameliorates a better picture, by avoiding the trapping of configuration in the local minima that was major problem in using ECRA method. The simulated annealing technique also inherits the feature to accept even the rejected configuration in the controlled manner. The paradigm of obtaining most bound configuration through SACA method follows the chain of metropolis steps with a controlled parameter 'ϑ' which is termed as temperature. It is important to notice here that unlike Restructured Aggregation Method (RAM) [229], the SACA method does not alter the nucleonic phase space. The steps for SACA algorithm reads as:

1. One begins from any random configuration 'ψ'' having energy $\zeta_{\psi'}$. From which a new fragment configuration 'ϕ'' with energy $\zeta_{\phi'}$ is generated using Monte-Carlo procedure. This is done by shifting one or few nucleons from one fragment to other fragment.

2. The energy difference between the old and new fragment configuration is calculated i.e., $\triangle\zeta = \zeta_{\phi'} - \zeta_{\psi'}$.

3. If energy difference between two configurations ($\Delta\zeta$) is negative, the new configuration is always accepted. On the other hand, if $\Delta\zeta$ is positive, the new configuration is still accepted with a probability $\exp(-\Delta\zeta/\vartheta)$ to avoid any local minima.

Let initial configuration 'ψ'' consists of randomly and artificially created fragments and free nucleons be 'ψ''. The total energy ($\zeta_{\psi'}$) associated with this configuration is then calculated as:

$$\zeta_{\psi'} = \sum_{i=1}^{A_f^{l_1}} \left[\sqrt{\left(\mathbf{p}_i - \mathbf{P}^{cm}_{A_f^{l_1}}\right)^2 + m_i^2} - m_i + \frac{1}{2}\sum_{j\neq i}^{A_f^{l_1}} V_{ij}(\mathbf{r}_i, \mathbf{r}_j) \right]_{l_1}$$
$$+.... + \sum_{i=1}^{A_f^{l_2}} \left[\sqrt{\left(\mathbf{p}_i - \mathbf{P}^{cm}_{A_f^{l_2}}\right)^2 + m_i^2} - m_i + \frac{1}{2}\sum_{j\neq i}^{A_f^{l_2}} V_{ij}(\mathbf{r}_i, \mathbf{r}_j) \right]_{l_2}$$

$$+\sum_{i=1}^{A_f^{l_3}}\left[\sqrt{\left(\mathbf{p}_i-\mathbf{P}^{cm}_{A_f^{l_3}}\right)^2+m_i^2}-m_i+\frac{1}{2}\sum_{j\neq i}^{A_f^{l_3}}V_{ij}(\mathbf{r}_i,\mathbf{r}_j)\right]_{l_3}$$
$$+.....\sum_{i=1}^{A_f^{l_n}}\left[\sqrt{\left(\mathbf{p}_i-\mathbf{P}^{cm}_{A_f^{l_n}}\right)^2+m_i^2}-m_i+\frac{1}{2}\sum_{j\neq i}^{A_f^{l_n}}V_{ij}(\mathbf{r}_i,\mathbf{r}_j)\right]_{l_n}. \quad (4.2)$$

Here, $\mathrm{A}_f^{l_1}$ represents the number of nucleons in the cluster 'l_1', $\mathbf{P}^{cm}_{A_f^{l_1}}$ is the momentum of the cluster 'l_1' in its center-of mass frame. Note here, the interaction between nucleons of the different clusters in not considered, therefore $\zeta_{\psi'}$ calculated in the above equation differs from the total energy of the system. Now, new fragment configuration is generated using Monte-Carlo method by choosing one of the following possibilities:

- transferring a single nucleon from one fragment to other fragment, or
- setting a single nucleon free from a fragment, or
- absorbing a single nucleon by the fragment.

To understand the SACA method, let the new configuration 'ϕ'' is generated by transferring a single nucleon from fragment l_3 to l_2. The energy associated with new configuration 'ϕ'' reads as:

$$\zeta_{\phi'}=\sum_{i=1}^{A_f^{l_1}}\left[\sqrt{\left(\mathbf{p}_i-\mathbf{P}^{cm}_{A_f^{l_1}}\right)^2+m_i^2}-m_i+\frac{1}{2}\sum_{j\neq i}^{A_f^{l_1}}V_{ij}(\mathbf{r}_i,\mathbf{r}_j)\right]_{l_1}$$
$$+....+\sum_{i=1}^{A_f^{l_2}+1}\left[\sqrt{\left(\mathbf{p}_i-\mathbf{P}^{cm}_{A_f^{l_2}+1}\right)^2+m_i^2}-m_i+\frac{1}{2}\sum_{j\neq i}^{A_f^{l_2}+1}V_{ij}(\mathbf{r}_i,\mathbf{r}_j)\right]_{l_2}$$
$$+\sum_{i=1}^{A_f^{l_3}-1}\left[\sqrt{\left(\mathbf{p}_i-\mathbf{P}^{cm}_{A_f^{l_3}-1}\right)^2+m_i^2}-m_i+\frac{1}{2}\sum_{j\neq i}^{A_f^{l_3}-1}V_{ij}(\mathbf{r}_i,\mathbf{r}_j)\right]_{l_3}$$
$$+.....\sum_{i=1}^{A_f^{l_n}}\left[\sqrt{\left(\mathbf{p}_i-\mathbf{P}^{cm}_{A_f^{l_n}}\right)^2+m_i^2}-m_i+\frac{1}{2}\sum_{j\neq i}^{A_f^{l_n}}V_{ij}(\mathbf{r}_i,\mathbf{r}_j)\right]_{l_n}. \quad (4.3)$$

During this procedure, the energy of all fragments except the donor (l_3) and acceptor (l_2) fragment remains constant. The energy difference between the old (ψ') and new (ϕ')

configuration then can be calculated as:

$$\Delta\zeta = \zeta_{\phi'} - \zeta_{\psi'}. \tag{4.4}$$

If the energy difference between two configurations ($\Delta\zeta$) is negative, the new configuration is always accepted. On the other hand, if ($\Delta\zeta$) is positive, the new configuration is accepted with a probability $e^{-\frac{\Delta\zeta}{\vartheta}}$ to avoid any local minima, where 'ϑ' is the control parameter in metropolis algorithm. Initially, a large value of 'ϑ' is taken. This is done to overcome any kind of local minima. At a given temperature, a sequence of steps is performed until cluster configuration freezes in binding energy. Then the control parameter 'ϑ' decreases to construct a new cluster configuration. The same procedure is repeated by exchanging two nucleons, three nucleons and so on. In between the metropolis procedure, the control parameter 'ϑ' is decreased to cool down the system. A decrease in control parameter 'ϑ' means that the accepted energy difference in metropolis step is narrowed. After a large number of metropolis steps, one would be able to realize the most stable configuration in nature. The SACA algorithm has number of control parameters that can change the time taken to realize the fragment configuration.

In the second step, the above mentioned procedure is repeated via shifting two nucleons at one time. Further steps include shifting three, four and larger number of nucleons. In the last step, the above procedure is evoked by allowing exchange of entire fragment (instead of individual nucleons). The detailed description of the procedure such as mathematical modelling, effect of input parameters, optimization input parameters of the model are given in Ref. [159].

To show the reliability of the SACA computer code, we apply this algorithm to single nuclei whose ground state properties are well known to us. We take two nuclei for the reference purpose i.e., ^{40}Ca and ^{208}Pb. We divide ^{40}Ca into 5 and ^{208}Pb into 10 random clusters of any size. If SACA finds the most bound configuration, then it must return us these random configurations as single ^{40}Ca and ^{208}Pb nuclei. In the Fig. 4.1, we show the evolution of the multiplicity (upper panels) and binding energy of the nuclei/clusters (lower panels) as a function of the iterations for the single nuclei of ^{40}Ca (left panel) and ^{208}Pb (right panels) [159]. Initially, we see multiplicity of clusters to be five for ^{40}Ca and 10 for ^{208}Pb. These random clusters are unstable and can also be observed by looking at lower panels, where binding energy of the clusters is shown. Starting from these random configurations, SACA construct other possible configurations and try to minimize the

binding energy of the system. It takes nearly few thousand iterations to find the final configuration. One can observe that SACA computer modelling gives multiplicity value of 1 at the end, which means SACA finds that the most stable cluster configuration is a single nucleus i.e., ^{40}Ca and ^{208}Pb in the present case. These configurations are stable and can also be observed from the binding energy values, which are negative and almost equal to actual binding energies of these nuclei. These results confirm the reliability of the SACA code in identifying the realistic clusters.

4.1.3 Fragment Recognition in General application (FRIGA) model

It is worth mentioning here that recently SACA algorithm was extended to study the hypernuclei production in heavy-ion reactions [226], namely Fragment Recognition in General application (FRIGA) model. To obtain more realistic fragments, this approach was extended by incorporating isospin degree of freedom in the framework through the potential terms (i.e., asymmetry energy and shell effects). Recently, the consistency of this algorithm in the reproduction of experimental data at the ultra-relativistic energies and production of hyper-nuclei was presented in Ref. [225, 226]. The results further strengthen the applicability of the procedure to construct fragments/clusters in the adopted algorithm. As the extended SACA is all set to explore the physics related to Quark-Gluon Plasma (QGP) at ultra-relativistic energies of Super Proton Synchrotron (SPS), Relativistic Heavy Ion Collider (RHIC), and Large Hadron Collider (LHC), the present chapter will be dedicated to understand the utility of SACA method to understand liquid-gas phase transition in multifragmentation at intermediate energy domain. In the following, we will briefly discuss Michigan State University (MSU) set up whose results we have compared in this chapter.

4.2 The Michigan State University (MSU) 4π array

The diverse range of experimental facilities have been developed so far and many are under development. The outcome of performed experiments have been quite consistent in providing many facets of the dynamics related to multifragmentation over broad variety of colliding partners of different masses, incident energies, colliding geometries, isospin contents, etc. Out of various existed research facilities and groups, the major groups involved

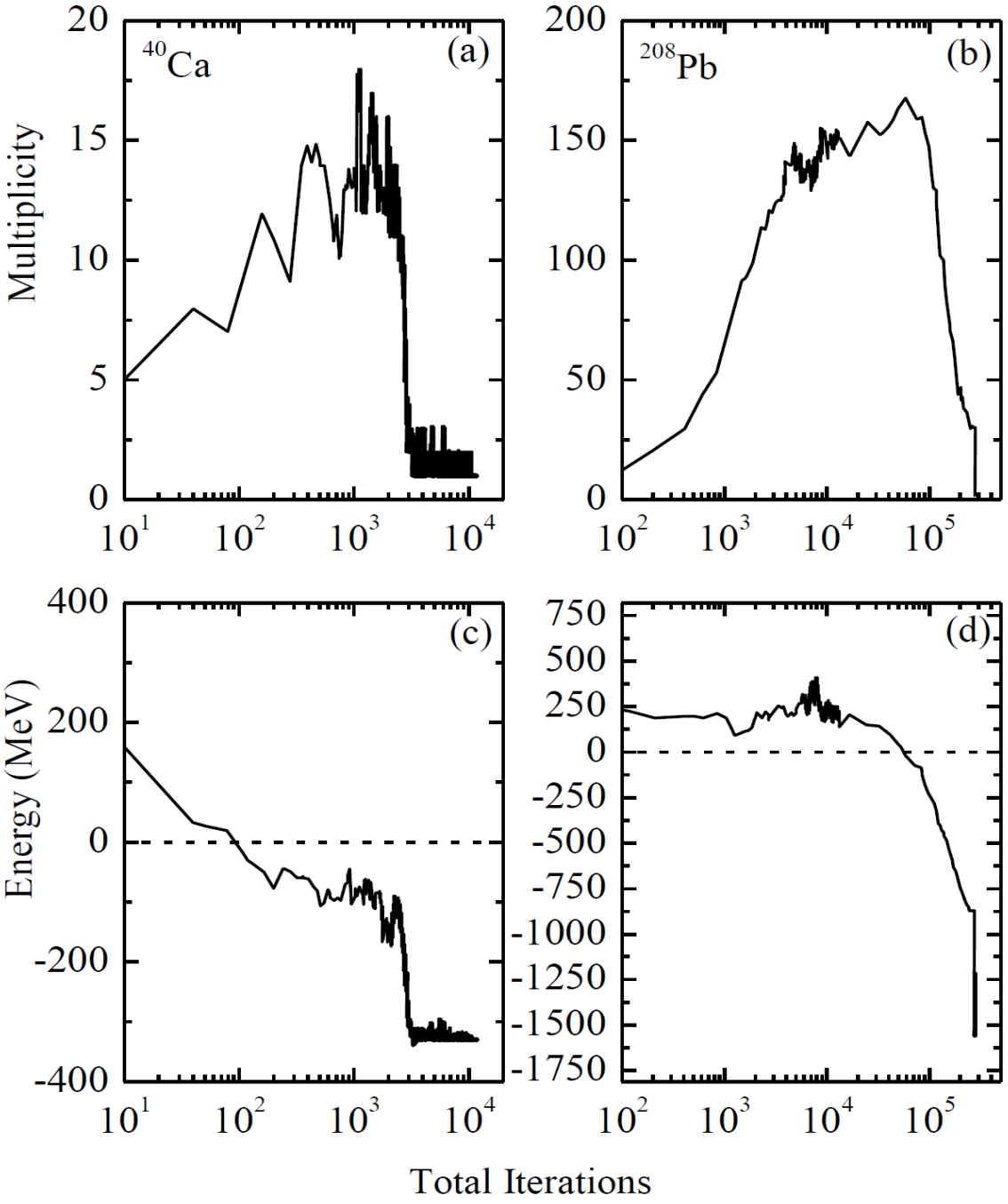

Figure 4.1: (Upper panels) The evolution of single nuclei ^{40}Ca and ^{208}Pb as the function of iterations, respectively. (Lower panels) Same as upper panels, but here we display the energy of the system as the function of the iterations. " Reprinted (Fig. 1) with permission from R. K. Puri and J. Aichelin, Journal of Computational Physics **162**, 245-266 (2000), Copyright (2000) by the Elsevier".

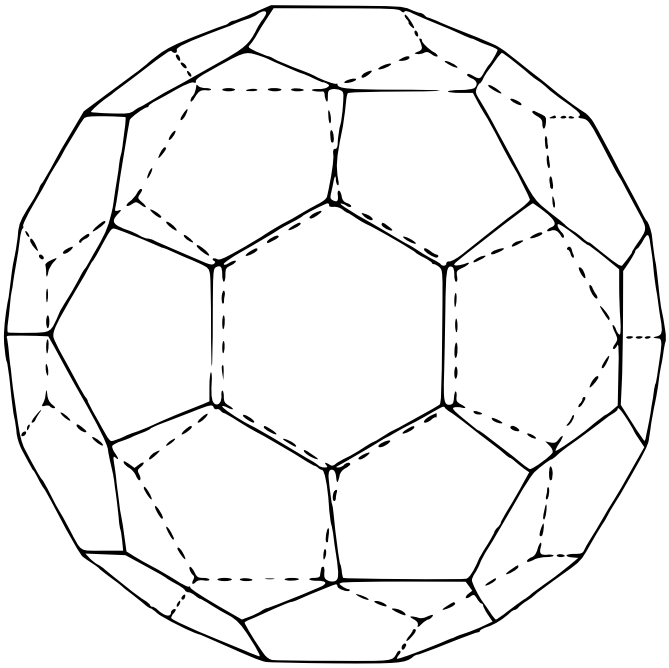

Figure 4.2: A thirty-two face truncated icosahedron, comprising of twenty hexagons and twelve pentagons. " Reprinted (Fig. 1) with permission from G. D. Westfall *et al.,* Nuclear Instruments and Methods in Physics Research A **238**, 347-353 (1985), Copyright (1985) by the Elsevier."

in the study of phenomenon of multifragmentation are FOur PI (FOPI) at GSI Germany, 4π multidetector Identification de Noyaux et Detection avec Resolution Array (INDRA) group at GANIL, Caen, France, *A Large Acceptance Di*pole mag*N*et (ALADiN) at GSI, Germany and 4π array of Michigan State University (MSU), Michigan, USA. Various detectors have been developed to accurately detect particles from heavy-ion collisions. For the simultaneous detection of variety of charged particles i.e., from pions to fission fragments, one needs a detector with the wide dynamic range. The aim was to construct an apparatus that can achieve almost complete 4π coverage and hold within a large dynamic range. In this chapter, we will compare our calculations with the experimental data from MSU 4π detector, therefore, we will present a few details of the set up [230].

4.2.1 Details of the experimental set up

The low-pressure Multi-Wire Proportional Counter (MWPC) forms the inner layer and detect fission fragments and various other slow, heavy, highly ionizing particles close to Coulomb barrier energies. The MWPC measures position sensitivity and provides information of the time of these particles. The Braggs Curve Counter (BCC) is constructed to

detect high energy particles which acts as a thick second layer. The charge Z_f and total energy of the fragments are also measured by the BCC counter. After the penetration of particles when they pass through both Multi-Wire Proportional Counter (MWPC) and Braggs Curve Counter (BCC); these particles can be analyzed in the scintillator telescope. The scintillator telescope provides information about the ΔE and E for light particles such as pions, protons and alpha particles. These telescopes can also be used to give timing information for the random-coincidence suppression and pion identification. Further, the photomultiplier tube is assembled to read these signals. At the output, the CaF_2 (slow) and plastic scintillator (fast) owing to the difference in the characteristic time are assembled. These signals are further separated by implementing different time gates. The shape of the detector is constrained as it is made of number of components (MWPCs, BCCs and scintillator telescopes), in order to achieve the objective of maximum coverage by 4π detector. The configuration of the detector is selected on the basis of thirty-two face truncated icosahedron comprising twenty regular hexagonal faces and twelve regular pentagonal faces in the configuration. For better understanding, the geometrical example figure of icosahedron is displayed in Fig. 4.2, that encloses hidden lines which are represented by dashed lines. The schematic view of a typical example of the truncated hexagonal detector is depicted in Fig. 4.3. Here, it is important to note that for the complete coverage of 4π solid angle, the detector must have maximum sensitive area to detect maximum count of particles and walls should have a small cross-section in comparison to the sensitive area. The structure of the detector is built in such a manner that the center lines of the walls are along the radii of a sphere centered at the target [230].

The Multi-Wire Proportional Counter (MWPC)

It is the low pressure gas detector that makes use of double amplification method. These detectors can be utilized as initial detectors for the heavy fragments with slow mobility alike fission fragments. The better and larger version of MWPC has been introduced and they are made more position sensitive by diving the cathode foil into strips. Since, the utility of this method needs the delay line outside the detector lines therefore, making it inappropriate for close packing structures. Accordingly, the strips on the cathode foil are connected with NiCr strips. The charge division method is employed to calculate the position signal.

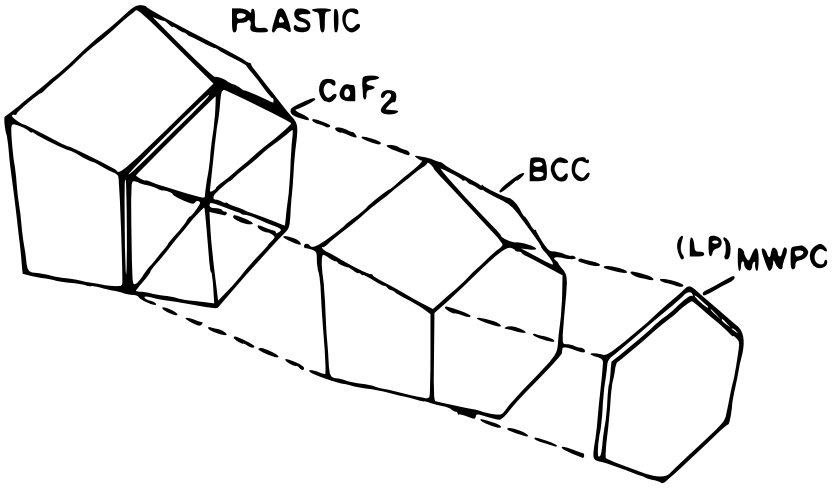

Figure 4.3: The illustrated representation of one of the thirty subarrays that construct the multiparticle array. " Reprinted (Fig. 2) with permission from G. D. Westfall *et al.,* Nuclear Instruments and Methods in Physics Research A **238**, 347-353 (1985), Copyright (1985) by the Elsevier".

The Braggs Curve Counter (BCC)

It is designed as an ionization chamber in the detector with its field aligned in the direction of incoming particles. In the similar manner, the range of the stopped particles in the detector can also be computed. This counter is based on the principle that the maximum specific ionization of the stopping ion is proportional to atomic number of the particle. The maximum value of the ionization is used to compute the charge Z_f; the integral of the ionization is also used to calculate energy E.

The ionization of a stopping particle leads to production of electrons that drift towards anode that is further shielded by Frisch Grid. One can compute charge as a function of time gathered around the anode, due to alignment of electric field in the same direction of the path of the particle and therefore, also calculate the complete energy loss of the distribution. In the existing counter, the range of covered area through angles is very large and subsequently, the data corresponding to the stopping particles will be lost if the electrons do not align themselves along the path of the particle. Therefore, the field shaping grid is assembled in the BCC to provide the radial field. The pictorial representation of BCC is shown in Fig. 4.4. The basic shape of BCC is hexagonal pyramid. It comprises of small diameter entrance window, pressure window made of aluminized mylar, Frisch grid composed of gold plated tungsten wires and anode behind the Frisch

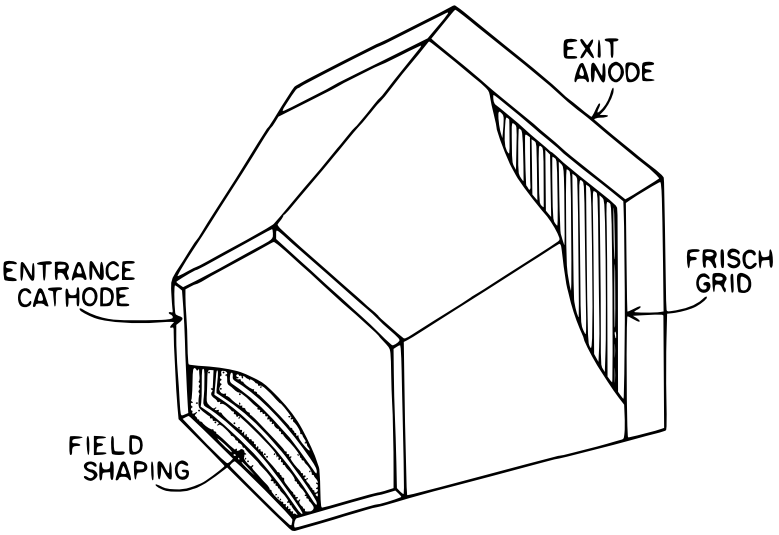

Figure 4.4: The enlarged view of Bragg Curve Counter. " Reprinted (Fig. 4) with permission from G. D. Westfall *et al.,* Nuclear Instruments and Methods in Physics Research A **238**, 347-353 (1985), Copyright (1985) by the Elsevier".

grid. The rear pressure window is made by using scintillator telescopes. Therefore, the BCC can operate at a pressure of 500 Torr.

The Scintillator telescopes

These telescopes are built to detect light particles from pions to alpha particles. The "Phoswich" technique is followed to calculate E and ΔE for identification of particles and energy measurement. This technique is based on the utilization of time constants from CaF_2 and plastic scintillators. The characteristic time for CaF_2 (1μs) is greater than for plastic scintillator (50ns). Therefore, the energy loss from the CaF_2 can be measured by imposing the long, delayed gate at the output of the phototube, on the other side the energy collected in the plastic scintillator can be attained using a short gate.

The structure of a scintillator counter supports this method of producing light by CaF_2 that possess better collection efficiency than the plastic scintillator. The number of scintillator telescopes are connected through lightguides to the photo-multipliers.

4.3 Results and discussions

For the present study, several thousand events of the reactions of ^{40}Ar+^{45}Sc and ^{84}Kr+^{197}Au were generated, at different beam energies (ranging between 15 and 400

MeV/nucleon). The choice of various entrance channels for the reactions (e.g., incident energies and colliding geometries) is guided by the experimental measurements available in the literature [46, 49]. Here, soft equation of state supplemented by Cugnon parametrization of the nucleon-nucleon (NN) cross-section is used to simulate the above reactions. It is worth mentioning that above choice of the equation of state and NN cross-section has been very successful in explaining various experimental results [51, 157, 159, 231, 232].

In Fig. 4.5, we display the normalized charge yields (see crossed squares) calculated using the QMD model coupled with SACA method for the central collisions of ^{40}Ar+^{45}Sc at different incident energies between 15 and 115 MeV/nucleon. The choice of the centrality and incident energy range is guided by experimental measurements reported in Ref. [46]. Along with calculated yields, we also show the available experimental data (see stars) [46]. From the figure, we notice that the slope of the charge yield becomes steeper with incident energy signifying the violence of the binary collisions. These results (obtained with QMD + SACA) are consistent with experimental trends and calculations reported in earlier studies [43, 44, 46, 49, 59, 87, 212, 213, 233]. Very encouragingly, the QMD + SACA can reproduce the measured charge yields at all incident energies very closely. It is worth mentioning that the charge distributions are often fitted with power-law $\propto Z_f^{-\tau}$ to investigate the critical energy point of the possible liquid-gas phase transition. Hence, we also fit the calculated charge yields [$3 \leq Z_f \leq 12$] with power-law $\propto Z_f^{-\tau}$ (shown in Fig. 4.5).

The extracted values of τ are plotted in Fig. 4.6. From the figure, it is clear that the values of τ increases with beam energy (>20 MeV/nucleon) reflecting the steepening of the slope of the charge distribution with incident energy. We also observe a minimum in the extracted "τ" value when plotted against incident energy. This minimum in the value of the power-law factor "τ" corresponds to the onset of multifragmentation or sometimes has also been referred as critical energy point. To obtain the exact value of the onset of multifragmentation or minimum in the τ, we fitted extracted values of τ with fourth order polynomial fit as was done in previous experimental analysis [46, 87, 212, 213] and obtained a minimum in the τ at 20.1 MeV/nucleon. Very interestingly, our present prediction about the minimum value for the light charged system of ^{40}Ar+^{45}Sc is in a close agreement with the measured one (23.9 MeV/nucleon) [46]. This is the closest value ever reported in the literature so far by any theoretical model. On the other hand, QMD + MST predicted the minimum value to occur at 18.03 MeV/nucleon and values of τ were nowhere close to experimental values [215, 223]. Also, the Percolation model calculations predicted the

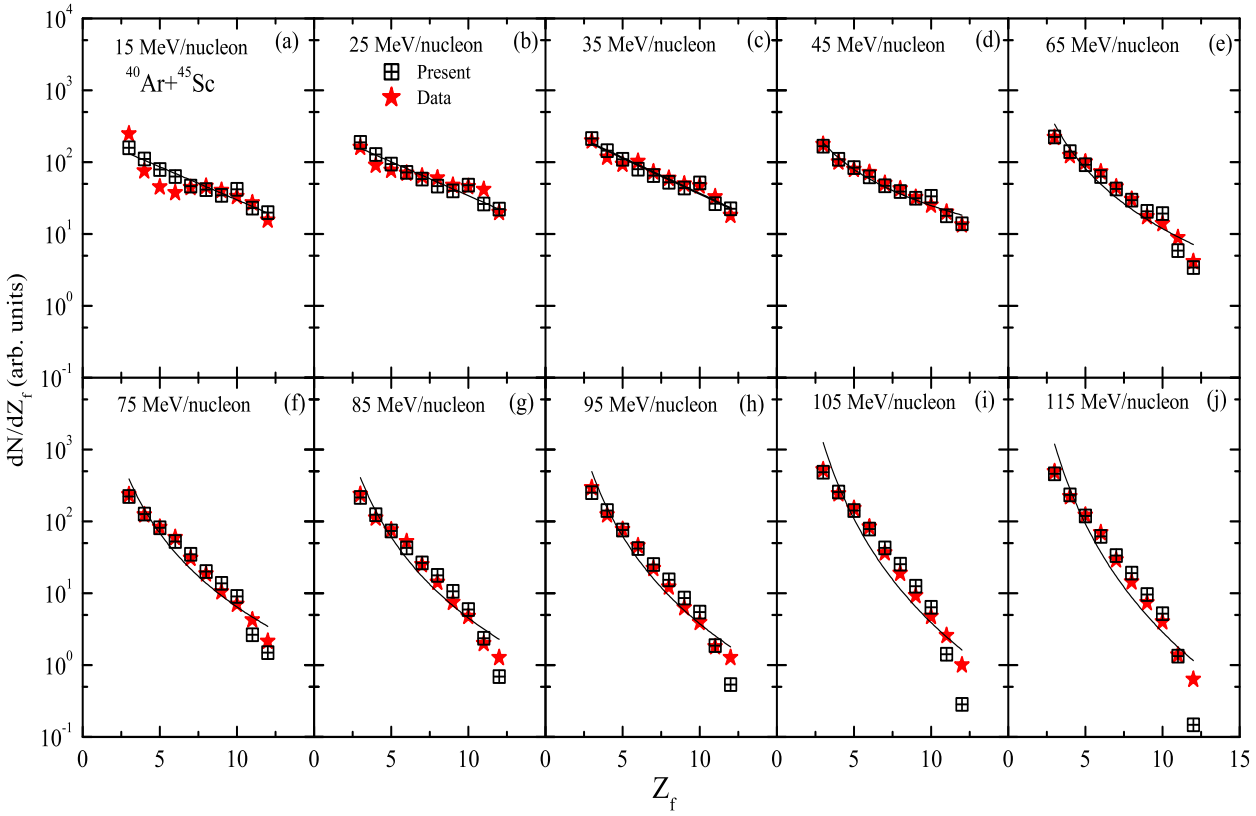

Figure 4.5: The normalized charge distributions obtained in the central reactions of ^{40}Ar+^{45}Sc at beam energies between 15 and 115 MeV/nucleon. The crossed squares show the calculated results of QMD + SACA method whereas, stars represent the experimental data [46]. The solid lines correspond to power law fits of fragment charge distributions for IMFs [$3 \leq Z_f \leq 12$] using QMD + SACA model.

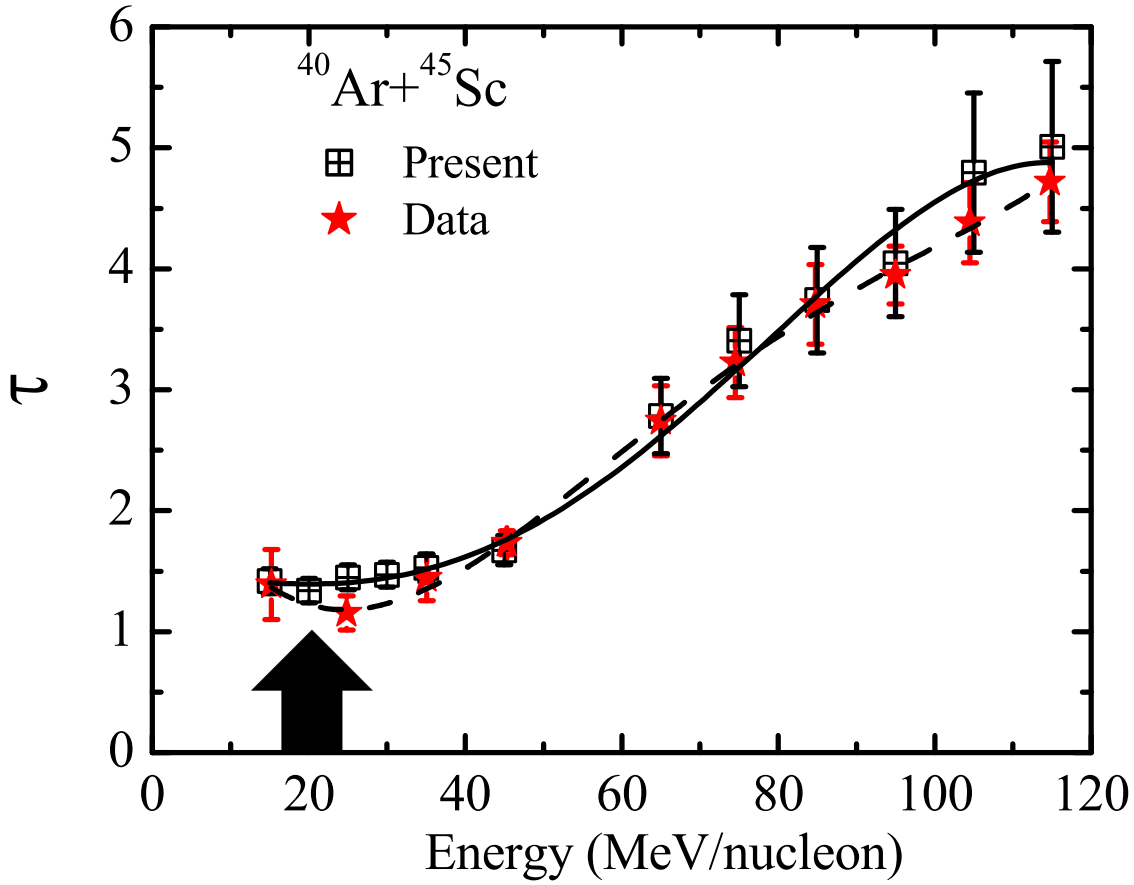

Figure 4.6: The extracted values of power-law parameter τ, (obtained from the power-law fits $\propto {Z_f}^{-\tau}$ of IMFs as shown in Fig. 4.5.) plotted as a function of incident energy. The solid and dashed lines correspond to fourth order polynomial fits over extracted τ values obtained using QMD + SACA and experimentally predicted τ values, respectively. Solid arrow represents the minimum in the extracted τ values for QMD + SACA calculations. Symbols have same meaning as in Fig. 4.5.

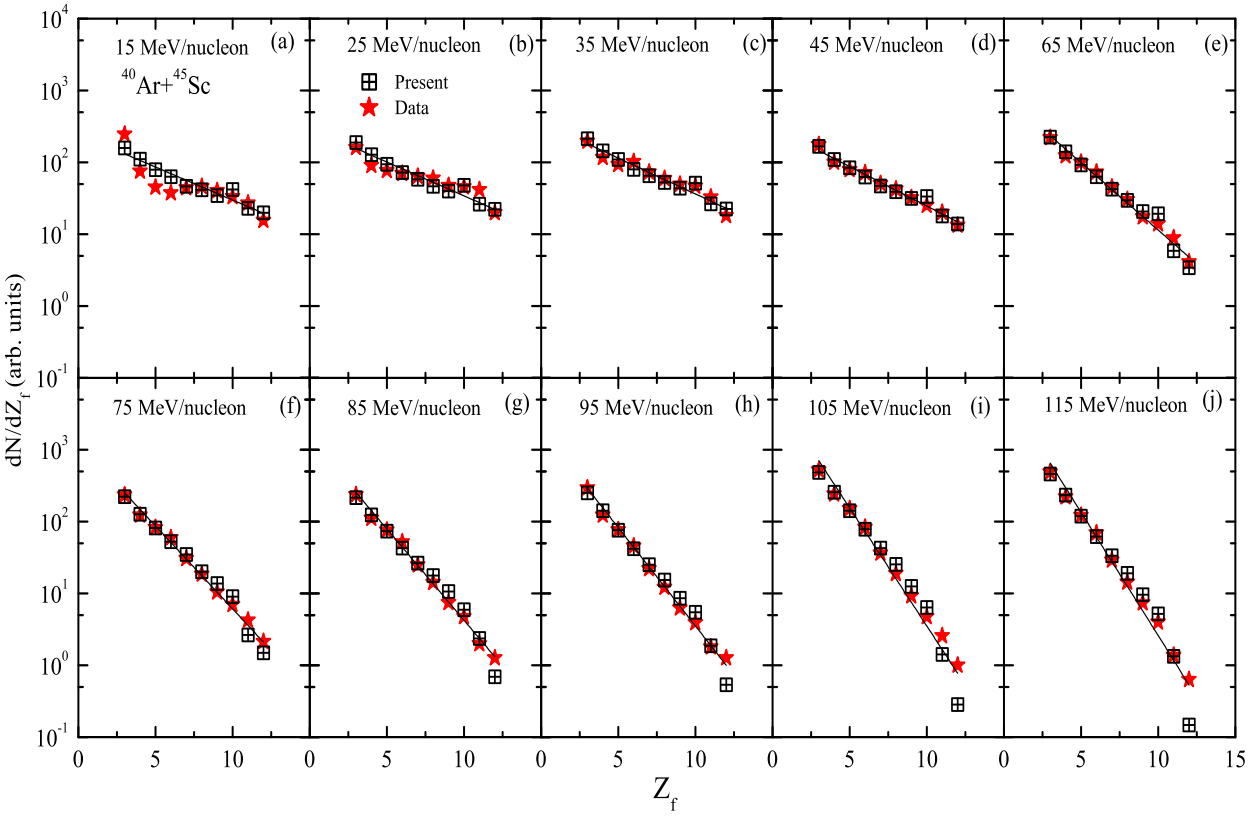

Figure 4.7: Same as Fig. 4.5, but here solid lines represent exponential fits $\propto e^{-\lambda Z_f}$ over fragment charge distribution of IMFs obtained using QMD + SACA model.

energy of critical point much higher than experimental data (28 MeV/nucleon) [46]. Thus, the QMD + SACA calculations not only reproduced the measured charge yields but also explained the behavior of power-law factor "τ" over the entire energy range nicely.

Next, to check the accuracy of our predicted minimum or onset of fragmentation (obtained with power-law fits $\propto Z_f^{-\tau}$), we also fitted the above calculated yields (Fig. 4.5) with exponential fit of the form $\propto e^{-\lambda Z_f}$ (see Fig. 4.7) and plotted the extracted λ values in Fig. 4.8.

Very interestingly, once again QMD + SACA method found a minimum in the extracted λ value. The exact minimum is extracted by fitting the λ values with fourth order polynomial fit. The minimum value obtained at 23.1 MeV/nucleon is very close to the one obtained using power-law fit (= 20.1 MeV/nucleon) and experimental values (= 23.9

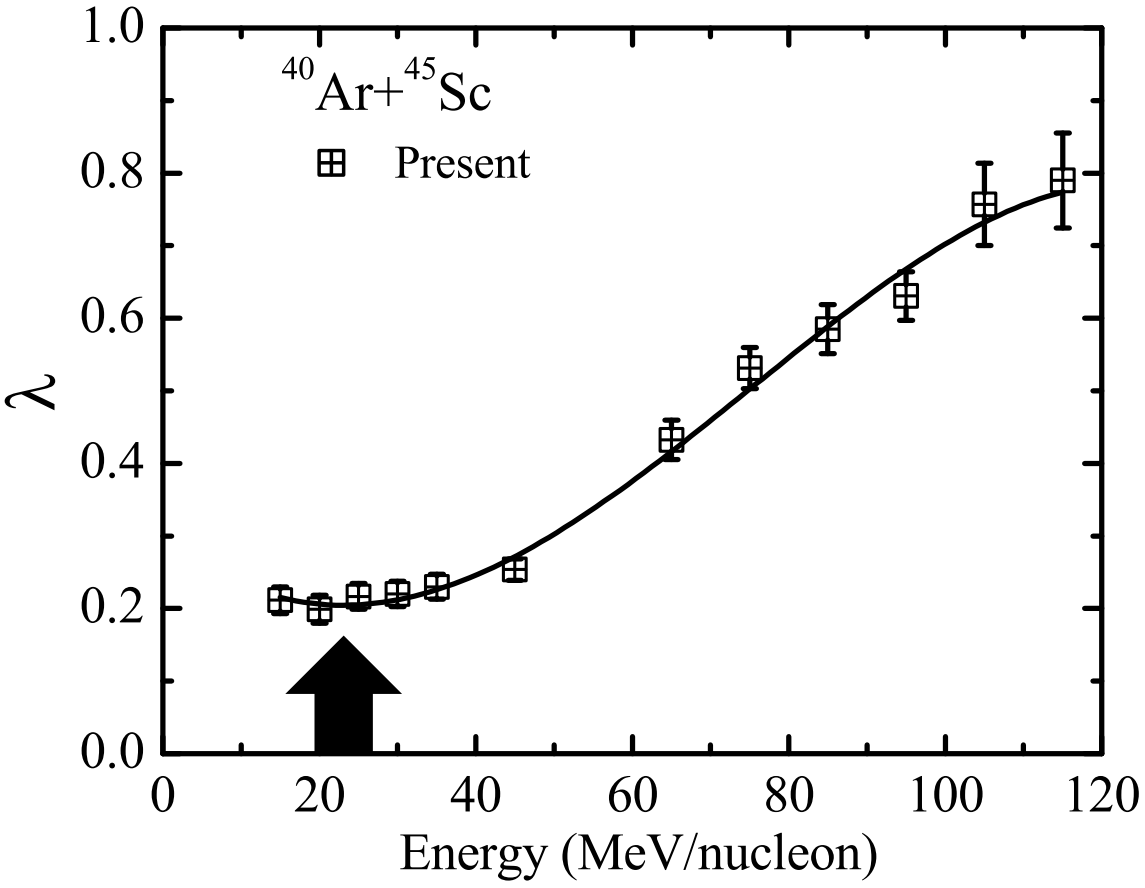

Figure 4.8: The extracted values of parameter λ, obtained using exponential fits $\propto e^{-\lambda Z_f}$ of IMFs as a function of beam energy. The solid line and solid arrow correspond to fourth order polynomial fit and a minimum in the extracted value of parameter λ.

MeV/nucleon). It is first time that such close agreement between model and experimental results is obtained.

It will be of further interest to investigate the multiplicity of various fragments around the onset of fragmentation. In Fig. 4.9, we display the multiplicity of free nucleons (FNs), light charged particles (LCPs) and intermediate mass fragments (IMFs) [$3 \leq Z_f \leq 12$] against incident energy emitted in the reactions of ^{40}Ar+^{45}Sc. From the figure, we notice that all the fragments show some disorder near the energy of the minimum in the power-law exponent τ. The multiplicities of free nucleons and light charged particles have little lower yield whereas the multiplicity of intermediate mass fragments shows maximal value around the energy of minimum value and are consistent with the earlier studies reported in Ref. [192].

As discussed in chapter 3, one needs to also analyze other critical parameters simultaneously to pin down the onset of fragmentation or possible critical behavior. Frequently used parameters are based on the study of moments e.g. $<S_2>$, $<\gamma_2>$, and size of the second largest fragment ($<Z_{max2}>$). The parameters $<S_2>$, $<\gamma_2>$, and $<Z_{max2}>$ (averaged over large number of events) should exhibit a peak at incident energy where minimum in the exponent parameter τ is obtained (for definition of critical exponents see previous chapter) [58, 121, 193, 195–198].

In Fig. 4.10, we display the average values of $<S_2>$, $<\gamma_2>$, and $<Z_{max2}>$ as a function of incident energy of projectile. We see that all these parameters passes through maximal value over the incident energy. Interestingly, all parameters $<S_2>$, $<\gamma_2>$, and $<Z_{max2}>$ predict a maximum at 20 MeV/nucleon, which is again very close to the earlier predicted value using τ/λ i.e., 20.1 (23.1) MeV/nucleon. Combining all the results from Figs. 4.5 to 4.10, our study predicts the critical point (or onset of fragmentation) to be in the band of 20-23.1 MeV/nucleon. One may also say that this is in close agreement with experimental data.

It would be of further interest to see whether QMD+SACA can also reproduce the trends reported for the reaction of ^{84}Kr+^{197}Au where no minimum in the power exponent was observed experimentally. In Fig. 4.11, we display the normalized charge distributions (crossed squares) [$3 \leq Z_f \leq 12$] obtained in the highly charged reaction of ^{84}Kr+^{197}Au at six different incident energies in the range of 35 and 400 MeV/nucleon. The available experimental data [49] for the same reaction is also displayed (see stars). Note that QMD+SACA is able to reproduce the experimental measurements for IMFs in most of

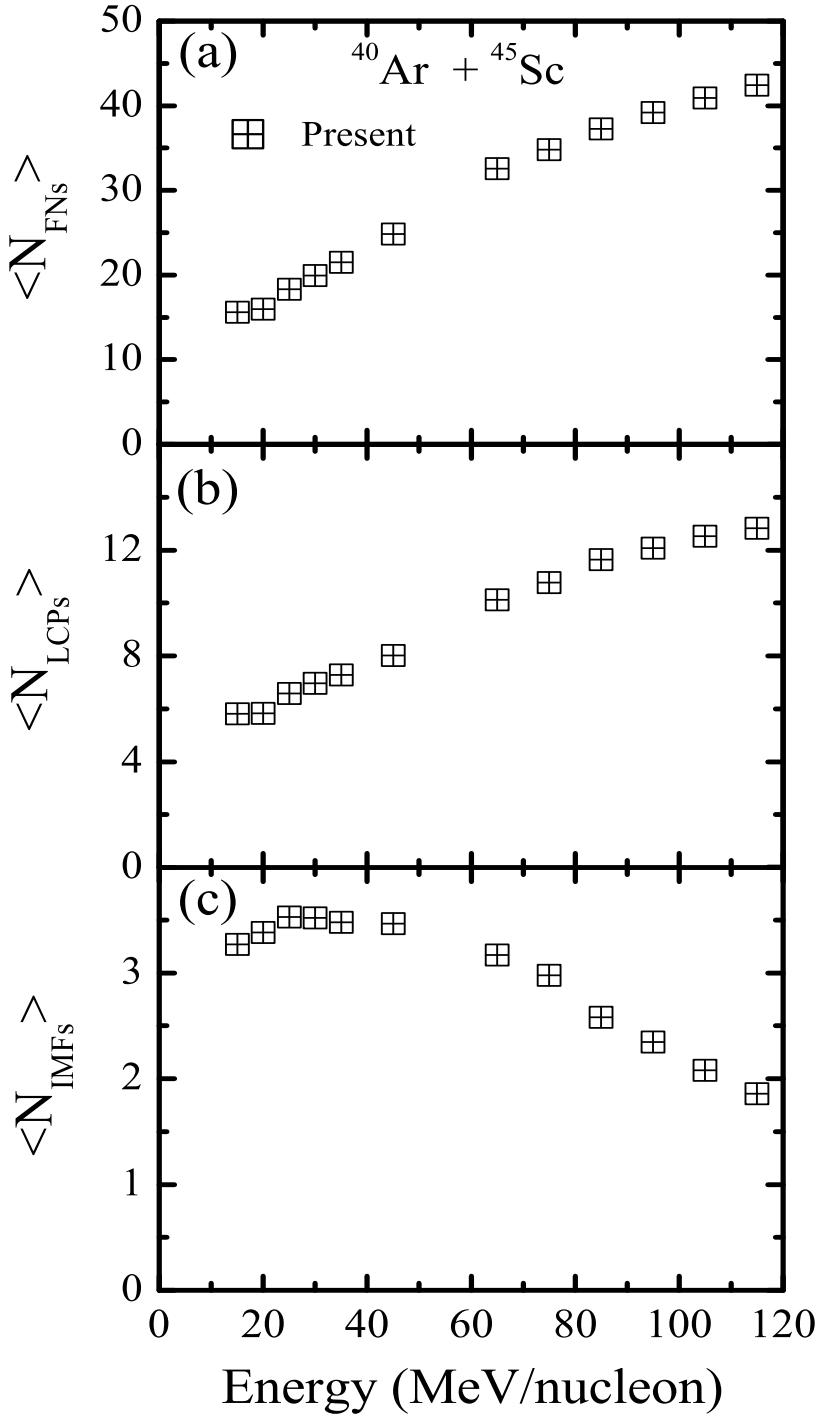

Figure 4.9: The average multiplicity of emitted free nucleons (FNs) (top panel), light charged particles (LCPs) (middle panel) and intermediate mass fragments (IMFs) (bottom panel) as a function of beam energy for the central reactions of ^{40}Ar+^{45}Sc.

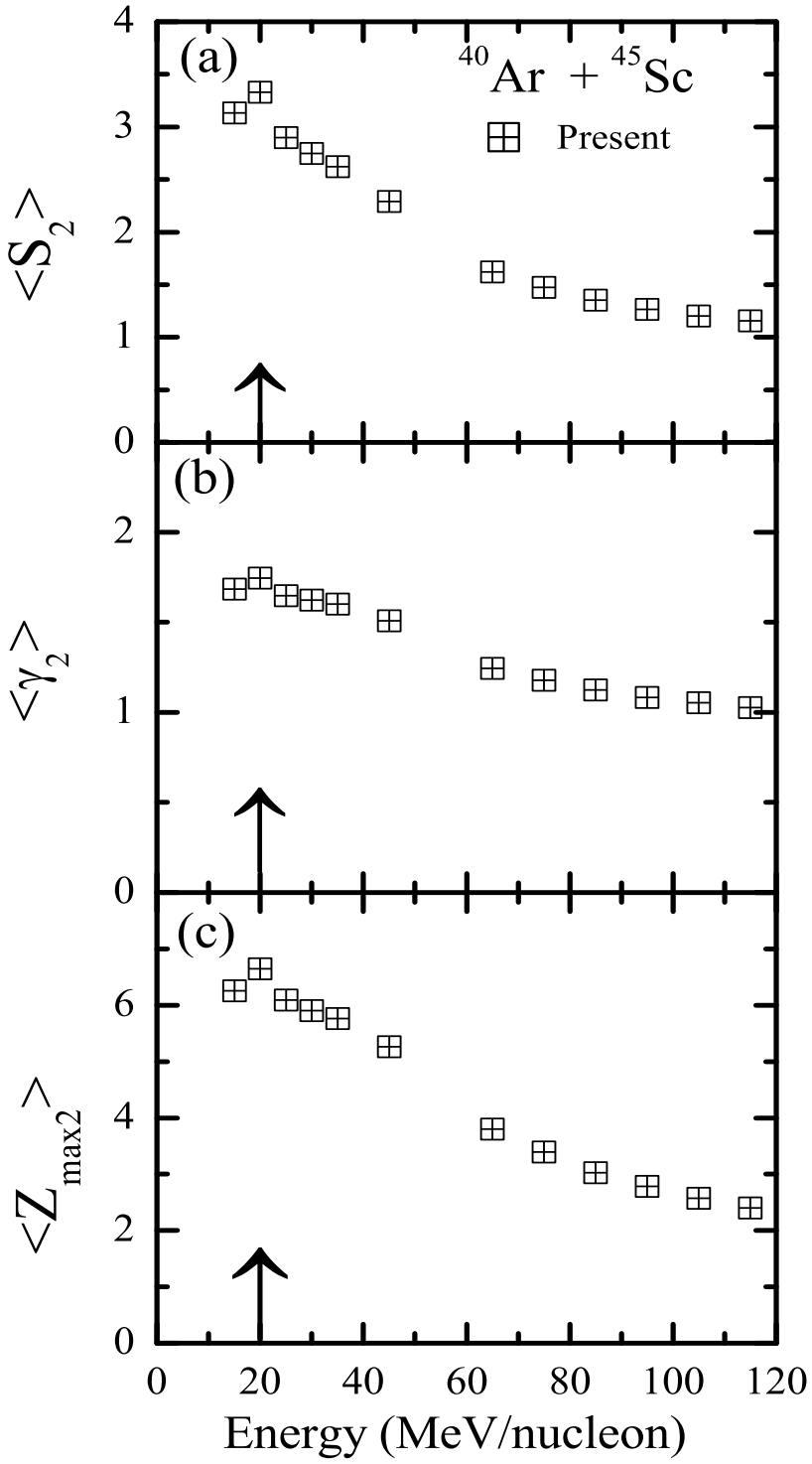

Figure 4.10: The values of normalized second moment <S_2>, the combinations of first three moments <γ_2>, and size of the second largest fragment (<Z_{max2}>) are plotted as a function of incident energy. The vertical arrows show the exact energy point of onset of fragmentation.

.

the cases.

Further, we again fit the charge yields at each incident energy with power-law fits $\propto Z_f^{-\tau}$ and the extracted values of power-law factor τ are plotted against incident energy in Fig. 4.12. From the figure, one notices that the extracted values of τ increase monotonically with incident energy without passing through minimum value. This absence of minimum in τ has been advocated to be due to dominance of long range Coulomb forces in highly charged systems [213]. In the figure, we also display the results of previous calculations (represented by different lines) reported using Statistical Multifragmentation Model (SMM) with and without sequential decay [49]. It was shown that rotational or radial flow indeed is required into the SMM model to correctly describe the experimental observations. At the same time one needs to apply sequential decays into the model. In the present study, we find that the present calculations using QMD+SACA give τ values that are close to the experimentally measured ones as well as to the SMM calculations with sequential decay [49]. We have also analyzed the other critical parameters λ, $<S_2>$, $<\gamma_2>$, and $<Z_{max2}>$ for this highly charged system (results are not shown here) and no discontinuity was found indicating the absence of minimum in this highly charged system. It is worth mentioning that no sequential decays are used in the present calculations for explaining experimental results. In the inset, we also displayed the results of τ down to the incident energy of 15 MeV/nucleon and no minima in the extracted values of τ is seen.

The consistency of the QMD+SACA approach to reproduce experimental data for light and heavily charged systems gives us faith that it can provide much reliable information about the onset of fragmentation. It is worth mentioning that SACA method does not have free parameter as in other calculations. Moreover, the fragments can be realized as early as $\sim$ 60-90 fm/c when system is still hot and dense. Further, this is the first ever consistent calculation which is in accordance with the onset of fragmentation in lighter system and subsequent absence of such trends in highly charged system.

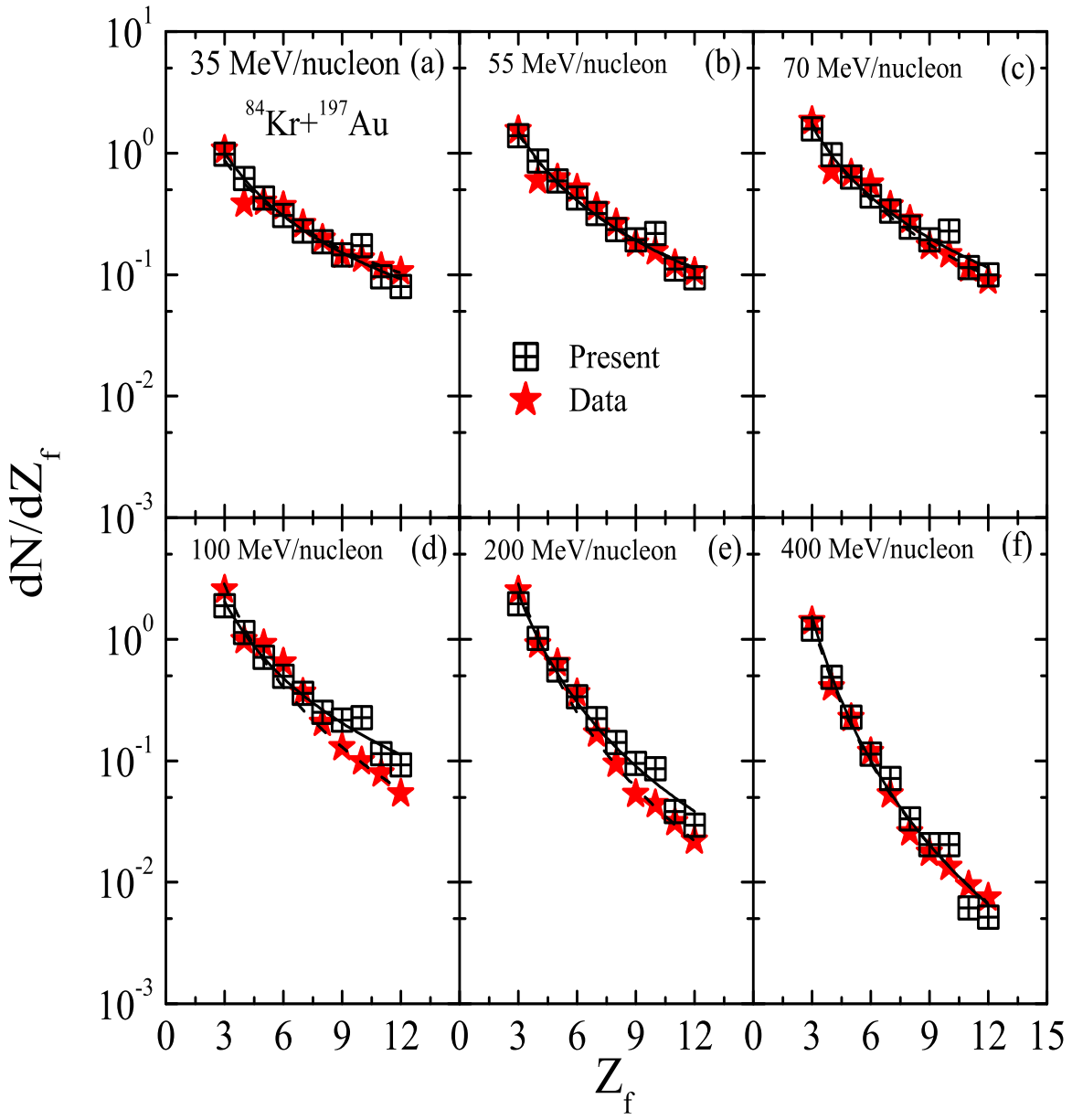

Figure 4.11: The normalized charge distributions obtained from the central reactions of ^{84}Kr+^{197}Au at six different beam energies between 35 and 400 MeV/nucleon. Solid lines represent the power-law fitting of IMFs [$3 \leq Z_f \leq 12$] obtained using QMD + SACA model.

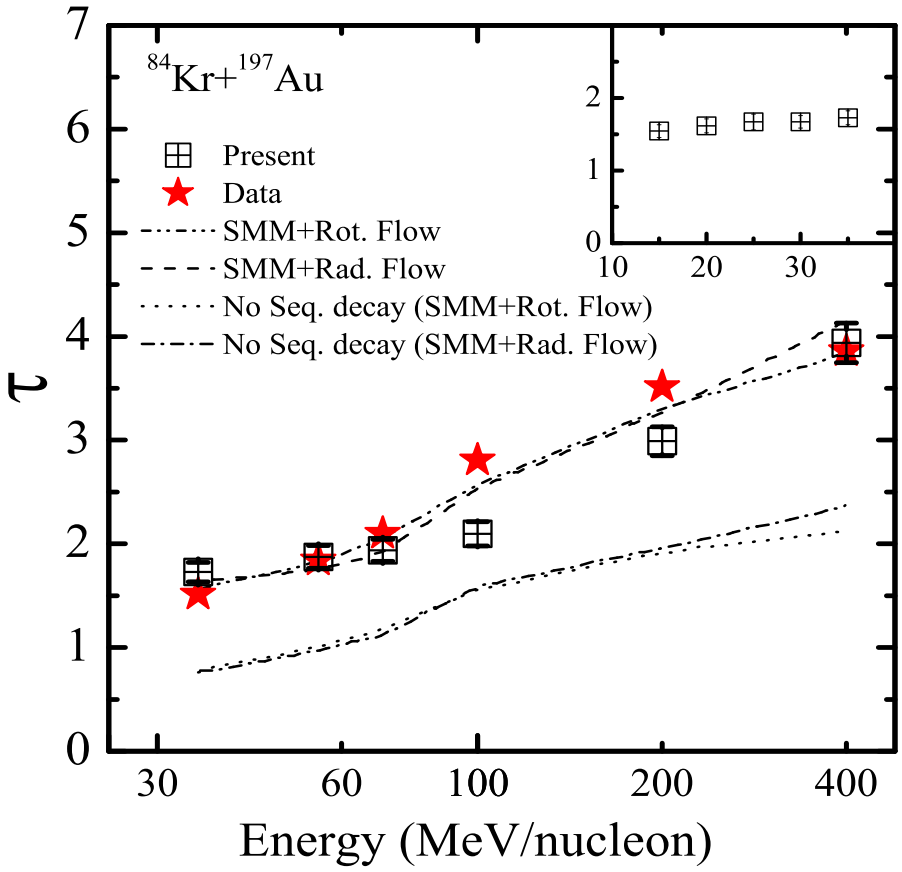

Figure 4.12: Extracted values of the power-law factor τ, obtained from the power-law fits of IMFs [$3 \leq Z_f \leq 12$] for the central reactions of ^{84}Kr+^{197}Au as shown in Fig. 4.10. Here, different lines represent the Statistical Multifragmentation Model (SMM) calculations with and without sequential decay.

4.4 Summary

In this chapter, we examine the charge yield of fragments and its connection with liquid-gas phase transition (i.e., the onset of multifragmentation) in light and heavily charged systems of ^{40}Ar+^{45}Sc and ^{84}Kr+^{197}Au, respectively. We have also used various other parameters and found that QMD+SACA calculations are consistent with the experimental measurements. Using different critical parameters, we obtained a minimum in the power-law exponent around 20-23.1 MeV/nucleon for ^{40}Ar+^{45}Sc systems which is close to the experimentally observed value of 23.9 MeV/nucleon. No such minima (or onset of fragmentation) is observed for ^{84}Kr+^{197}Au in agreement with experimental findings and other theoretical calculations. It is worth reminding that due to lack of fermionic statistics in the model, the QMD type model cannot be consistent with the realistic liquid-gas phase transition. Though, we could reproduce exactly the energy of the minima in the power law exponent as reported in the experiment, it does not necessarily indicate phase-transition.

Chapter 5

Onset of vaporization and role of mass asymmetry on the entropy production in heavy-ion collisions

Over the past few decades, with the help of experimental and theoretical studies, various aspects of dynamics of heavy-ion reactions have been explored, some of which are already discussed in previous chapters. These extensive studies have shown that the outcome of a reaction depends on various entrance channels e.g., incident energy of the projectile, impact parameter, mass of the colliding nuclei, mass asymmetry of the colliding nuclei as well as isospin asymmetry of the colliding partners (for details see chapter 1) [43, 49, 60, 71, 84, 97]. It is well known now that the mass asymmetry of colliding nuclei can change the outcome of a reaction to a a great extent. Generally, the mass asymmetry of a reaction is defined using asymmetry parameter η_A, where $\eta_A = |\frac{A_P - A_{Tar}}{A_P + A_{Tar}}|$; $A_P(A_{Tar})$ is the mass of the projectile (target). The value of η_A varies between 0 and 1, with $\eta_A = 0$ corresponding to symmetric reaction and the asymmetry of a reaction increases as one approaches the value 1, with $\eta_A = 1$ corresponding to extreme asymmetric reaction. The vital difference between symmetric and asymmetric reaction is that the former stores the energy in compressional form whereas the later stores major part of energy as thermal energy. Rigorous studies done in the past reveal a great role of mass asymmetry of colliding nuclei on the reaction dynamics at incident energies starting from low to ultra-relativistic ones. For example at low incident energies, it has been found that the magnitude of sub-barrier fusion is enhanced for systems with large mass asymmetry [234–236]. At intermediate energies, Ogilivie *et al.* studied the reactions of Au beam on C, Al and Cu at incident energy of 600 MeV/nucleon [43]. They observed a significant role of mass

asymmetry of reaction on the signals of liquid-gas phase transition [43]. In other study, Schuttauf *et al.* performed a more detailed observations where they analyzed the reactions with various mass asymmetries in the incident energy range of 400-1000 MeV/nucleon [71]. They showed that the energy of maximum IMF's production decreases linearly as one moves from symmetric to extreme asymmetric reactions. Out of various experimental studies done in the past, ISIS, FASA and PHENIX collaborations are amongst to study mass asymmetric reactions at relativistic incident energies [71, 237, 238].

In 1981 R. R. Betts performed a systematic study via keeping the total system mass of the reaction constant but varying their mass asymmetry and measured their fusion probabilities [239]. He proposed this method as a better way to understand the difference between dynamics of the symmetric and asymmetric reactions. On the similar lines, many other studies have been performed at lower incident energies. A few such attempts were also performed on various observables in heavy-ion collisions at intermediate energies e.g., Kaur *et al.* studied various reactions having η_A to vary between 0.0 to 0.6 in the incident energy range of 50 to 600 MeV/nucleon. The total system mass in this study was kept constant [240]. Their study reported the absence of rise and fall behavior for multiplicity of IMFs for highly asymmetric reacting partners when plotted against incident energy. They also showed the role of mass asymmetry on nuclear stopping at incident energy of 250 MeV/nucleon [241]. In another study, they analyzed the reactions of ^{50}Cr+ ^{102}Ru (η_A=0.3), ^{32}S+ ^{120}Sn (η_A=0.5) and ^{16}O+ ^{136}Xe (η_A=0.7) at incident energies between 50 to 250 MeV/nucleon and found that the transition energy (the energy at which elliptical flow changes from in-plane to out-of-plane) increases with increase in the mass asymmetry [242]. Puri and collaborators analyzed the role of the mass asymmetry on the energy of vanishing flow (EVF) and geometry of vanishing flow (GVF) [243, 244]. Their study reported a role as large as 40 % on EVF and 62 % on GVF between symmetric and highly asymmetric reacting partners. Recently, Puri *et al.,* proposed asymmetric reactions as a vital probe to constraint the density dependence of the symmetry energy at low densities [245]. In another study, Guo *et al.,* studied the mass asymmetric reactions of ^{16}O+ ^{197}Au at incident energy of 40 MeV/nucleon to investigate α-structure of ^{16}O [246]. Therefore, asymmetric reactions can also be a powerful tool to understand the structure of exotic nuclei such as α structure nuclei, halo-nuclei etc. but only, if first, one completely understands them for stable systems. All the above mentioned studies demonstrate the need and importance of understanding the dynamics of various asymmetric reactions to

map the complete reaction dynamics. This will be the prime aim of the present study.

5.1 Light particles and their role in understanding reaction dynamics

In the previous chapters, our focus was to study the physics associated with all or intermediate mass fragments. It is well known now that with the increase in the incident energy of projectile the abundance of bigger bound fragments ($A > 4$) decreases gradually [35, 60, 84, 247]. The energy at which the abundance of bigger bound fragments almost vanishes is known as the energy of "onset of vaporization" [35, 60, 84, 247]. At incident energies close to or higher than the energy of onset of vaporization, the physics related to the reaction dynamics is mainly governed by the light charged particles ($A < 5$). Moreover, one is always in search for observables that can provide information of the nuclear matter during its compressional stages. One such observable that preserves the early traces of the reaction and remains unaltered in the expansion phase of the compressed state of nuclear matter is "entropy" and can be obtained using yields of lighter mass fragments. Various valuable theoretical and experimental attempts have been done in the past to study the entropy production [51–56, 59, 61–64]. These studies have investigated the role of various entrance channel parameters on entropy production, like system mass, incident energy of projectile, isospin content of reacting partners and other reaction parameters like isospin dependence of cross-section, Gaussian width, equation of state. The entropy production was found to remain constant for all of these entrance channel parameters except for the Gaussian width of nucleons [51, 52]. Unfortunately, all these studies were limited to mass symmetric reacting partners only, whereas above paragraphs clearly show the crucial role of mass asymmetry on various observables used to understand the dynamics of a reaction. These studies motivated us to look for the role played by the mass asymmetry on the entropy production. In this chapter, we will focus on two main aspects. First, we will look for few aspects related to the energy of onset of vaporization and second we will analyze in detail, the effect of mass asymmetry on entropy production. The study of entropy production will be conducted via varying mass asymmetry of a reaction. We will keep the total system mass constant between 40 to 240 units and the mass asymmetry of reaction will be varied between 0.0 to 0.7. The study will be conducted at different incident energies between 400 and 1000 MeV/nucleon.

5.2 Onset of vaporization

The fragment pattern, of course, depends on the incident energy if impact parameter/geometry of the reaction is fixed. The production of intermediate mass fragments increases with incident energy but after certain incident energy, the free nucleons and lighter charged particles dominate the reaction outcome. This phase has been termed as vaporization in the literature and the incident energy at which this phase starts to dominate is termed as "onset of vaporization". A few attempts have been done to understand physics related to onset of vaporization which we will discuss in upcoming sections.

5.2.1 Review of literature on onset of vaporization

Jakobsson *et al.* were among firsts to study, in experiments, the reactions of ^{16}O+^{80}Br and ^{16}O+^{108}Ag in the incident energy range of 10 to 220 MeV/nucleon on event-by-event basis [35]. These experiments were conducted at GANIL and BEVALAC accelerators and only high multiplicity events (central collisions) were used for analysis. They found that the colliding systems first undergo from fission to multifragmentation at lower incident energies and then multifragmentation to vaporization at higher incident energies. It is worth mentioning that, in previous chapters, we have studied in detail the physics of onset of multifragmentation and its link to liquid-gas phase transition. Here, we will concentrate our discussion to higher incident energies only. To describe vaporization, they used the sum of charges of fragments ($< Z >$) with and without including the charge of the largest fragment ($< Z_1 >$). They observed that the value of $< Z >$ decreases rapidly whereas $< Z_1 >$ remains almost constant above 20 MeV/nucleon for both ^{16}O+^{80}Br and ^{16}O+^{108}Ag reactions. The reason for this is the decrease in the size of the largest cluster (Z_{max}) as incident energy increases. This further showed that, the increasing amount of excitation energy is mainly used to break the heaviest fragment into pieces. They have also presented the value of $< Z > \sim 1.4$ at 2 GeV/nucleon which signifies that only lighter charge particles sustains at these energies. For theoretical description, Souza *et al.* had performed calculations using Quantum Molecular Dynamics (QMD) + Restructured Aggregation Model (RAM) model for the reaction of ^{16}O+^{80}Br. They were successful in reproducing the experimental results above 50 MeV/nucleon [60]. They analyzed various other reaction observables such as charged particle multiplicity ($< N_c >$), multiplicity of IMFs ($< N_{IMFs} >$) etc and stressed that above 200 MeV/nucleon only lighter fragments

dominate the reaction outcome. Their findings revealed the onset of vaporization to exist around 200 MeV/nucleon [218]. In the same direction, Tsang *et al.* performed an experiment at GSI, Germany, with the ^{197}Au beam on ^{197}Au target [84]. The reactions were performed at incident energies of 100, 250 and 400 MeV/nucleon. They showed that for central impact parameter, the multiplicity of IMFs decreases gradually with incident energy and for incident energies $\geq$ 400 MeV/nucleon the multiplicity of IMFs is $<$ 1. Thus, almost all the charge is in the form of lighter mass fragments only. For theoretical description, they used QPD+EES (Expanding Evaporation System), QMD+MST and QMD+SMM. They depicted inconsistency with the dynamical models to describe the results which was resolved when QMD was coupled with SACA method for fragments. Later on, Bacri *et al.* in their experiment using 4π multi-detector INDRA, studied reactions between ^{36}Ar and ^{58}Ni in the incident energy range of 32 and 95 MeV/nucleon [247]. They found that to vaporize the system into free and light charged particles, one needs a minimum excitation energy of $\sim$ 12 MeV/nucleon. Interestingly, this excitation energy is twice the energy required to have maximum abundance of α-particles. These lighter fragments are used to estimate the entropy production in heavy-ion collisions. Let us first give an overview of the literature on the entropy production in heavy-ion reactions at intermediate energies.

5.3 Overview of previous attempts on entropy production

Siemens and Kapusta were among firsts to calculate the entropy production in the heavy-ion collisions. Their method was based on a highly idealized assumption of perfect gas [53]. They proposed to use the deuteron-to-proton ratio to calculate entropy considering it to be saturated very early during a reaction. Bertsch and Cugnon generalized this assumption considering the presence of other lighter clusters like t, ^{3}He, ^{4}He [54]. They included these lighter clusters to estimate entropy. Some other assumptions like by Stöcker *et al.* to include heavier fragments ($A >$4) to calculate entropy [62], by Jacak *et al.* to determine entropy using fragments $1\leq A \leq 14$ in mid-rapidity [63], also exist in nature. But these assumptions were found to influence the results in the lower side of incident energies where heavier fragments have significant yield.

Further, the method to estimate entropy was debated intensively in the early days,

therefore, many studies used various definitions to calculate entropy. For e.g., Doss *et al.* [55] measured the entropy for the reactions of ^{40}Ca+^{40}Ca and ^{93}Nb+^{93}Nb at incident energies of 400 and 600 MeV/nucleon, respectively. Doss *et al.* also measured the yield ratios for lighter fragments and concluded the consistency of results with Quantum Statistical Model (QSM) [55]. They showed the mass independence of the entropy calculated by using the definitions of Siemens and Kapusta and Stöcker *et al.* (will be explained in detail in next section). Later on, the Cascade Model calculations were also performed using assumptions of local equilibrium in addition to the method proposed by Bertsch and Cugnon [54]. These studies showed that at lower incident energies, results are quite different compared to experimental data whereas, at higher incident energies. In the literature, many studies have been done using various transport models. Aichelin *et al.* have studied the role of Momentum Dependant Interactions (MDI) and Equation of State (EOS) using BUU model for the ^{40}Ca+^{40}Ca reactions [11]. The results were found to be insensitive towards momentum dependence of the potential but dependent on Equation of State (EOS). Puri *et al.* calculated the d_{like} and p_{like} ratio as a function of participant proton multiplicity and entropy production for the reaction of ^{40}Ca+^{40}Ca and ^{93}Nb+^{93}Nb at different incident energies between 400 and 1050 MeV/nucleon using Quantum Molecular Dynamics (QMD) model [51]. The results were found to be in good agreement with 4π Plastic Ball Data [51]. Later on, using IQMD model they reported that with increase in the neutron content, the entropy production decreases i.e., with an increase in neutron content the nuclear system gets more and more ordered. They also showed the significant dependence of entropy production on the EOS and Gaussian width [52]. All these calculations were done for symmetric reactions only [52]. It can be clearly seen that the majority of the studies done and results reported in the past are for symmetric reactions. Very few studies have been done to understand the dynamics of asymmetric reactions for entropy production e.g., the CHIC collaboration have studied various mass asymmetric reactions ranging from proton-nucleus to nucleus-nucleus reactions (p+Kr, O+Kr and Ne+Au) in the incident energy range of 30 MeV/nucleon to 350 GeV [63]. They estimated the ratios, R_{dp} (deuteron to proton) and R_{tp} (triton to proton), and corresponding entropy production. The statistical evaporation models were reported to fail in reproducing these experimental observations. Whereas, the mean field models were successful in explaining the experimental results to some extent. As their study was done using inclusive data of reactions, therefore, their conclusions were not exact or were

blurred. In another study, Trockel *et al.* studied the reactions of ^{12}C+ ^{197}Au at incident energies of 30, 48 and 84 MeV/nucleon [64]. This study reported that the entropy production calculated using lighter particles increases with the increase in the incident energy. Nagamiya *et al.* in their experiments at Berkeley Bevalac, studied the reactions of C+C, C+Pb, Ne+NaF, Ne+Cu, Ne+Pb, Ar+KCl and Ar+Pb at 800 MeV/nucleon, and Ne+NaF and Ne+Pb at 2.1 GeV/nucleon [248]. They reported the yields of lighter mass particles (i.e., p, d, t, ^{3}He and ^{4}He), their ratios and entropy production. They observed that the ratios of d/p, t/p, and ^{3}He/p show a rapid decrease with incident energy for symmetric reactions compared to asymmetric reactions. Later, Danielewicz and Bertsch tried to reproduce the data using cascade model but found inconsistencies in explaining the d/p ratio [249]. These studies on entropy production show that interesting aspects of reaction dynamics can be explored via studying entropy production of asymmetric reacting partners. Moreover, no systematic study of entropy production is ever been done for mass asymmetric reacting partners and is the prime aim of this study. Before that, we shall demonstrate the detailed formalism of computing entropy production.

5.4 Entropy production in heavy ion collisions

It is well explained and discussed in earlier chapters that the dynamics of heavy-ion collisions at intermediate energies is very complex and difficult to understand. On one hand it is due to the short span for which the hot and dense state of nuclear matter is formed, on the other hand, it is also due to the fact that one can detect the fragments only at the time when nuclear matter is well diluted and cold. Therefore, one is always in search for observables that can directly reflect or trace back the properties of nuclear matter during the hot and compressed state. In this direction, specific entropy is found to provide such traces as it first increases, but as soon as the compressed phase of a reaction is over, thus during expansion, remains constant. The last three decades have witnessed many different methods to accurately calculate entropy. In the earliest attempt, it was suggested that after the equilibrium is set in the reaction zone, the entropy can be calculated using the deuteron-to-proton ratio, R_{dp}. The basis of this assumption was to consider the system as ideal gas consisting of mainly neutrons and protons in local equilibrium, allowing one to calculated entropy per nucleon using Sackur-Tetrode equation:

$$\frac{S}{A} = \frac{5}{2} - \frac{\mu_A}{\tau}. \tag{5.1}$$

Here, μ_A and τ are the chemical potential of the protons and temperature of the system, respectively. Then for a composite particle of A nucleons, the chemical potential μ_A is given by

$$\mu_A = \tau \ln \left[\frac{n_A}{n_A^c} \right] - \varepsilon_A. \tag{5.2}$$

In this equation, n_A and ε_A represent the density of composite system of A nucleons and its corresponding binding energy, respectively. Also, n_A^c is termed as chemical density and is represented by

$$n_A^c = g_A \left(\frac{m_A \tau}{2\pi\hbar^2} \right)^{3/2}, \tag{5.3}$$

where m_A and g_A are the mass of the fragment A and it isospin degeneracy, respectively.

Siemens and Kapusta [53] assumed that in a case, if the number of protons outnumber deuterons in a given system and further no significant contribution from heavier clusters, the entropy per nucleon can be calculated as:

$$\frac{S}{A} = \frac{5}{2} - \left\{ \frac{\varepsilon_A}{\tau} + \ln \left[\frac{g_d}{g_p} \left(\frac{m_d}{m_p} \right) \right] - \ln \mathrm{R}_{dp} \right\}. \tag{5.4}$$

Now, if the temperature of the system is much larger than the binding energy of the deuteron, the above equation reduces to

$$S_N = 3.945 - ln R_{dp}, \tag{5.5}$$

where, R_{dp} is the deuteron-to-proton ratio. The experiments have clearly shown that R_{tp}(triton-to-proton ratio)$<<$ $R_{dp} \leq 0.4$ at E $\geq$ 400 MeV/nucleon, the above formula was expected to give consistent results. Unfortunately, the entropy per nucleon observed using this formula was much larger compared to what was measured in experiments. Later, Bertsch and Cugnon studied the entropy production for the reactions of $^{40}Ca+$ ^{40}Ca using Cascade model. To calculate the entropy they replaced the number of deuteron and protons with the deuteron-like and proton-like clusters [54]. The deuteron-like and proton-like clusters were calculated including the ground state of the particles with masses from 2 to 4 (i.e., t, ^{3}He, ^{4}He) [54]. In this modified definition, the formula to calculate entropy per nucleon reads as:

$$S_N = 3.945 - ln \tilde{R}_{dp}, \tag{5.6}$$

where

$$\tilde{R}_{dp} = \frac{d_{like}}{p_{like}} = \frac{d + \frac{3}{2}(t + {}^3He) + 3\ {}^4He}{p + d + t + 2\ {}^3He + 2\ {}^4He}. \tag{5.7}$$

This formulation to some extent removes the reliance on chemical equilibrium and diluteness of nuclear system. Later on, Stöcker *et al.* proposed the inclusion of heavier fragments ($A > 4$) in the formulation for entropy production [62]. This inclusion was considering the formation of bigger fragments also at higher densities but lower temperatures. The contribution of this proposition was found to be significant only at lower incident energies, whereas at higher incident energies the number of heavier fragments ($A > 4$) is very small, therefore, no significant role is seen on entropy production. Peilert *et al.* put forward a parameterized form of the above formula to estimate entropy production [59] and it reads as:

$$\tilde{R}_{dp} = \frac{d_{like}}{p_{like}} = \frac{Y(A=2) + \frac{3}{2}Y(A=3) + 3Y(A=4)}{N_p}, \tag{5.8}$$

where Y(A='n') stands for the number of fragments with multiplicity 'n' in one event. The participant proton multiplicity is calculated as:

$$N_p = \frac{Z_p + Z_{Tar}}{A_P + A_{Tar}}[Y(A=1) + 2Y(A=2) + 3Y(A=3) + 4(Y=4)]. \tag{5.9}$$

We will use above equations to calculate proton-like and deuteron-like clusters, their ratio and finally entropy production. We will pursue our study using available transport model and for all the possible mass asymmetries.

5.5 Results and discussion

5.5.1 Results of onset of vaporization

For the present analysis, we have simulated the reactions of ^{16}O+^{80}Br at incident energies between 15 and 200 MeV/nucleon. We have used a soft equation of state along with energy-dependent cross-section. This is to keep into mind that this study is only first hand attempt to put forward the sensitivity of the point of onset of vaporization towards some technical parameters of clusterization algorithms and different clusterization techniques. The other main aim of this part is to also show that at higher incident energies, only lighter particles dominate the reaction results within the present model calculations. We will here use the parameters $< Z >$ and $< Z_1 >$ to observe the vaporization phase in accordance to the one used by Jakobsson *et al.* [35] and Souza *et al.* [60].

Before understanding other aspects, it is important to question whether the model used for the calculations itself contains the desired physics related to vaporization or not.

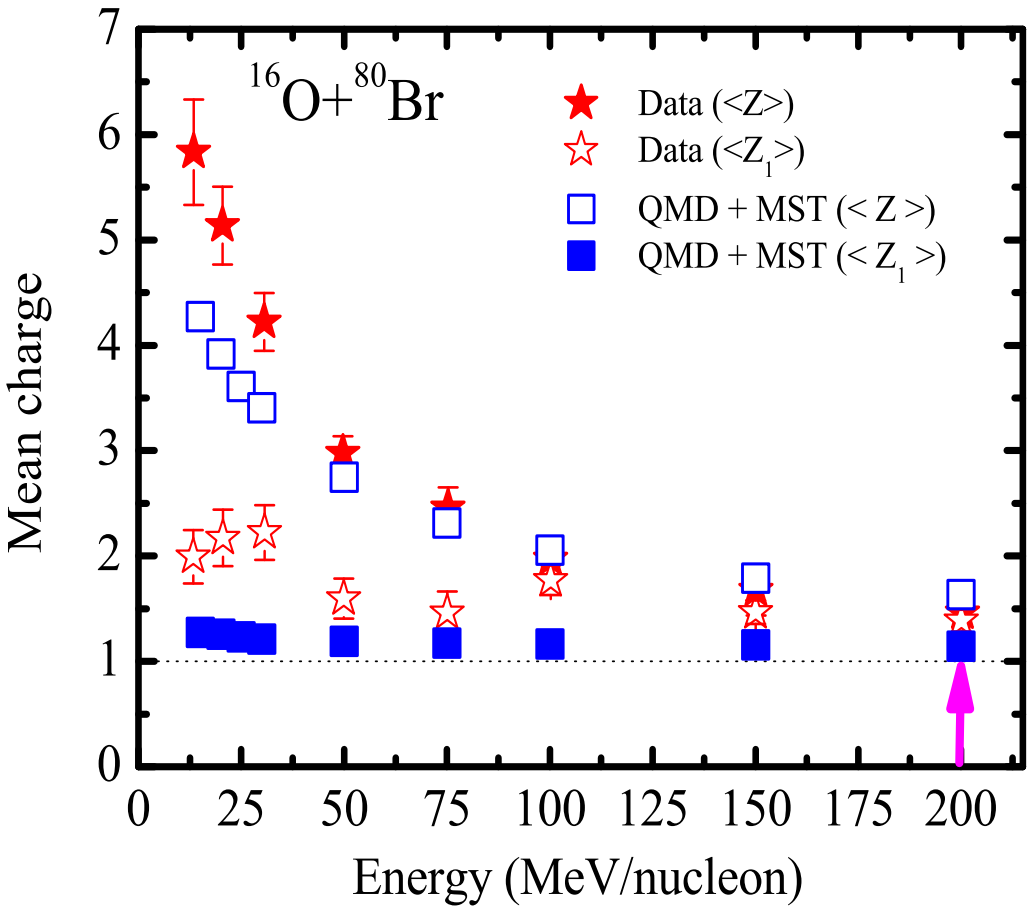

Figure 5.1: The mean charge with ($< Z >$) and without ($< Z_1 >$) largest fragment as a function of incident energy for the system of ^{16}O+^{80}Br. The symbols are explained in the text.

To take care of this aspect, we try to reproduce the available experimental results on the onset of vaporization. In Fig. 5.1, we have plotted the normalized average charge in each event with ($< Z >$) and without largest fragment ($< Z_1 >$) as a function of incident energy. The method of calculating normalized mean charge is same as reported in Refs. [35, 60]. The Open (filled) stars represent the experimental data of $< Z_1 >$ ($< Z >$) and open (filled) squares represent the corresponding calculations using QMD with default MST method (R_{clus} =4 fm) (labelled as 'MST'). From the figure, we see that the normalized mean charge ($< Z >$) decreases with increase in the incident energy as more amount of energy is stored inside the system that leads to extra breaking and cracking, thus, lesser number of larger fragments. Here the energy of vaporization is taken to be the one where $< Z >$ reaches asymptotic value. The $< Z > \simeq 1$ signifies that the correlations among nucleons are completely broken and matter is in the form of single nucleons only. One can figure out immediately that the QMD + MST model with default values is able to reproduce experimental data at all incident energies reasonably well. The exact reproduction happens only above incident energy of 50 MeV/nucleon. The failure of MST method at lower incident energies happen due to its inability to separate fragments which are overlapping in coordinate space due to lower fragment velocities. This leads to one large fragment instead of many intermediate mass fragments. This is supported by the results of normalized charge excluding largest fragment $< Z_1 >$. We see that the MST method has serious problem at lower incident energies whereas it explains experimental data nicely at higher energies. Nevertheless, QMD + MST model is able to reproduce the onset of vaporization quite nicely which is reported to be around 200 MeV/nucleon.

Role of different spatial constraints on vaporization

Though, the MST method remains the most widely and successful method in the literature to identify fragments, some studies have shown that the clusterization range used in the MST method can also lead to change in the results [250]. Therefore, it would be of further interest to see whether spatial range used for constructing the fragments affect the onset of vaporization or not. For this, we also performed same calculations using R_{clus} = 3 and 5 fm also. The results are displayed in Fig. 5.2. We see some effect of altering the clusterization range at lower incident energies where nucleons are still close in the space. The effect however vanishes at higher incident energies. On the average, altering the range of clusterization by 25 % changes $< Z >$ by 12 % at 15 MeV/nucleon

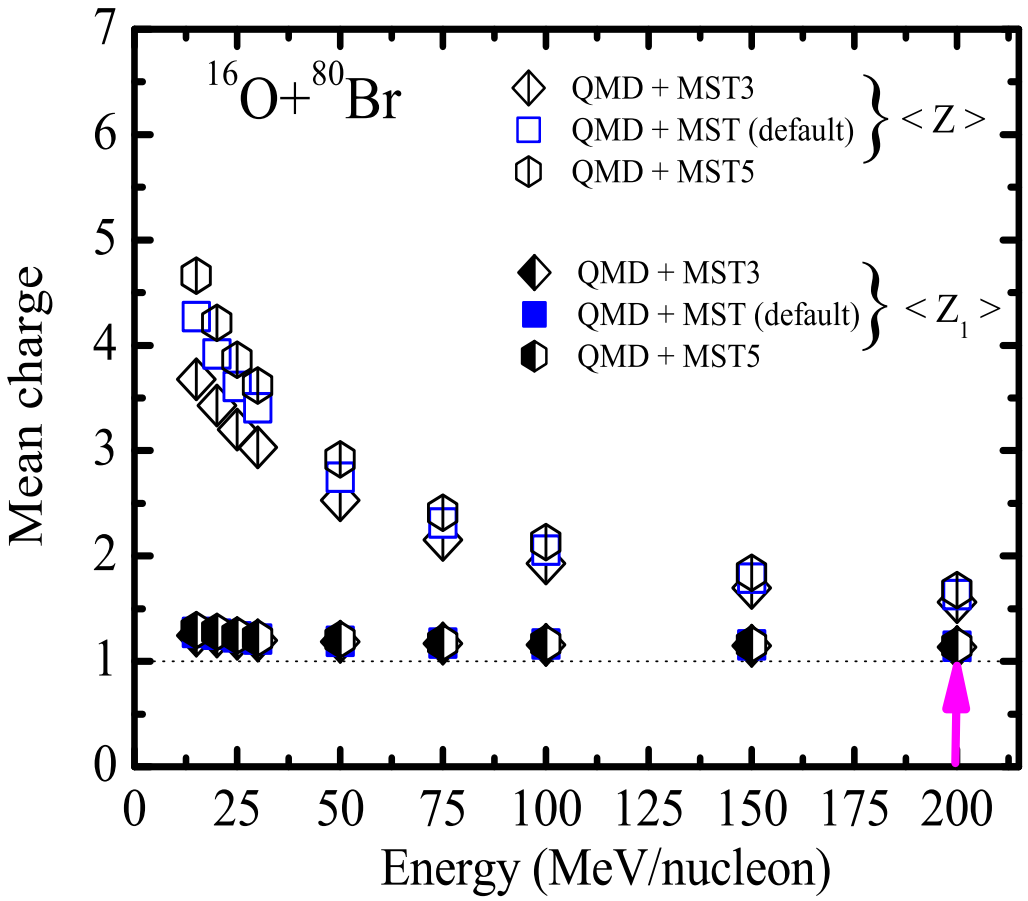

Figure 5.2: Same as Fig. 5.1, but using different R_{clus} values in MST method.

whereas the effect reduces to 6 % at 200 MeV/nucleon. Further, it is evident that the clusterization range do not affect the energy of the onset of vaporization. The uncertainty of 6 % is within the experimental error limits, therefore, one can say that the results on the onset of vaporization are independent of the variation in the spatial constraints used in clusterization algorithm. The results can be understood in terms of the expansion in the constituent nucleons of the system at different incident energies in accordance with earlier studies [71, 251]. At lower incident energies, the nucleons expand at lower rate and are close to each other. Therefore, the change in the clusterization range in the MST method can give different fragment sizes. With increase in the incident energy, the phase-space is opened up at faster rate and at freeze out, only those nucleons are close which are part of the same fragment. Thus, the role of different clusterization ranges do not alter the results of fragments significantly at incident energy close to onset of vaporization.

Role of different clusterization on the onset of vaporization

As mentioned in earlier chapters, one can use different definitions to obtain clusters. The role of these definitions was found to be insignificant on the signals of the onset of multifragmentation or liquid-gas phase transition (discussed in chapter 3). But one should keep into mind that the absolute values were indeed affected by the change in cluster definitions. In chapter 3, the discussion was focussed on the onset of multifragmentation, thus, only to the lower incident energies. Here, our aim is to analyze the onset of vaporization which occurs at relatively higher incident energies. Therefore, it is of interest to see how results are changed with the choice of clusterization algorithm. In particular, we will use MST, MSTP, SACA with the QMD model, and MST, MSTP with the IQMD model [11, 141, 154, 155, 159]. The details of these different methods of clusterization can be found in chapters 2 to 4.

In Fig. 5.3, we show the results of $< Z >$ and $< Z_1 >$ with the above mentioned combinations of primary models and clusterization algorithms. The results of QMD coupled with MST, MSTP and SACA are represented by open (filled) squares, circles, and double(half crossed) crossed squares, respectively, whereas, the results of IQMD coupled with MST and MSTP are represented as open (filled) triangles, and inverted triangles, respectively. From the figure, we see that the value of $< Z >$ is greatly influenced at lower incident energies but gives the same values at higher incident energies where onset of vaporization appears. One can understand the results as following: at lower incident

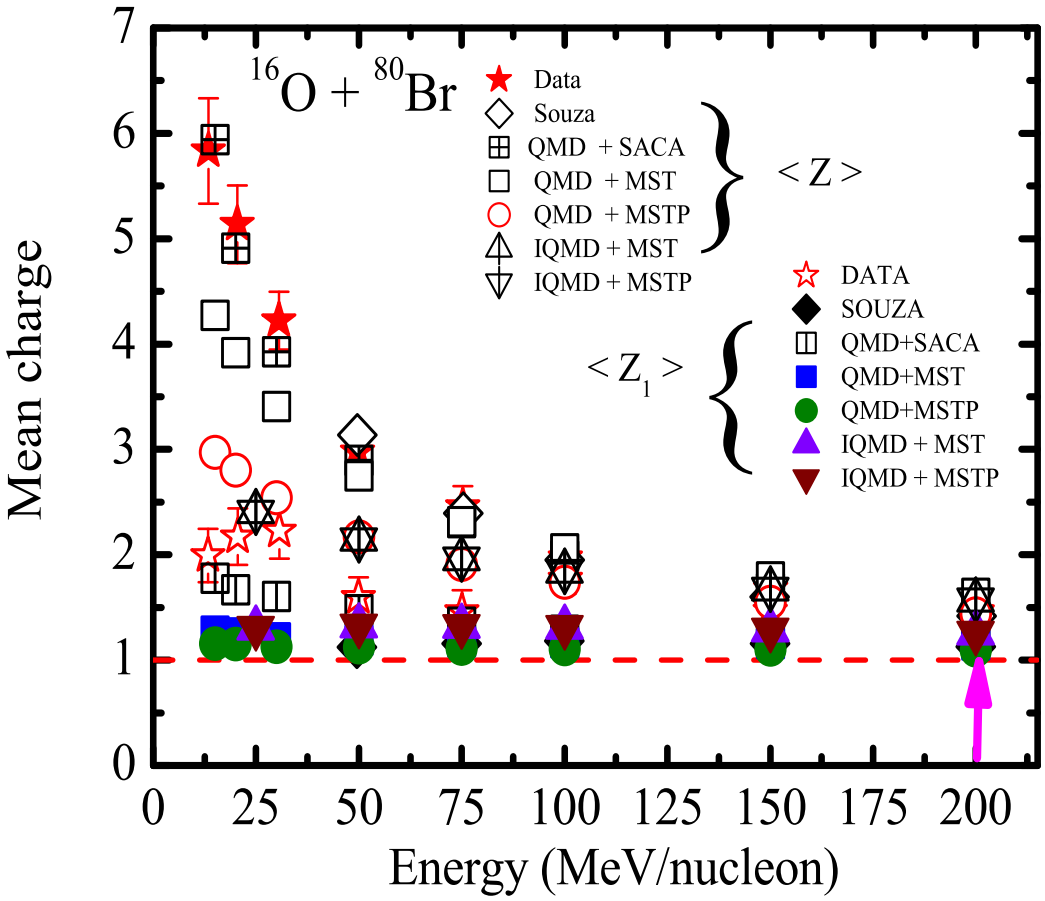

Figure 5.3: Same as Fig. 5.1, but using different clusterization algorithms MST, MSTP and SACA. We have also shown the calculations using IQMD+MST and IQMD+MSTP models.

energies less phase-space is available for the nucleons and they are close to each other. As discussed earlier, the MST method being based on the spatial constraints is unable to separate out the fragments even if they have only one common nucleon. If one enforces the MSTP method, the picture changes significantly. Now the calculations are more away from the experimental results. The MSTP method, which is based on the spatial+momentum constraints is able to separate many overlapping clusters but the production of excess number of free particles reduces the values of $< Z >$ and $< Z_1 >$. Hence the MSTP results are more deviated compared to the MST method. If one shifts to the SACA method, the results are significantly improved with respect to the MST and MSTP methods, and also consistent with the experimental observations. These results are complementary to what we observed in chapter 4. The success of SACA method reflects its ability to identify fragment configurations even if they are overlapped. Nevertheless, we also specify here that the failure of one clusterization algorithm in reproducing the absolute values does not make them unsuitable to discuss physics related to that observable. It only reflects the inability of the algorithm to contain certain features related to that observable. The bottleneck in the present calculations is the insignificant role of different algorithms at incident energies where vapor phase starts to appear. Moreover, the results of QMD and IQMD models with different cluster definitions are also same at energies where vapor phase starts dominating. The same kind of results were reported by Souza *et al.* [60] for vaporization, but using QMD + RAM model (see diamonds in figure). One should keep into mind that the QMD model used by Souza *et al* have many modifications such as Pauli principle, isospin etc. over the one used in the present study. Further, the RAM model used to identify fragments is much more complex compared to the present clusterization algorithms [229]. At the same time, one alters with the phase-space in RAM method to obtain spherical fragments, thus, distorts the actual physics related to reaction. This is not the case in the clusterization algorithm used in the present study. The present calculations with all primary+secondary algorithms are indeed close to the experimental results where vapor phase persists and consistent with earlier calculations. Therefore, one can say that all these combinations contain the desired physics related to vaporization. Note that this is the first ever study in the last two decades on the vaporization, but a detailed study is still required to extract all the physics related to vaporization. The present results are that at higher incident energies most of the system is broken into lighter mass fragments ($A < 5$) within the present models also. If one

wants to discuss any physics at higher energies one should study the observable related to lighter fragments only. One such observable is "Entropy" that is derived from the ratio of lighter mass fragments will be discussed in upcoming sections.

5.5.2 Results of entropy production

For the present study, we simulated several thousand events for various reactions. As mentioned earlier, for these reactions, the mass asymmetry of the colliding nuclei will be varied between 0.0 and 0.7 via keeping the total system mass constant between 40 to 240 units. In this case, we simulated the reactions of ^{20}Ne +^{20}Ne (η_A=0.0),^{18}F+^{22}Ne (η_A=0.1), ^{14}N+^{26}Mg (η_A=0.3), ^{10}B+^{30}Si (η_A=0.5) and ^{6}Li+^{34}S (η_A=0.7) for A$_T$= 40; ^{40}Ca+^{40}Ca (η_A=0.0), ^{36}Ar+^{44}Ca (η_A=0.1), ^{28}Si+^{52}Ca (η_A=0.3), ^{20}Ne+^{60}Ni (η_A=0.5) and ^{11}B+^{69}As (η_A=0.7), for A$_T$= 80; ^{80}Kr+^{80}Kr (η_A=0.0), ^{70}Ge+^{90}Zr (η_A=0.1), ^{54}Fe+^{106}Pb (η_A=0.3), ^{40}Ca+^{120}Te (η_A=0.5) and ^{24}Mg+^{136}Nd (η_A=0.7), for A$_T$=160 and ^{120}Sn+^{120}Sn (η_A=0.0), ^{108}Cd +^{132}Ba (η_A=0.1), ^{84}Sr+^{156}Dy (η_A=0.3), ^{60}Ni+^{180}W (η_A=0.5) and ^{36}Ar+^{204}Pb (η_A=0.7) for A$_T$=240.

The reactions are simulated at incident energies between 400 and 1000 MeV/nucleon. As discussed earlier, at these incident energies only vapor phase persists, thus system exists only in terms of the lighter mass clusters. It is worth noting that all the calculations are done by using the IQMD model in which the Fermi momentum is reduced by 30 % for soft equation of state. All results are analyzed at 40 fm/c as upto this stage the compressed phase is over.

5.5.3 Entropy production at fixed beam energy

In the Fig. 5.4, we demonstrate the ratios of $< A = 2/p >$, $< A = 3/p >$ and $< A = 4/p >$ as a function of system mass at incident energy of 400 MeV/nucleon. Here results are shown for various mass asymmetries corresponding to total system mass of 40, 80, 160 and 240. The mass asymmetry parameter (η_A) varies between 0.0 and 0.7. The results obtained for different mass asymmetries of 0.0, 0.1, 0.3, 0.5 and 0.7 are represented by squares, circles, triangles, hexagons and diamonds, respectively. For further discussion, these symbols will be kept same.

From the figure, we see an uniform rise for the $< A = 2/p >$, $< A = 3/p >$ and $< A = 4/p >$ as the system mass increases for different mass asymmetries. To get a better

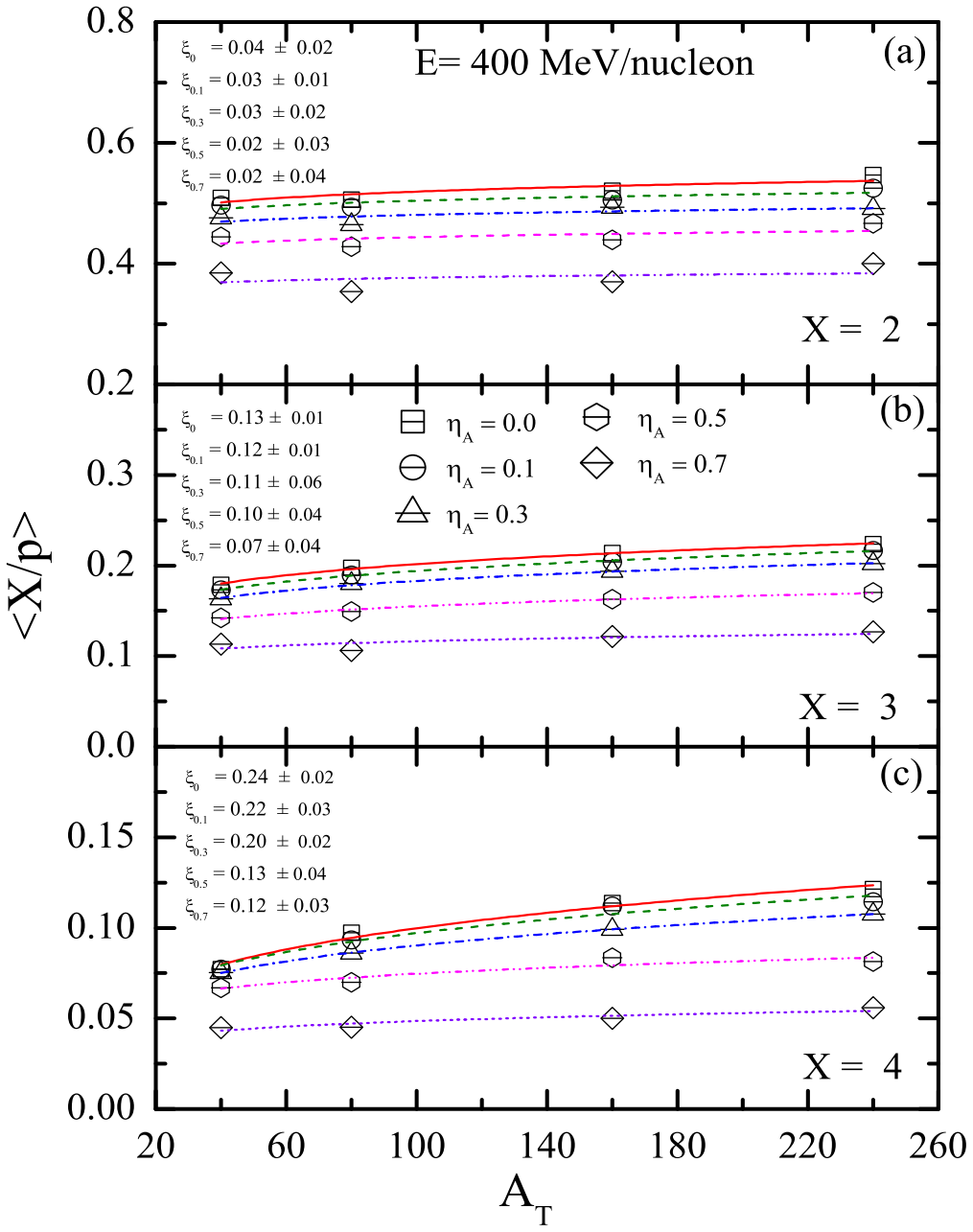

Figure 5.4: The composite yield ratios, <X/p> where X stands for A= 2, A= 3 and A= 4 as a function of total system mass for various mass asymmetries at an incident energy of 400 MeV/nucleon. The results of mass asymmetries of 0.0, 0.1, 0.3, 0.5 and 0.7 are represented as lined, squares, circles, triangles, hexagons and diamonds, respectively.

picture, the ratios as a function of total system mass are fitted with power law ($\propto A_T^{\xi}$). We see that for a fixed mass asymmetry, the values of slopes obtained using power law is always positive for all ratios, $< A = 2/p >$, $< A = 3/p >$ and $< A = 4/p >$. We also find that the slopes of the ratios is decreasing in the order starting from $< A = 4/p >$, $< A = 3/p >$ to $< A = 2/p >$ e.g., for η_A=0.0, the values of slopes (without errors) are 0.24, 0.13 and 0.04, and for η_A=0.7, the slopes are 0.12, 0.07 and 0.02 for the ratios of $< A = 4/p >$, $< A = 3/p >$ and $< A = 2/p >$, respectively. Therefore, the slopes are less steeper in asymmetric systems compared to symmetric systems and rise is more as the cluster size increases. Earlier, Singh *et al.* have observed such behavior, greater rise for heavier fragments than lighter ones, in their study of symmetric reactions in the incident energy range of 50 MeV/nucleon and 1 GeV/nucleon [252]. In their study, different fragments also showed power law dependence as a function of system masses.

Now, let us understand the results, first, for symmetric systems (η_A=0.0). At fixed incident energy, the systems with lesser number of nucleons dilutes faster compared to the systems with larger number of nucleons. Therefore, more number of nucleons exist close to each other in phase space as the total system mass increases. This leads to the formation of more number of clusters with masses 2 to 4. Ultimately, all the ratios increases with increase in the total system mass. The increase in the slopes for $< A = 4/p >$, $< A = 3/p >$ and $< A = 2/p >$ can also be explained on the basis of the above discussion i.e., more dense is the system, greater will be the possibility that the clusters with masses 2, 3 and 4 forms. The above discussed role that the expansion of system depends on source size is well established for multifragmentation and collective flow in experiments and theory [71, 251].

Further, let us understand the prominent increase for lower mass asymmetries compared to higher mass asymmetries e.g., for η_A =0.0, 0.1, 0.3, 0.5 and 0.7 the slopes (exact upto three decimals) for $< A = 2/p >$ are 0.04 (0.038), 0.03 (0.030), 0.03 (0.026), 0.03 (0.026) and 0.02 (0.022), respectively, for $< A = 3/p >$ the values are 0.13, 0.12, 0.011, 0.10 and 0.07, respectively, and $< A = 4/p >$ the values are 0.24, 0.22, 0.20, 0.13 and 0.12, respectively. We avoid to write error bars during discussion to keep the discussion more clear. Note that the trends of slopes are similar in all the cases. To understand these trends of ratios, one must know the fact that for fixed total system mass and constant incident energy the greater share of energy is used as thermal in case of reactions with larger mass asymmetries. The larger temperature of the system causes the lesser

abundance of lighter clusters. On the other hand in case of symmetric reactions the larger share of energy is in the form of compression causing rapid expansion and lower temperature leads to larger number of light bound clusters. For fixed beam energy of 800 MeV/nucleon, Nagamiya *et al.* showed similar results for the reactions of C+C, Ne+NaF, Ar+KCl, Ne+Cu, C+Pb, Ne+Pb and Ar+Pb [248]. They reported the slopes of 0.36 and 0.8 for the ratios of d/p and t/p, respectively. It is important to mention here that the present calculated slopes differ from the one reported by them due to the difference in the methods to vary mass asymmetries. Danielewicz and Bertsch have also presented such results in the framework of cascade model [249].

5.5.4 Beam energy dependence of entropy production

Let us now understand the variation of ratios of $< A = 2/p >$, $< A = 3/p >$ and $< A = 4/p >$ at different beam energies. In particular, we present results at 600, 800 and 1000 MeV/nucleon. The results are displayed in Figs. 5.5-5.7. We have already discussed the results at 400 MeV/nucleon in Fig. 5.4. Symbols have the same meaning as in Fig. 5.4. If we compare Figs. 5.4 to 5.7, we found that all the ratios decrease in magnitude with increase in beam energy for fixed system mass and mass asymmetry. This is due to the reason that as the density of the phase-space decreases the yield of bound fragments also decreases J. Kapusta has also obtained similar results in his theoretical study [253]. We also note that the decrease of ratios as a function of the beam energies is more pronounced for symmetric systems (e.g., ^{40}Ca+^{40}Ca) than for the asymmetric systems (^{11}B+^{69}As). These trends are consistent with the observations of Nagamiya *et al.* in Ref. [248]. They have reported the trends for the system of Ne+NaF and Ne+Pb in the incident energy range of 400 MeV/nucleon to 2.1 GeV/nucleon. The beam energy dependence arises through the terms freeze out density and temperature. Since these two quantities do not depend strongly on the projectile and target masses, the different beam energy dependence of the systems with different mass asymmetries are easy to explain.

For symmetric systems (η_A=0.0), the slopes of $< A = 2/p >$ at incident energies of 400, 600, 800 and 1000 MeV/nucleon are 0.04, 0.17, 0.19 and 0.22, respectively, of $< A = 3/p >$ are 0.13, 0.32, 0.39 and 0.46, respectively, of $< A = 4/p >$ are 0.24, 0.52, 0.65 and 0.74, respectively. For asymmetric systems (η_A=0.7), the slopes of $< A = 2/p >$ at incident energies of 400, 600, 800 and 1000 MeV/nucleon are 0.02, 0.08, 0.12 and 0.14, respectively, of $< A = 3/p >$ are 0.07, 0.15, 0.21 and 0.22, respectively, of $< A = 4/p >$

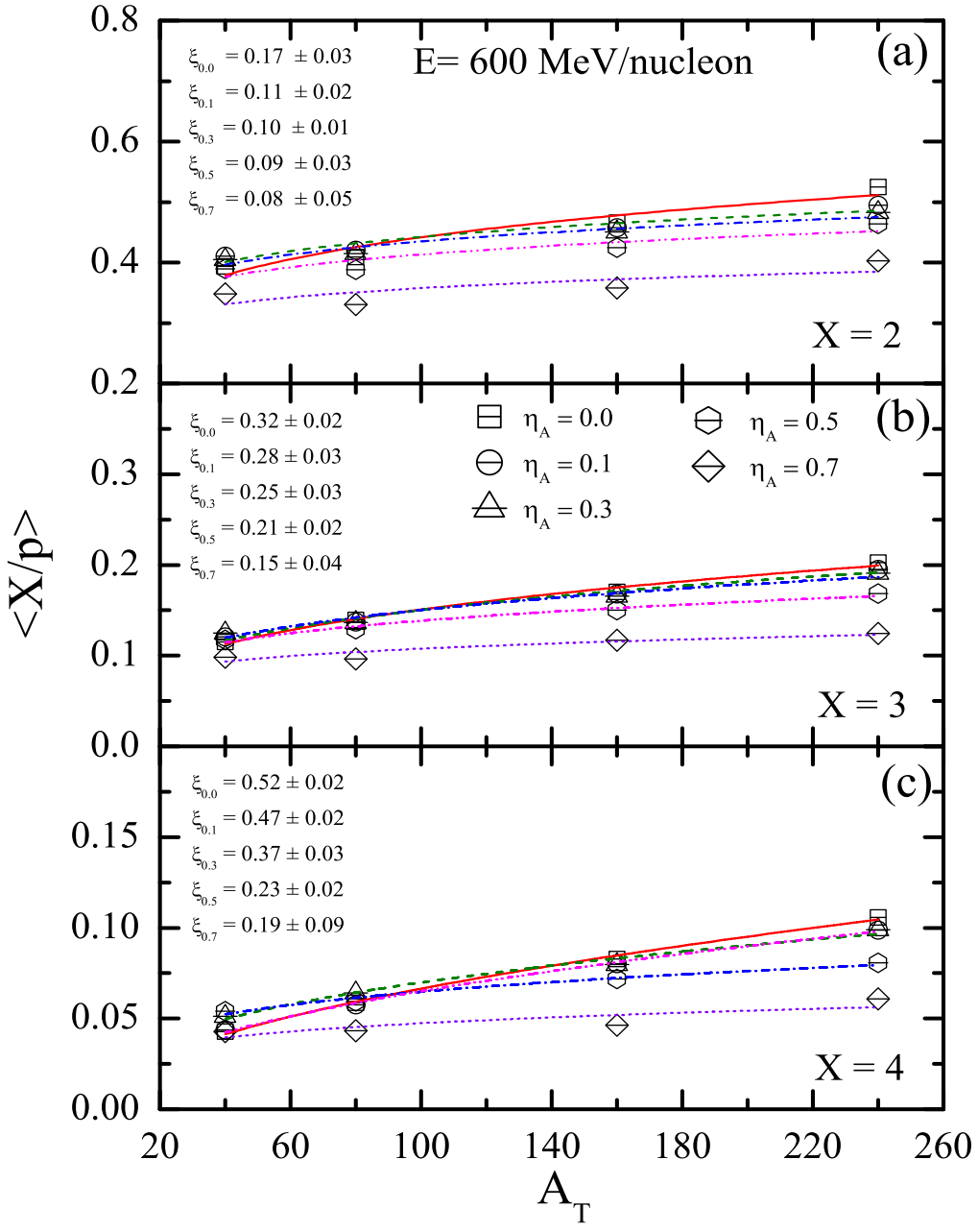

Figure 5.5: Same as Fig. 5.4, but at incident energies of 600 MeV/nucleon.

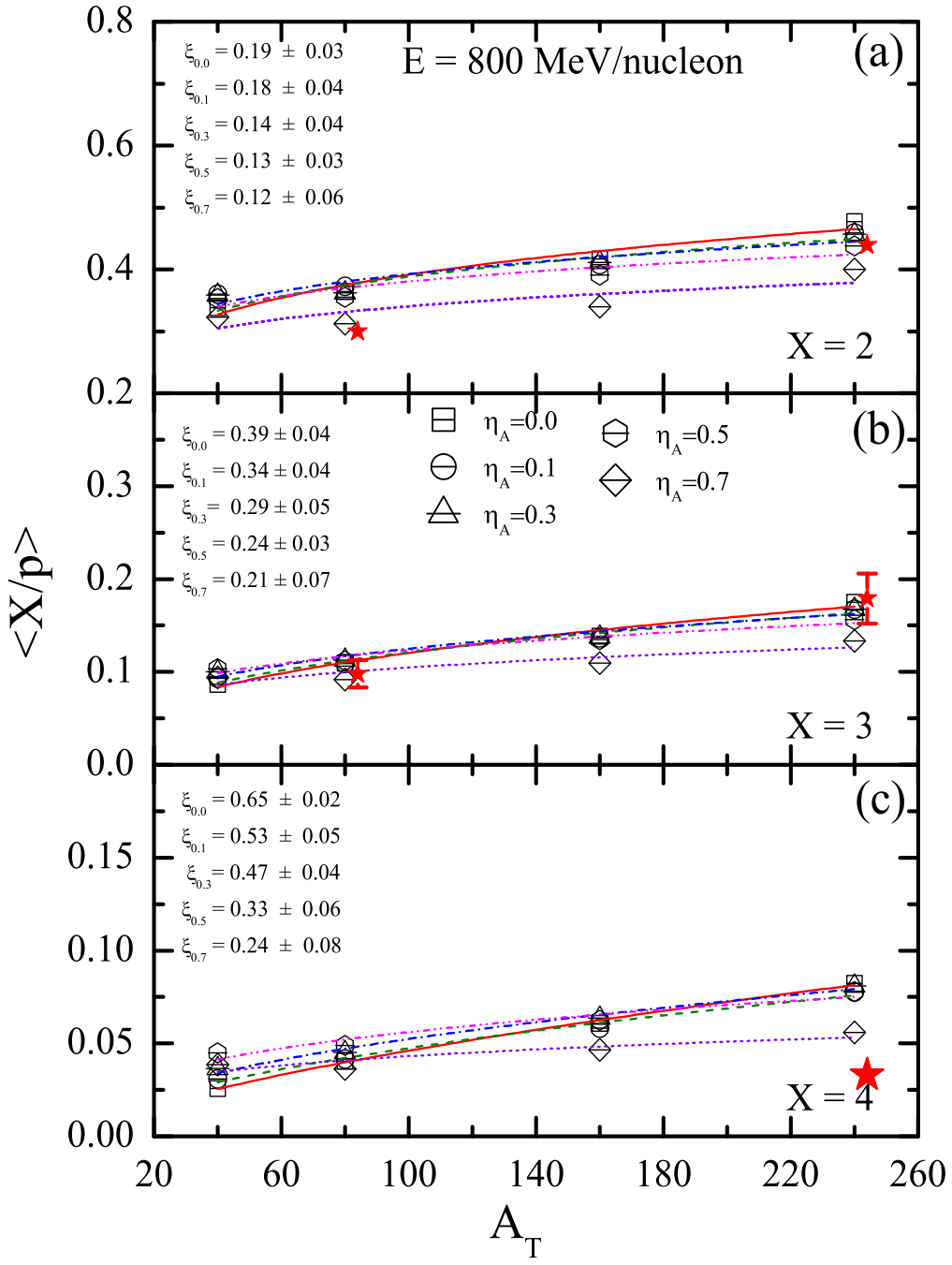

Figure 5.6: Same as Fig. 5.4, but at incident energies of 800 MeV/nucleon. Here, stars represent the experimental data for Ne+Cu and Ar+Pb at an incident energies of 800 MeV/nucleon [248].

are 0.12, 0.19, 0.24 and 0.29, respectively. Therefore, the slope values increases as one increases the incident energy for fixed mass asymmetry value. Qualitatively, the observed behavior could be explained as following: as we increase the beam energy, a larger phase-space volume will be opened up. Since formation of composite fragments is less likely for larger phase-space volumes, we expect smaller ratios for (A=2)/p, (A=3)/p, and (A=4)/p as the incident energy is increased. Such a tendency is clearly seen both for symmetric and asymmetric systems. Also, note that the increase in incident energy reduces the phase space density in expansion phase. The reduction is more prominent for lighter system masses compared to heavier ones. Thus, the rising nature of the ratios continues to appear even for largest incident energies. In asymmetric system, slow composite fragments could be produced more copiously because they tend to originate in the target. Since the spectra of the target fragments do not have strong beam dependence, we could expect less beam energy dependence for heavier mass targets causing the increase in the slopes. We have also shown the results in tabular form in Table 5.1. One can clearly understand the trends from there also.

Next, one is obviously curious to know whether the present results for asymmetric reactions is consistent with experimental observations or not. Keeping this aspect into mind, we have displayed the experimental data (see stars) for higher asymmetries for Ne+Cu and Ar+Pb at incident energy of 800 MeV/nucleon [248] (displayed in Fig. 5.8). From the figure, we can see the consistency between the experimental data and the theoretical calculations. We would also want to mention here that for the same reactions Danielewicz and Bertsch failed to explain the ratios of d/p [249]. This is the first ever calculation, where dynamical models are so close to the experimental results of light particle ratios for asymmetric reactions. At the same time, one can see a rise of ratios in experimental data with increase in system mass for incident energy of 800 MeV/nucleon [248]. Also, the present trends of ratios as a function of incident energy are in accordance with the experimental observations [248]. This consistency also reflects the success of the present model to explain the physics of asymmetric reactions. One can find the comparison between theoretical and experimental data for symmetric reactions in wide incident energy domain in the framework of the present model in Ref. [51, 52].

5.5.5 Variation of deuteron like clusters and deuteron-to-proton ratio with mass asymmetry

Now, let us understand the deuteron like clusters ($< d_{like} >$) and deuteron-to-proton ($< R_{dp} >$) ratios for different mass asymmetries in the incident energy range of 400 to 1000 MeV/nucleon. The results of $< d_{like} >$ and $< R_{dp} >$ are shown in Figs. 5.8 and 5.9, respectively. Symbols have same meaning as in previous figures.

From Fig. 5.8, we see that the values of d_{like} clusters increase with the increase in system masses for all mass asymmetries and for all incident energies. Here, d_{like} clusters are calculated using the eq. 5.8. In this equation, one uses the yields of clusters with masses 2, 3, and 4 on event-by-event basis. Therefore, the rise which was seen for yields of light mass clusters add up to make the difference in slopes of symmetric and asymmetric reactions more prominent. At incident energy of 400 MeV/nucleon, the increase in slopes is sharp in symmetric reactions compared to asymmetric ones. The slopes of $< d_{like} >$ clusters is 0.69, 0.69, 0.68, 0.65 and 0.64 for the mass asymmetry values of 0.0, 0.1, 0.3, 0.5 and 0.7, respectively.

Also, the slopes of ratios changes with the increase in the incident energy e.g., for η_A =0.0, the slopes of power law fit for $< A = 2/p >$ changes from 0.04 to 0.22, for $< A = 3/p >$ changes from 0.13 to 0.46, for $< A = 4/p >$ changes from 0.24 to 0.74 and for $\eta_A = 0.7$, the slope for $< A = 2/p >$ changes from 0.02 to 0.14, for $< A = 3/p >$ changes from 0.07 to 0.22, for $< A = 4/p >$ changes from 0.12 to 0.29 for incident energy change from 400 to 1000 MeV/nucleon. These change in the slopes are clear demonstration that the light cluster formation is greatly influenced by the change in the mass asymmetry of the reaction. The above results are easy to understand with the help of previously discussed results. Again, as discussed earlier, the opening of phase space (or decrease in phase space density) and temperature difference in symmetric and asymmetric systems contribute to the change in slopes.

In Fig. 5.9, we have displayed the results of deuteron-to-proton ratios $< R_{dp} >$ for different mass asymmetries at incident energies of 400, 600, 800 and 1000 MeV/nucleon. Interestingly, at incident energy of 400 MeV/nucleon, the slopes of $< R_{dp} >$ decreases gradually if one moves from symmetric to asymmetric reactions. The slopes of power law fit are 0.17, 0.10, 0.9, 0.08 and 0.07 for the mass asymmetries of 0.0, 0.1, 0.3, 0.5 and 0.7, respectively. This decrease is associated with the number of free protons and bound

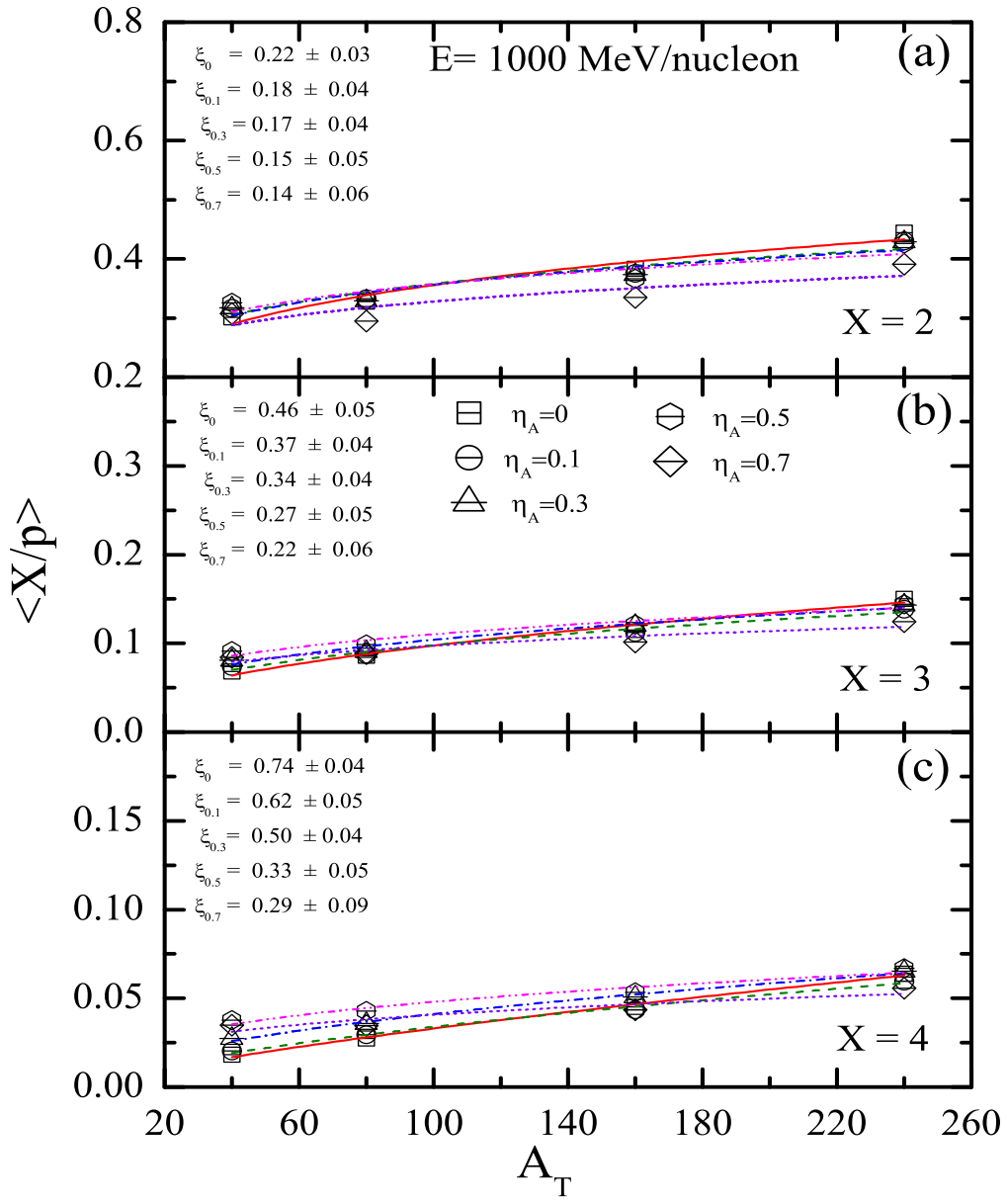

Figure 5.7: Same as Fig. 5.4, but at an incident energy of 1000 MeV/nucleon.

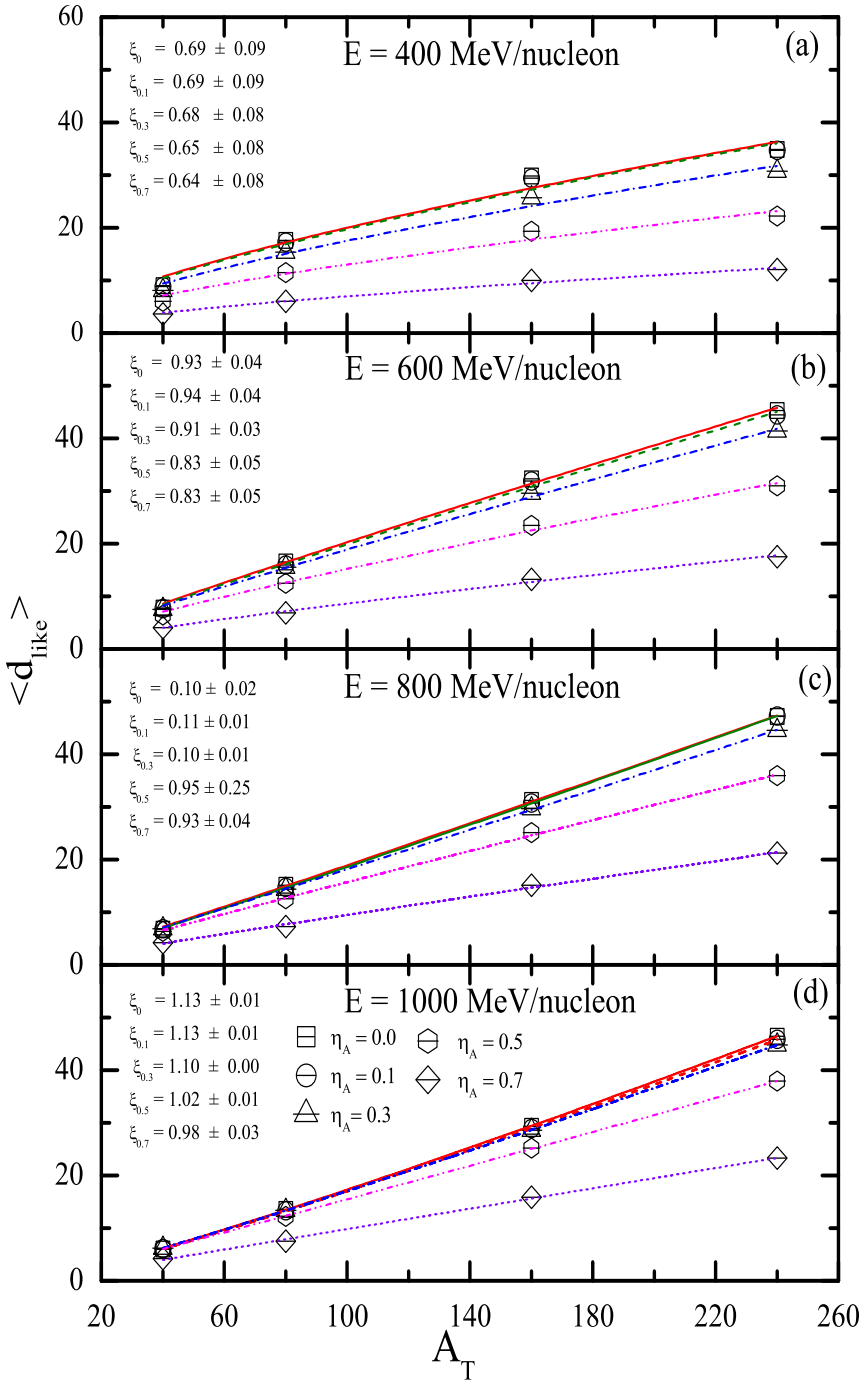

Figure 5.8: The $< d_{like} >$ clusters are displayed at incident energies of 400, 600, 800 and 1000 MeV/nucleon for various mass asymmetries (from top to bottom).

Table 5.1: Slopes of the power law fit (ξ) for the ratios of $< (A = 2)/p >$, $< (A = 3)/p >$, $< (A = 4)/p >$, $< d_{like} >$ clusters and deuteron-to-proton R_{dp} ratio at incident energies of 400, 600, 800 and 1000 MeV/nucleon. The results are shown for all mass asymmetry values ranging from 0.0 to 0.7 for constant system masses of 40, 80, 160 and 240 units.

Mass Asymmetry (η_A)	$< A = 2/p >$	$< A = 3/p >$	$< A = 4/p >$	d_{like}	R_{dp}
E = 400 MeV/nucleon					
0.0	0.04±0.02	0.13±0.01	0.24±0.02	0.69±0.09	0.17±0.01
0.1	0.03±0.01	0.12±0.01	0.22±0.03	0.69±0.09	0.10±0.00
0.3	0.03±0.02	0.11±0.06	0.20±0.02	0.68±0.08	0.09±0.01
0.5	0.02±0.03	0.10±0.04	0.13±0.04	0.65±0.08	0.08±0.01
0.7	0.02±0.04	0.07±0.04	0.12±0.03	0.64±0.08	0.07±0.03
E = 600 MeV/nucleon					
0.0	0.17±0.03	0.32±0.02	0.52±0.02	0.93±0.04	0.24±0.03
0.1	0.11±0.02	0.28±0.03	0.47±0.02	0.94±0.04	0.18±0.02
0.3	0.10±0.01	0.25±0.03	0.37±0.03	0.91±0.03	0.16±0.02
0.5	0.09±0.03	0.21±0.02	0.23±0.02	0.83±0.05	0.14±0.02
0.7	0.08±0.05	0.15±0.04	0.19±0.09	0.82±0.04	0.13±0.04
E = 800 MeV/nucleon					
0.0	0.19±0.03	0.39±0.04	0.65±0.02	1.05±0.02	0.28±0.03
0.1	0.18±0.04	0.34±0.04	0.53±0.05	1.06±0.01	0.22±0.03
0.3	0.14±0.04	0.29±0.05	0.47±0.04	1.03±0.01	0.21±0.02
0.5	0.13±0.03	0.24±0.03	0.33±0.06	0.95±0.03	0.17±0.03
0.7	0.12±0.06	0.21±0.07	0.24±0.08	0.92±0.04	0.16±0.05
E = 1000 MeV/nucleon					
0.0	0.22±0.03	0.46±0.05	0.74±0.04	1.13±0.01	0.30±0.03
0.1	0.18±0.04	0.37±0.04	0.62±0.05	1.12±0.01	0.24±0.03
0.3	0.17±0.04	0.34±0.04	0.50±0.04	1.10±0.00	0.22±0.03
0.5	0.15±0.05	0.27±0.05	0.33±0.05	1.02±0.01	0.18±0.04
0.7	0.14±0.06	0.22±0.06	0.29±0.09	0.98±0.03	0.17±0.05

fragments. The results here follows the same trends as seen in previous cases i.e., with the increase in mass asymmetry the slopes of power law fit decreases at fix incident energy. But, if one compare the slopes with the slopes of $< d_{like} >$ clusters, the slopes are less shaper for all mass asymmetry values at a given incident energy.

Further, if one compares the values of $< R_{dp} >$ for different asymmetries at different incident energies, the slopes are found to increase with rise in the incident energy. The slopes of power law fits, for η_A=0.0, varies from 0.17 to 0.30, whereas, for η_A=0.7, varies from 0.07 to 0.17 for change in incident energy from 400 to 1000 MeV/nucleon. Again, as the R_{dp} is calculated using deuteron-like and proton-like clusters, therefore, the results here are mere image of the earlier results.

5.5.6 Entropy production for various mass asymmetries

As discussed in section 5, the R_{dp} ratios are used to calculate the entropy production in heavy-ion collisions. Here, the values of R_{dp} are used to calculate entropy using the eq. 5.5 for the reactions with various mass asymmetries at incident energies of 400, 600, 800 and 1000 MeV/nucleon.

In Fig. 5.10, the entropy per nucleon is plotted for incident energies of 400, 600, 800 and 1000 MeV/nucleon and for the reactions with total system masses equal to 40, 80, 160 and 240 units. The mass asymmetry values lies between 0.0 and 0.7. From the figure, we see that the entropy per nucleon remains almost constant for all mass asymmetries between 0.0 to 0.7 at incident energies of 400, 600, 800 and 1000 MeV/nucleon. Typically, the variation in the entropy values for all cases is between 0.3-0.5 level at all incident energies. These variations are of the same order as seen for increase in incident energy. To see consistency with experimental data, we have also shown the entropy values for the reactions of ^{40}Ca+^{40}Ca at incident energies of 400 and 1050 MeV/nucleon, and ^{93}Nb +^{93}Nb at incident energies of 400 and 650 MeV/nucleon. We see that our calculations are consistent with the experimental results at both incident energies for both system masses. Thus, we find that for variation in system mass and asymmetry of a reaction, the individual yields and their ratios change, but the entropy per nucleon remains constant. These results can also be understood by looking at the $< R_{dp} >$ ratios in Fig. 5.9. In particular, the following two aspects can be observed:

- The variation in $< R_{dp} >$ is in between 0.3 range only, for a given mass asymmetry

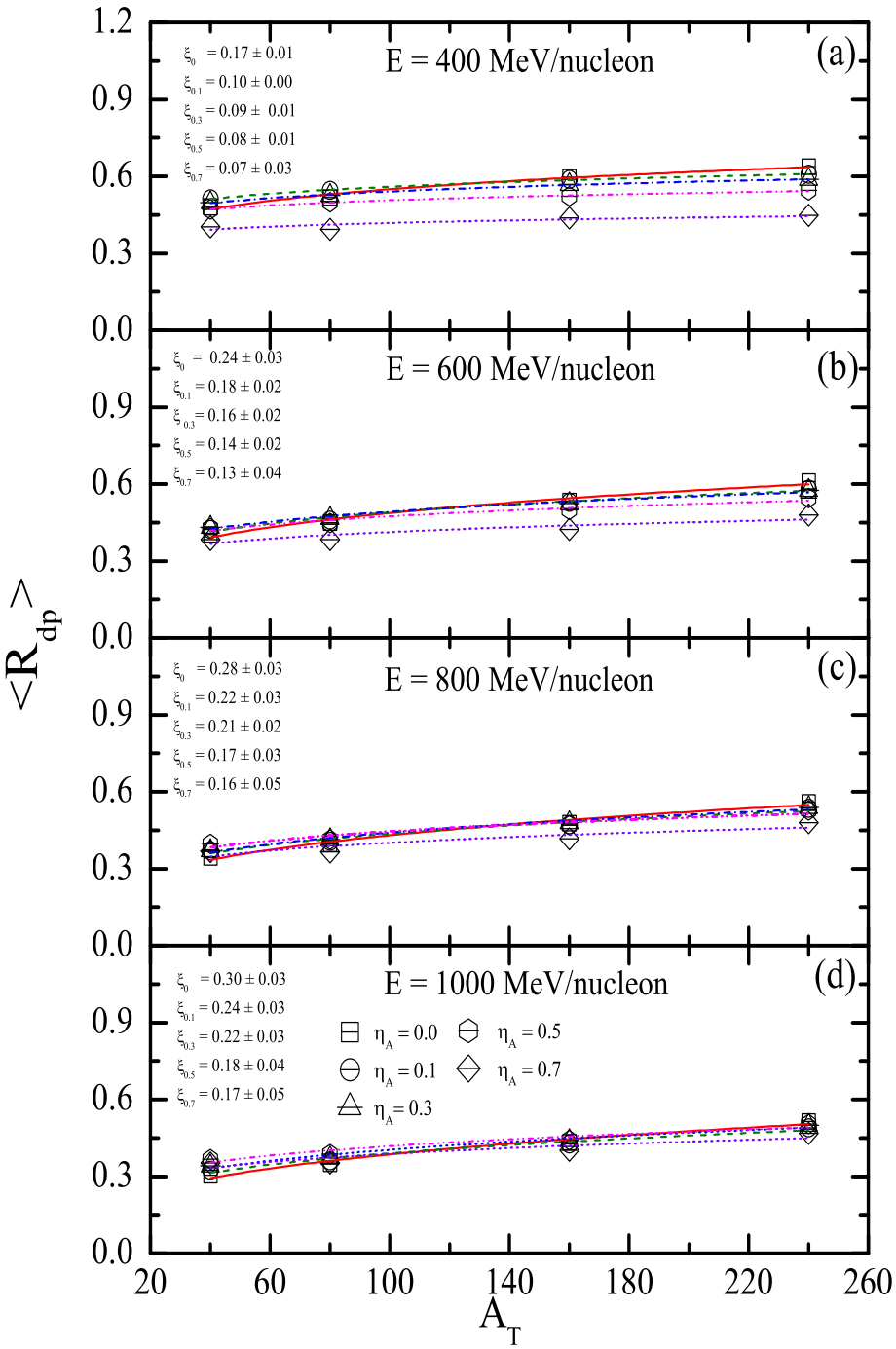

Figure 5.9: The deuteron-to-proton ratio ($< R_{dp} >$) is displayed as a function of system masses for mass asymmetries of 0.0, 0.1, 0.3, 0.5 and 0.7 at incident energies of 400, 600, 800 and 1000 MeV/nucleon.

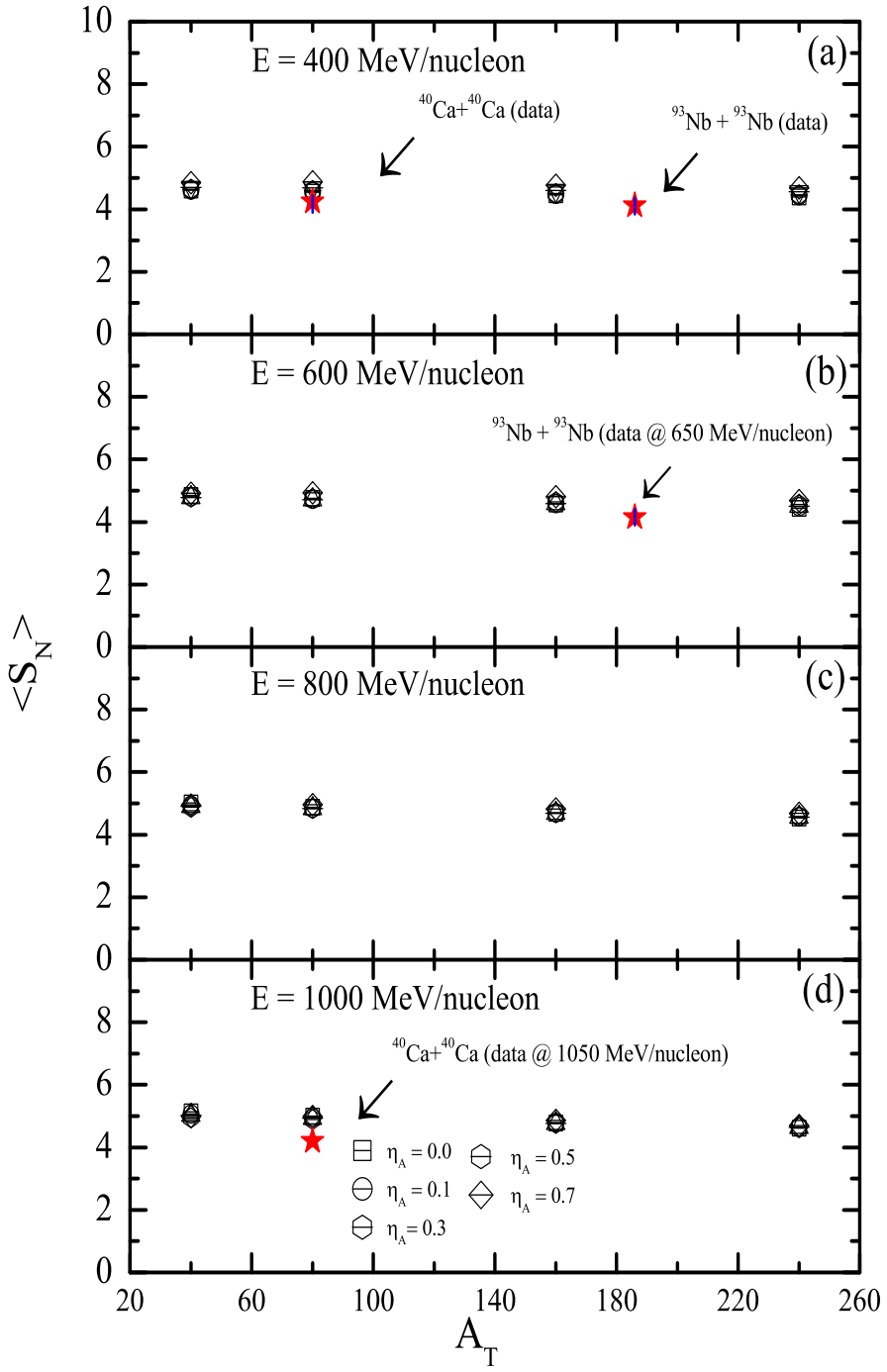

Figure 5.10: The entropy production per nucleon ($< S_N >$) as a function of total system mass is displayed for mass asymmetry values of 0.0, 0.1, 0.3, 0.5 and 0.7 at incident energies of 400, 600, 800 and 1000 MeV/nucleon. Stars represent the experimental data [55].

for all incident energies.

- The variation of incident energy changes the $< R_{dp} >$ from ~ 0.45 to ~ 0.30 for systems with total system mass 40, and from ~ 0.50 to ~ 0.45 for systems with total mass 240.

One can see the variation is not that drastic that it can influence results within the formalism to calculate entropy (see eq. 5.5). Thus we conclude that entropy production in heavy-ion collisions remains constant for all system masses with mass asymmetries between 0.0 to 0.7 and in the incident energy range of 400 to 1000 MeV/nucleon.

5.6 Summary

First, we have demonstrated the role of various technical parameters of clusterization algorithms such as clusterization radius and different clusterization algorithms on the onset of vaporization. We observed that the technical parameters do not alter the results of vaporization and also close to the experimental observations. Later, the property of light particles to thermalize the nuclear matter instigates one to study entropy production as the important probe for asymmetric reactions. The study done includes the role of mass asymmetries on ratios of light mass clusters and entropy production at different incident energies of 400, 600, 800 and 1000 MeV/nucleon. The study was conducted using various mass asymmetries for total system masses of 40, 80, 160 and 240 units. The role of both mass asymmetry and incident energy is seen for ratios of light clusters. Also, the ratios are found to be consistent with the available experimental data and earlier calculations. Lastly, the entropy production is found to be independent of all mass asymmetries and system masses.

Chapter 6

Summary of the thesis and outlook

In this thesis, the phenomenon of multifragmentation and various features associated with it was presented. Both Quantum Molecular Dynamics (QMD) model and its isospin variant was used to generate the phase space of nucleons from the beginning to the end of the reaction. Further, the phase space of nucleons is clusterized using various clusterization algorithms.

In **chapter1**, we introduced the phase transitions in nuclear matter. We also correlated phenomenon of multifragmentation (emission of multi-particles) with various stages of phase transitions in nuclear matter. Then, we presented details of available experimental facilities and theoretical modelling done to study multifragmentation.

In chapter 2, we discussed the methodology of Quantum Molecular Dynamics (QMD) model and Isospin-dependent Quantum Molecular Dynamics (IQMD) model in detail which is used in the present study.

In **chapter 3**, we discussed various spatial based clusterization algorithms such as MST method and its variants. We extracted the critical exponent τ/λ to study the point of onset of multifragmentation or critical energy point. We also calculated various observables such as S_2, γ_2 and Z_{max2} to study the first-order phase transition in nuclear matter. Our results validated the utility of MST method and its any extension to identify fragments as results were found insensitive to the choice of algorithm.

In **chapter 4**, we put forward the idea of using energy based clusterization algorithm

to overcome the shortcomings of MST method (or any of its variant). We discussed the need and importance of energy based clusterization algorithm i.e., SACA. Then we confronted our calculations with the available experimental results that includes the critical parameter τ (λ) and various other observables such as S_2, γ_2 and Z_{max2}. Our detailed study spans over both light and heavy systems. Our detailed study revealed the capability of SACA method to very well reproduce exactly the energy of minima in power law exponent as shown in experimental data.

In **chapter 5**, we try to associate emission of light particles to study onset of vaporization in nuclear matter. We presented calculations using various clusterization algorithms and its role on the onset of vaporization. Further, we discussed the significance of emission of light particles at various stages of the reaction and associate it to study entropy production. This study was done using IQMD model. Our study spans over the entire range of mass asymmetric reactions and also different total system masses. The entropy was found independent of mass asymmetry and total system mass. The results of both IQMD and QMD model were also compared. The entropy was found independent of both models also.

Summarizing, we have attempted to study phase transitions that nuclear matter undergo at various stages of the reaction with incident energy. We have done this study using complete range of available clusterization algorithms. We have shown that these algorithms provide realistic structure of fragments. Our results showed that, although the MST provide strong evidence to study liquid-gas phase transition in nuclear matter at the later stages of the reaction, the SACA can give these indications more accurately and precisely at the early stages of the reaction. In future scope, it will be very interesting to introduce new parameters to study phase transitions in nuclear matter. We have also shown the systematics of light particles near/after the complete vaporization of system.

6.1 Outlook

We have investigated the role of various clusterization algorithms on the phase-transitions in nuclear matter and related phenomenon, still there are numerous challenges yet to be solved. The most important challenge is to study role of varying various model ingredients, mass asymmetry and N/Z ratios on phase transition. Despite the fact that various observables have been put forward as probe in the literature which give information about

dynamics involved with phase-transitions in nuclear matter but, we need to search for new observables to better understand the physics related to phase-transitions in nuclear matter. In chapters 3 and 4, we studied the role of various clusterization algorithms on liquid-gas phase transition. This study can be extended by studying the complete range of asymmetric reactions and by defining new observables to define the existence of liquid-gas phase transition. In chapter 5, we have associated the emission of light particles to the entropy production and onset of vaporization. It would be quite interesting to extend it to study role for asymmetric reactions and N/Z ratio on these phenomena.

Bibliography

[1] D. J. Champion *et al.*, Science **230**, 1390 (2008).

[2] J. M. Lattimer, C. J. Pethick, M. Prakash, and P. Haensel, Phys. Lett. **66**, 2701 (1991).

[3] G. Bertsch and P. J. Siemens, Phys. Lett. B 1 **126B**, 95 (1983).

[4] R. Nandi and S. Schramm, Phys. Rev. C **95**, 065801(2017).

[5] M. Kardar, *Statistical physics of particles*(Book), Cambridge University Press (2017).

[6] F. Reif, *Fundamentals of Statistical and Thermal physics*(Book), Waveland Press Inc. (2009).

[7] R. K. Patharia, *Statistical Mechanics* (Book), Butterworth-Heinemann (2001).

[8] J. Pochodzalla *et al.*, Phys. Rev. Lett. **75**, 1040 (1995).

[9] M. D. Agostino *et al.*, Nucl. Phys. A, **749**, 55c-64c (2005).

[10] E. P. Prendergast, Ph. D. Thesis, University of London, London (1971).

[11] J. Aichelin, Phys. Rep. **202**, 233 (1991).

[12] B. Borderie and M. F. Rivet, Prog. Part. Nucl. Phys. **61**, 551 (2008).

[13] A. Roy, Current Science **76**, 149 (1999); *ibid.*, Pram. J. Phys. **57**, 659 (2001).

[14] W. F. Henning, *Proceedings of the Particle Accelerator Conference, Potland*, Oregon, **1**, 16 (2003).

[15] P. Spiller *et al.*, *Proceedings of 10th European Particle Accelerator Conference*, Edinburg, UK, p. **24** (2006).

[16] J. J. Thomson, Phil. Mag. **44**, 293 (1897).

[17] E. Rutherford, Phil. Mag. **21**, 669 (1911).

[18] J. Chadwick, Proc. Roy. Soc. (London) A **136**, 692 (1932).

[19] E. D. Bloom *et al.*, Phys. Rev. Lett. **23**, 930 (1969)

[20] J. Breidenbach *et al.*, Phys. Rev. Lett. **23**, 935 (1969).

[21] G. Kaur and M. K. Sharma, Phys. Rev. C **87**, 044601 (2013); Rajni, R. Kumar and M. K. Sharma, *ibid.* C **90**, 044604 (2014); R. Kumari and R. K. Puri, Nucl. Phys. A **933**, 135 (2015).

[22] N. Bohr, Nature **137**, 344 (1936).

[23] V. V. Desai, B. K. Nayak, A. Saxena, S. V. Suryanarayana and R. Capote, Phys. Rev. C **92**, 014609 (2015); T. Ichikawa *et al.*, *ibid.*, C **92**, 064604 (2015); H. Naik *et al.*, Nucl. Phys. A **941**, 16 (2015).

[24] R. Kumar and M. K. Sharma, Phys. Rev. C **85**, 054612 (2012); L. Ma *et al.*, *ibid.* C **91**, 051302(R) (2015); A. Kaur, S. Chopra and R. K. Gupta, *ibid.* C **91**, 064601 (2015); V. Y. Denisov, O. I. Davidovskaya and I. Y. Sedykh, *ibid.* C **92**, 014602 (2015).

[25] J. M. Akkermans and H. Gruppelaar, Phys. Rev. Lett. **157**, 95 (1985).

[26] P. K. Rath *et al.*, Phys. Rev. C **88**, 064322 (2013); *ibid.* C **87**, 014301 (2013).

[27] L. C. Vaz, J. M. Alexander and G. R. Satchler, Phys. Rep. **69**, 373 (1981).

[28] V. I. Zagrebaev, Phys. Rev. C **64**, 034606 (2001).

[29] R. Kumari *et al.*, Nucl. Phys. A **917**, 85 (2013), X. J. Bao, Y. Gao, J. Q. Li and H. F. Zhang, Phys. Rev. C **92**, 014601 (2015).

[30] J. Adams *et al.*, Nucl. Phys. A **757**, 102 (2005).

[31] C. Y. Wong, *Introdution to high-energy heavy-ion collisions, World Scientific,* Singapore (1994).

[32] J. P. Bondorf, A. S. Botvina, A.S. Iljinov, I. N. Mishustin and K. Sneppen, Phys. Rep. **257**, 133 (1995).

[33] J.P. Bondorf, Journal de Physique **37**, C5-195 (1976); J. P. Bondorf, *Proceeding of the EPS topical conference on large amplitude collective nuclear motions, Keszthely, Hungary*, June 1979.

[34] B. Jakobsson, G. Jönsson, B. Lindkvist and A. Okarsson *et al.*, Z. Phys. A **307**, 293 (1982).

[35] B. Jakobsson *et al.*, Nucl. Phys. A **509**, 195 (1990).

[36] W. Stöcker and J. Burzlaff *et al.*, Nucl. Phys. A 202, 265 (1973).

[37] D. G. Ravenhall, C. J. Pethick and J. M. Lattimer, Nucl. Phys. A **407**, 571 (1983); D. G. Ravenhall, C. J. Pethick and J. R. Wilson, Phys. Rev. Lett. **50**, 2066 (1983).

[38] B. Friedman and V. R. Pandharipande, Nucl. Phys. A **361**, 502 (1981); T. J. Schlagel and V. R. Pandharipande, Phys. Rev. C **36**, 162 (1987).

[39] G. Sauer, H. Chandra and U. Mosel, Nucl. Phys. A **264**, 221 (1976); P. Bonche, S. Levit and D. Vautherin, Nucl. Phys. A **428**, 95 (1984); *ibid.* A **427**, 278 (1984).

[40] E. Suraud, Nucl. Phys. A **462**, 109 (1987); H. Müller and R.M. Dreizler, *ibid.*, A **563**, 649 (1994).

[41] B. D. Serot and J. D. Walecka, Adv. Nucl. Phys. **16**, 1 (1986).

[42] W. A. Küpper, G. Wegmann and E.R. Hilf, Ann. of Phys. **88**, 454 (1974); Y. B. Ivanov *et al.*, Fiz. Sov. J. Nucl. Phys. **34**, 45 (1981).

[43] C. A. Ogilvie *et al.,* Phys. Rev. Lett. **67**, 1214 (1991).

[44] Y. G. Ma and W. Q. Shen, Phys. Rev. C **51**, 710 (1995).

[45] Y. G. Ma *et al.*, Phys. Rev. C **71**, 054606 (2005).

[46] T. Li *et al.,* Phys. Rev. C **49**, 1630 (1994).

[47] A. Sharma, A. Bharti, S. Gautam and R. K. Puri, Nucl. Phys. A **945**, 95 (2016).

[48] A. Sharma and A. Bharti, Eur. Phys. J. A **52**, 42 (2016).

[49] C. Williams *et al.,* Phys. Rev. C **55**, R2132 (1997).

[50] S. D. Gupta and J. Pan, Phys. Rev. C **53**, 1319 (1996).

[51] Y. K. Vermani and R. K. Puri, Nucl. Phys. A **847**, 243 (2010).

[52] S. Kaur and R. K. Puri, Phys. Rev. C **89**, 057603 (2014); *ibid.,* C **90**, 037602 (2014).

[53] P. J. Siemens and J. I. Kapusta, Phys. Rev. Lett. **43**, 1486 (1979).

[54] G. Bertsch and J. Cugnon, Phys. Rev. C **24**, 2514 (1981); G. F. Bertsch, Nucl. Phys. A **400**, 221 (1983).

[55] K. G. R. Doss *et al.*, Phys. Rev. C **32**, 116 (1985); *ibid.*, C **37**, 163 (1988).

[56] A. Fokin *et al.,* Phys. Rev. C **60**, 024601 (1999).

[57] G. F. Peasle*et al.*, Phys. Rev. C **49**, R2271 (1994).

[58] J. E. Finn *et al.,* Phys. Rev. Lett. **49**, 1321 (1982).

[59] G. Peilert *et al.,* Phys. Rev. C **39**, 1402 (1989).

[60] S. R. Souza *et al.,* Nucl. Phys. A **571**, 159 (1994).

[61] J. Aichelin, A. Rosenhauer, G. Peliert, H. Stocker, and W. Greiner, Phys. Rev. Lett. **58**, 1926 (1987).

[62] H. Stocker *et al.*, Nucl. Phys. A **400**, 63 (1983).

[63] B. V. Jacak *et al.,* Phys. Rev. Lett. **51**, 1846 (1983); B. V. Jacak, H. Stocker, and G. D. Westfal, Phys. Rev. C **29**, 1744 (1984).

[64] R. Trockel *et al.,* Phys. Rev. C **38**, 1 (1988).

[65] C. Hartnack, H. Oeschler, Y. Leifels, E. L. Bratkovskaya and J. Aichelin, Phys. Rep. **510**, 119 (2012).

[66] B. A. Li, L. W. Chen and C. M. Ko, Phys. Rep. **464**, 113 (2008).

[67] W. K. Wilson, *Ph.D. Thesis, Michigan State University* (1991).

[68] L. Phair *et al.*, Phys. Lett. B **285**, 10 (1992).

[69] J. K. Dhawan and R. K. Puri, Phys. Rev. C **75**, 057601 (2007).

[70] J. Hubele *et al.*, Phys. Rev. C **46**, R1577 (1992).

[71] A. Schüttauf *et al.*, Nucl. Phys. A **607**, 457 (1996).

[72] J. P. Alard *et al.*, Phys. Rev. Lett. **69**, 889 (1992).

[73] D. Cussol *et al.*, Phys. Rev. C **65**, 044604 (2002).

[74] S. Piantelli *et al.*, Phys. Rev. C **74**, 034609 (2006); S. Piantelli *et al.*, *ibid.* C **78**, 064605 (2008).

[75] G. Peilert, H. Stocker and W. Greiner *et al.*, Rep. Prog. Physics **57**, 533 (1994).

[76] O. V. Lozhkin and N. A. Perfilov, Sov. Phys. JETP **4**, 790 (1957); N. A. Perfilov, O. V. Lozhkin, and V. P. Shamov, Sov. Phys. Usp. **3**, 1 (1960)].

[77] L. G. Moretto, D. N. Delis and G. J. Wozniak, Phys. Rev. Lett. **71**, 3935 (1993).

[78] L. Phair *et al.*, Phys. Rev. Lett. **75**, 213 (1995).

[79] T. C. Sangster *et al.*, Phys. Rev. C **46**, 1404 (1992).

[80] D. R. Bowman *et al.*, Nucl. Phys. A **523**, 386 (1991).

[81] P. R. Chomaz *et al.*, Nucl. Phys. A **551**, 508 (1993).

[82] A. Insolia *et al.*, Phys. Rev. C **61**, 044902 (2000).

[83] N. T. Porile *et al.,* Phys. Rev. C **39**, 1914 (1989).

[84] M. B. Tsang *et al.*, Phys. Rev. Lett. **71**, 1502 (1993).

[85] R. Sun *et al.*, Phys. Rev. C **61**, 061601 (2000).

[86] R. T. de Souza *et al.*, Phys. Lett. B **268**, 6 (1991).

[87] T. Li *et al.*, Phys. Rev. Lett. **70**, 1924 (1992).

[88] W. J. Llope *et al.*, Phys. Rev. C **51**, 1325 (1995).

[89] N. T. B. Stone, W. J. Llope, and G. D. Westfall, Phys. Rev. C **51**, 3157 (1995).

[90] D. Sisan *et al.*, Phys. Rev. C **63**, 027602 (2001).

[91] M. B. Tsang *et al.*, Phys. Rev. Lett. **92**, 062701 (2004).

[92] Y. Zhang *et al.*, Phys. Lett. B **664**, 145 (2008).

[93] T. X. Liu *et al.*, Phys. Rev. C **76**, 034603 (2007).

[94] E. Galichet, M. Colonna, B. Borderie and M. F. Rivet, Phys. Rev. C **79**, 064615 (2009); E. Galichet *et al.*, *ibid.*, C **79**, 064614 (2009).

[95] B. Hong *et al.*, Phys. Rev. C **66**, 034901 (2002).

[96] B. de Schauenburg, *et al.*, GSI Rep. **98**, p. 56 (1997); W. Reisdorf, Nucl. Phys. A **630**, 15 (1998).

[97] M. Begemann-Blaich *et al.*, Phys. Rev. C **48**, 610 (1993).

[98] J. D. Frankland *et al.*, Phys. Rev. C **71**, 034607 (2005); J. D. Frankland et al., Nucl. Phys. A **689**, (2001), Phys. Rev. C **58**, 256 (1998).

[99] W. Loveland *et al.*, Phys. Rev. C **59**, 1472 (1999).

[100] B. Borderie *et al.*, Nucl. Phys. A **734**, 495 (2004).

[101] M. *Ď* Agostino *et al.*, Nucl. Phys. A **699**, 795 (2002).

[102] M. Pichon, *et al.*, Nucl. Phys. A **749**, 93 (2005).

[103] N. Le Neindre *et al.*, Nuc. Phys. A **795**, 47 (2007).

[104] A. I. Warwick *et al.*, Phys. Rev. C **27**, 1083 (1983).

[105] K. Hagel et al., Phys. Rev. C **50**, 2017 (1994).

[106] P. Danielewicz, Phys. Rev. C **51**, 716 (1995).

[107] P. Kreutz *et al.*, Nucl. Phys. A **556**, 672 (1993).

[108] W. -c. Hsi *et al.*, Phys. Rev. Lett. **79**, 817 (1997).

[109] Y. G. Ma , Phys. Rev. C **69**, 031604 (2004).

[110] R. Wada *et al.*, Phys. Rev. C **69**, 044610 (2004).

[111] D. V. Shetty *et al.*, Phys. Rev. C **68**, 054605 (2003): D. V. Shetty, G. A. Souliotis, S. Galanopoulos and S. J. Yenello, Phys. Rev. C **79**, 034603 (2009).

[112] D. V. Shetty, *et al.*, J. Phys. G **36**, 075103 (2009).

[113] D. V. Shetty, S. J. Yenello and G. A. Souliotis, Phys. Rev. C **76**, 024606 (2007); *ibid.*, C **75**, 034602 (2007).

[114] A. S. Botvina *et al.*, Nucl. Phys. A **584**, 737 (1995).

[115] A. Z. Mekijian, Phys. Rev. C **l7**, 1051 (1978).

[116] J. Randrup and S. E. Koonin, Nucl. Phys. A **356**, 223 (1981).

[117] D. Hahn and H. Stocker, Nucl. Phys. A **476**, 718 (1988) .

[118] D. H. E. Gross, Prog. Rep. Phys. **53**, 605 (1990).

[119] L. Satpathy, M. Mishra, A. Das and M. Satpathy, Phys. Lett. B **237**, 181 (1990); S. Pal, S. K. Samaddar and J. N. De, Nucl. Phys. A **608**, 49 (1996); C. B. Das, A. Das, L. Satpathy and M. Satpathy, Phys. Rev. C **53**, 1833 (1996).

[120] M. Colonna, *et al.*, Phys. Lett. B **283**, 180 (1992).

[121] A. Das, M. Mishra, M. Satpathy, and L. Satpathy, J. Phys. G: Nucl. Part. Phys. **19**, 319 (1993); S. Pal, S. K. Samaddar, J. N. De and B. Djerroud, Phys. Rev. C **57**, 3246 (1998).

[122] V. Weisskopf, Phys. Rev. C **52**, 295 (1937).

[123] W. Bauer, U. Post, D. R. Dean and U. Mosel, Nucl. Phys. A, **452**, 699 (1986).

[124] C. B. Das, S. D. Gupta, W. G. Lynch, A. Z. Mekjian and M. B. Tsang, Phys. Rep. **406**, 1 (2005).

[125] G. F. Bertsch and S. D. Gupta, Phys. Rep. **160**, 189 (1988); G. F. Bertsch, H. Kruse and S. D. Gupta, Phys. Rev. C **29**, R673 (1984); J. Aichelin *et al.*, Phys. Lett. B **224**, 34 (1989).

[126] H. Kruse, B. V. Jacak, J. J. Molitoris, G. D. Westfall and H. Stocker, Phys. Rev. C **31**, 1770 (1985); H. Kruse, B. V. Jacak and H. Stöcker, Phys. Rev. Lett. **54**, 289 (1985); J. J. Molitoris and H. Stöcker, Phys. Rev. C **32**, R346 (1985).

[127] C. Grégorie, B. Rémaud, F. Sébille, L. Vinet and Y. Raffray, Nucl. Phys. A **465**, 317 (1987); C. Grégoire, B. Rémaud, F. Śebille and L. Vinet, Phys. Lett. B **186**, 14 (1987); *ibid.*, B **180**, 198 (1986).

[128] A. Bonasera, F. Gulminelli and P. Schuck, Phys. Rev. C **46**, 1431 (1992).

[129] A. Badalá, R. Barbera, A. Bonasera *et al*, Phys. Rev. C **43**, 190 (1991).

[130] B. A. Li and S. J. Yennello, Phys. Rev. C **52**, R1746 (1995).

[131] B. A. Li *et al.*, Phys. Rev. Lett. **76**, 4492 (1996).

[132] A. Ono, H. Horiuchi, T. Maruyama, and A. Ohnishi, Phys. Rev. Lett. **68**, 2898 (1992).

[133] A. Ono, H. Horiuchi, T. Maruyama, and A. Ohnishi, Prog. Theo. Phys. **87**, 1185 (1992).

[134] A. Ono, H. Horiuchi and T. Maruyama, Phys. Rev. C **48**, 2946 (1993); A. Ono and H. Horiuchi, *ibid.* C **51**, 299 (1995).

[135] A. Ono, H. Horiuchi, Prog. Part. Nucl. Phys. **53**, 501 (2004).

[136] J. P. Bondorf, R. Donangelo, I. N. Mishustin, C. J. Pethick, H. Schulz and K. Sneppen, Nucl. Phys. A, **321** (1985).

[137] T. Maruyama, K. Niita and A. Iwamoto, Phys. Rev. C **53**, 297 (1996).

[138] H. Feldmeier, Nucl. Phys. A **515**, 147 (1990); H. Feldmeier and J. Schnack, Prog. Part. Nucl. Phys. **39**, 393 (1997).

[139] N. Wang, Z. Li and X. Wu, Phys. Rev. C **65**, 064608 (2002).

[140] N. Wang *et al.,* Phys. Rev. C **69**, 034608 (2004).

[141] C. Hartnack *et al.,* Eur. Phys. J. A **1**, 151 (1998).

[142] M. Papa, T. Maruyama, and A. Bonasera, Phys. Rev. C **64**, 024612 (2001).

[143] M. Papa, G. Giuliani, A. Bonasera, J. Comp. Phys. **208**, 403 (2005).

[144] R. K. Puri *et al.,* Nucl. Phys. A **575**, 733 (1994).

[145] A. Bohnet*et al.,* Phys. Rev. C **44**, 2111 (1991).

[146] G. Peilert *et al.,* Phys. Rev. C **46**, 1457 (1992).

[147] E. Lehmann, R. K. Puri, A. Faessler, G. Batko and S. W. Huang, Phys. Rev. C **51**, 2113 (1995).

[148] E. Lehmann, R. K. Puri, A. Faessler, T. Maruyama, G. Q. Li, N. Ohtsuka, S. W. Huang, D. T. Khoa, M. A. Matin, Prog. Part. Nucl. Phys. **30**, 219 (1993).

[149] Z. Y. Sun *et al.*, Phys. Rev. C **82**, 051603(R) (2010).

[150] S. A. Bass *et al.*, Prog. Part. Nucl. Phys. **41**, 255 (1998).

[151] A. Dumitru *et al.*, Phys. Rev. C **57**, 3271 (1998).

[152] K. Abdel-Waged, Phys. Rev. C **70**, 014605 (2004).

[153] L. V. Bravina *et al.*, Phys. Rev. C **62**, 064906 (2000).

[154] S. Kumar and R. K. Puri, Phys. Rev. C **58**, 320 (1998).

[155] J. Singh, S. Kumar and R. K. Puri, Phys. Rev. C **63**, 054603 (2001).

[156] S. Kumar and R. K. Puri, Phys. Rev. C **58**, 2858 (1998); S. Goyal and R. K. Puri, Phys. Rev. C **83**, 047601 (2011).

[157] R. Kumar, S. Gautam and R. K. Puri, Phys. Rev. C **89**, 064608 (2014); *ibid.*, J. Phys. G: Nucl. Part. Phys. **43**, 025104 (2016).

[158] C. Dorso and J. Randrup, Phys. Lett. B **301**, 328 (1993).

[159] R. K. Puri, C. Hartnack and J. Aichelin, Phys. Rev. C **54**, R28 (1996); R. K. Puri and J. Aichelin, J. Comput. Phys. **162**, 245 (2000); Y. K. Vermani and R. K. Puri, Eur. Phys. Lett. **85**, 62001 (2009).

[160] H. Stöcker and W. Greiner, Phys. Rep. **137**, 277 (1986).

[161] J. W. Negele, Rev. Mod. Phys. **54**, 913 (1982); F. Sakata, T. Kubo, T. Marumori, K. Iwasawa and Y. Hashimoto, Phys. Rev. C **50**, 138 (1994); D. Lacroix and P. Chomaz, *ibid.*, C **58**, 1604 (1998); A. S. Umar and V. E. Oberacker, Phys. Rev. C **74**, 024606 (2006); S. S. Chandel, S. K. Dhiman and R. Shyam, C **68**, 054320 (2003).

[162] S. Ayik, D. Lacroix and P. Chomaz, Phys. Rev. C **61**, 014608 (1999).

[163] J. Cugnon, Phys. Rev. C **22**, 1885 (1980).

[164] D. Polster *et al.*, Phys. Rev. C **51**, 1167 (1995).

[165] A. Boudard, J. Cugnon, S. Leray and C. Volant, Phys. Rev. C **66**, 044615 (2002); J. Cugnon and P. Henrotte, Eur. Phys. J. A **16**, 393 (2003).

[166] R. Stock et al., Phys. Rev. Lett. **49**, 1236 (1982).

[167] Y. Yariv and Z. Fraenkal, Phys. Rev. C **20**, 2227 (1979); Y. Kitazoe, M. Sano, Y. Yamamura, H. Furutani and K. Yamamoto, *ibid.* C **29**, 828 (1984).

[168] G. F. Bertsch, H. Kruse and S. D. Gupta, Phys. Rev C **29**, 673 (1984).

[169] L. Neise *et al.*, Nucl. Phys. A **519**, 375c (1990); M. Berenguer, C. Hartnack, G. Peilert, H. Stöcker, W. Greiner, J. Aichelin and A. Rosenhauer, J. Phys. G: Nucl. Part. Phys. **18**, 655 (1992).

[170] D. T. Khoa *et al.*, Nucl. Phys. A **542**, 671 (1992); D. T. Khoa *et al.*, Nucl. Phys. A **529**, 363 (1991).

[171] G. Q. Li *et al.*, Nucl. Phys. A **534**, 697 (1991).

[172] J. Aichelin *et al.*, Phys. Rev. C **37**, 2451 (1988).

[173] L. Wilets, Y. Yariv and R. Chestnut, Nucl. Phys. A **301**, 359 (1978); A. R. Bodmer, C. N. Panos and A. D. MacKellar, Phys. Rev. C **22**, 1025 (1980); A. Vicentini, G. Jacucci and V. R. Pandharipande, *ibid.*, C **31**, 1783 (1985).

[174] G. Peilert, J. Randrup, H. Stöcker and W. Greiner, Phys. Lett. B **260**, 271 (1991).

[175] R. K. Puri *et al.,* Nucl. Phys. A **575**, 733 (1994).

[176] J. Cugnon, T. Mizutani and J. Vandermeulen, Nucl. Phys. A **352**, 505 (1981).

[177] H. R. Schmidt and J. Schükraft, J. Phys. G: Nucl. Part. Phys. **19**, 1705 (1993).

[178] Z. Q. Feng, F. S. Zhang, G. M. Jin and X Huang, Nucl. Phys. A **750**, 232 (2005); Z. Q. Feng, G. M. Jin, F. S. Zhang, F. Fu and X. Huang, Chin. Phys. Lett. **22**, 3040 (2005).

[179] Z. Q. Feng, Phys. Lett. B **707**, 83 (2012); Z. Q. Feng, Phys. Rev. C **84**, 024610 (2011).

[180] H. Sorge, H. Stocker and W. Greiner, Ann. Phys. **192**, 266 (1989).

[181] K. Abdel-Waged, Phys. Rev. C **63**, 024618 (2001).

[182] Q. Li, C. Shen, C. Guo, Y. Wang, Z. Li, J. Lukasik and W. Trautmann, Phys. Rev. C **83**, 044617 (2011); Q. Li, Z. Li, S. Soff, M. Bleicher and H. Stöcker, J. Phys. G: Nucl. Part. Phys. **32**, 407 (2006).

[183] A. Ono and J. Randrup, Eur. Phys. J. A **30**, 109 (2006).

[184] N. Itagaki, S. Aoyama, S. Okabe, and K. Ikeda, Phys. Rev. C **70**, 054307 (2004).

[185] J. Jaenicke, J. Aichelin, N. Ohtsuka, R. Linden and A. Faessler, Nucl. Phys. A **536**, 201 (1992).

[186] A. Bohnet, N. Ohtsuka, J. Aichelin, R. Linden and A. Faessler, Nucl. Phys. A **494**, 349 (1989).

[187] C. Hartnack L. Zhuxia, L. Neise, G. Peilert, A. Rosenhauer, H. Sorge, J. Aichelin, H. Stöcker and W. Greiner, Nucl. Phys. A **495**, 303c (1989).

[188] C. Hartnack, J. Aichelin, H. Stöcker and W. Greiner, Mod. Phys. Lett. A **9**, 1151 (1994); C. Hartnack, J. Aichelin, H. Stöcker and W. Greiner, Phys. Lett. B **336**, 131 (1994).

[189] B. J. VerWest and R. A. Arndt, Phys. Rev. C **25**, 1979 (1982).

[190] C. Liewen, F. Fengshou and J. Genming, Phys. Rev. C **58**, 2283 (1998).

[191] L. W. Chen, V. Greco, C. M. Ko and B. A. Li, Phys. Rev. Lett. **90**, 162701 (2003); *ibid.*, Phys. Rev. C **68**, 014605 (2003).

[192] Y. G. Ma, J. Phys. G: Nucl. Part. Phys. **27**, 2455 (2001).

[193] M. Belkacem *et al.*, Phys. Rev. C **54**, 2435 (1996).

[194] J. Pan and S. D. Gupta, Phys. Rev. C **51**, 1384 (1995).

[195] J. Pan, S. D. Gupta, and M. Grant, Phys. Rev. Lett. **80**, 1182 (1998).

[196] W. Lin *et al.*, Phys. Rev. C **97**, 054615 (2018).

[197] X. Campi, J. Phys. A **19**, L917 (1986).

[198] S. Mallik, G. Chaudhuri, P. Das, and S. D. Gupta, Phys. Rev. C **95**, 061601(R) (2017).

[199] M. D' Agostino *et al.,* Phys. Rev. Lett. **75**, 4373 (1995).

[200] M. Jandel *et al.*, Phys. Rev. C **74**, 054608 (2006).

[201] M. L Gilkes *et al.*, Phys. Rev. Lett. **73**, 1590 (1994).

[202] N. T. Porile *et al.*, Phys. Rev. C **39**, 1914 (1989).

[203] D. H. E. Gross *et al.*, Ann. Phys. **1**, 467 (1992).

[204] Y. Zhang, Z. Li, C. Zhou and M. B. Tsang, Phys. Rev. C **85**, 051602(R) (2012).

[205] R. Kumar *et al.,* Eur. Phys. J. A **52**, 112 (2016).

[206] N. J. Davidson *et al.,* Phys. Lett. B **315**, 12 (1993); *ibid.* Nucl. Phys. A **570**, 61 (1994).

[207] M. Pi, X. Viñas and M. Barranco, Phys. Rev. C **26**, 733 (1982).

[208] G. Sauer, H. Chandra and U. Mosel, Nucl. Phys. A **264**, 221 (1976).

[209] A. S. Jensen and J. Damgaard, Nucl. Phys. A **203**, 578 (1973).

[210] P. Quentin and H. Flocard, Ann. Nucl. Sci. **28**, 523 (1978).

[211] R. Wada *et al.*, Phys. Rev. C **99**, 024616 (2019).

[212] A. Sharma, A. Bharti, S. Gautam and R. K. Puri, Nucl. Phys. A **945**, 95 (2016).

[213] A. Sharma and A. Bharti, Eur. Phys. J. A **52**, 42 (2016).

[214] Y. G. Ma, Phys. Rev. Lett. **83**, 3617 (1999).

[215] R. Kumar, S. Sood, A. Sharma and R. K. Puri, Act. Phys. Pol. B **49**, 301 (2018).

[216] H. Feldmeier and J. Schnack, Rev. Mod. Phys. **72**, 655 (2004).

[217] R. Donangelo, H. Schulz, K. Sneppen, and S. R. Souza, Phys. Rev. C **50**, R563 (1994).

[218] S. R. Souza, M. B. Tsang, R. Donangelo, W. G. Lynch, and A. W. Steiner, Phys. Rev. C **78**, 014605 (2008).

[219] C. Karthikraj, N. S. Rajeswari and M. Balasubramaniam, Phys. Rev. C **86**, 014613 (2012).

[220] M. A. Preston and R. K. Bhaduri, *Structure of the Nucleus (Addison-Wesley, Reading, MA, 1975).*

[221] S. R. Souza *et al.,* Phys. Rev. C **67**, 051602(R) (2003).

[222] P. Danielewicz, Nucl. Phys. A **727**, 233 (2003).

[223] S. Sood, R. Kumar, A. Sharma and R. K. Puri, Phys. Rev. C **99**, 054612 (2019).

[224] C. Dorso and J. Randrup, Phys. Lett. B **301**, 328 (1993).

[225] A. Le Fèvre *et al.*, J. Phys.: Conf. Ser. **668**, 012021 (2016).

[226] A. Le Fèvre *et al.*, Phys. Rev. C **100**, 034904 (2019).

[227] N. Metropolis *et al.*, J. Chem. Phys. **21**, 1087 (1953).

[228] P. J. M. Laarhoven and E. H. L. Aarts, *Simulated Annealing: Theory and Applications (Reidel, Dordrecht, 1987).*

[229] C. Ngo *et al.,* Nucl. Phys. A **499**, 148 (1989).

[230] G. D. Westfall et al., Nucl. Instrum. Methods A **238**, 347 (1985).

[231] R. Kumar and R. K. Puri, Phys. Rev. C **97**, 034624 (2018).

[232] Y. K. Vermani and R. K. Puri, J. Phys. G: Nucl. Part. Phys. **36**, 105103 (2009); S. Kaur and R. K. Puri, Phys. Rev. C **87**, 014620 (2013).

[233] Y. K. Vermani and R. K. Puri, Cent. Eur. J. Phys. **9**, 621 (2011).

[234] V. Singh *et al.,* Phys. Lett. B **765**, 99 (2017).

[235] V. Tripathi *et al.*, Phys. Rev. C **65**, 014614 (2001).

[236] B. A. Bian, F. S. Zhang and H. Y. Zhou, Phys. Lett. B **665**, 314 (2008).

[237] K. Kwiatkowski *et al.,* Phys. Lett. B **423**, 21 (1998); S. P. Avdeyev *et al.,* Eur. Phys. J. A **3**, 75 (1998).

[238] S. S. Adler *et al.,* Phys. Rev. Lett. **96**, 0102304 (2006); S. S. Adler *et al.,* Phys. Rev. Lett. **107**, 142301 (2011).

[239] R. R. Betts, in Proceedings for conference Resonances in Heavy Ion Reactions, edited by K. A. Eberhardt, Lecture Notes in Physics Vol. **156**, p. 185 (Springer, Berlin, 1981).

[240] V. Kaur and S. Kumar, Phys. Rev. C **81**, 064610 (2010).

[241] V. Kaur, S. Kumar and R. K. Puri, Nucl. Phys. A **861**, 37 (2011).

[242] V. Kaur, S. Kumar and R. K. Puri, Phys. Lett. B **697**, 512 (2011).

[243] S. Goyal and R. K. Puri, Nucl. Phys. A **853**, 164 (2011).

[244] S. Goyal, Nucl. Phys. A **856**, 154 (2011).

[245] S. Sharma, R. Kumar and R. K. Puri, private communication.

[246] C.-C. Guo *et al.,* Phys. Rev. C **99**, 044607 (2019).

[247] Ch. O. Bacri *et al.,* Phys. Lett. B **353**, 27 (1995).

[248] S. Nagamiya *et al.,* Phys. Rev. C **24**, 971 (1981).

[249] P. Danielwicz and G. F. Bertsch, Nucl. Phys. A **553**, 712 (1991).

[250] J. Singh and R. K. Puri and J. Aichelin, Phys. Rev. C **62**, 054602 (2000).

[251] S. C. Jeong *et al.*, Phys. Rev. Lett. **72**, 3468 (1994); P. -B. Gossiaux, D. Keane, S. Wang and J. Aichelin, Phys. Rev. C

[252] J. Singh, R. K. Puri and J. Aichelin, Phys. Lett. B **519**, 46 (2001).

[253] J. Kapusta, Phys. Rev. C **29**, 1735 (1984).

[254] Y. K. Vermani and R. K. Puri, Eur. Phys. Lett. **85**, 62001 (2009); C. Dorso and J. Randrup, Phys. Lett. B **301**, 328 (1993); Y. K. Vermani *et al.*, J. Phys. G: Nucl. Part. Phys. **37**, 015105 (2010). **51**, 3357 (1995).

Chapter 6

Summary of the thesis and outlook

In this thesis, the phenomenon of multifragmentation and various features associated with it was presented. Both Quantum Molecular Dynamics (QMD) model and its isospin variant was used to generate the phase space of nucleons from the beginning to the end of the reaction. Further, the phase space of nucleons is clusterized using various clusterization algorithms.

In **chapter1**, we introduced the phase transitions in nuclear matter. We also correlated phenomenon of multifragmentation (emission of multi-particles) with various stages of phase transitions in nuclear matter. Then, we presented details of available experimental facilities and theoretical modelling done to study multifragmentation.

In chapter 2, we discussed the methodology of Quantum Molecular Dynamics (QMD) model and Isospin-dependent Quantum Molecular Dynamics (IQMD) model in detail which is used in the present study.

In **chapter 3**, we discussed various spatial based clusterization algorithms such as MST method and its variants. We extracted the critical exponent τ/λ to study the point of onset of multifragmentation or critical energy point. We also calculated various observables such as S_2, γ_2 and Z_{max2} to study the first-order phase transition in nuclear matter. Our results validated the utility of MST method and its any extension to identify fragments as results were found insensitive to the choice of algorithm.

In **chapter 4**, we put forward the idea of using energy based clusterization algorithm

to overcome the shortcomings of MST method (or any of its variant). We discussed the need and importance of energy based clusterization algorithm i.e., SACA. Then we confronted our calculations with the available experimental results that includes the critical parameter τ (λ) and various other observables such as S_2, γ_2 and Z_{max2}. Our detailed study spans over both light and heavy systems. Our detailed study revealed the capability of SACA method to very well reproduce exactly the energy of minima in power law exponent as shown in experimental data.

In **chapter 5**, we try to associate emission of light particles to study onset of vaporization in nuclear matter. We presented calculations using various clusterization algorithms and its role on the onset of vaporization. Further, we discussed the significance of emission of light particles at various stages of the reaction and associate it to study entropy production. This study was done using IQMD model. Our study spans over the entire range of mass asymmetric reactions and also different total system masses. The entropy was found independent of mass asymmetry and total system mass. The results of both IQMD and QMD model were also compared. The entropy was found independent of both models also.

Summarizing, we have attempted to study phase transitions that nuclear matter undergo at various stages of the reaction with incident energy. We have done this study using complete range of available clusterization algorithms. We have shown that these algorithms provide realistic structure of fragments. Our results showed that, although the MST provide strong evidence to study liquid-gas phase transition in nuclear matter at the later stages of the reaction, the SACA can give these indications more accurately and precisely at the early stages of the reaction. In future scope, it will be very interesting to introduce new parameters to study phase transitions in nuclear matter. We have also shown the systematics of light particles near/after the complete vaporization of system.

6.1 Outlook

We have investigated the role of various clusterization algorithms on the phase-transitions in nuclear matter and related phenomenon, still there are numerous challenges yet to be solved. The most important challenge is to study role of varying various model ingredients, mass asymmetry and N/Z ratios on phase transition. Despite the fact that various observables have been put forward as probe in the literature which give information about

dynamics involved with phase-transitions in nuclear matter but, we need to search for new observables to better understand the physics related to phase-transitions in nuclear matter. In chapters 3 and 4, we studied the role of various clusterization algorithms on liquid-gas phase transition. This study can be extended by studying the complete range of asymmetric reactions and by defining new observables to define the existence of liquid-gas phase transition. In chapter 5, we have associated the emission of light particles to the entropy production and onset of vaporization. It would be quite interesting to extend it to study role for asymmetric reactions and N/Z ratio on these phenomena.